

# Simulating the role of biogeochemical hotspots in driving nitrogen export from dryland watersheds

Jianning Ren<sup>1</sup>, Erin Hanan<sup>1</sup>, Aral C Greene<sup>2</sup>, Christina Tague<sup>3</sup>, Alexander Krichels<sup>4</sup>, William Burk<sup>1</sup>, Joshua Schimel<sup>3</sup>, and Peter M Homyak<sup>2</sup>

<sup>1</sup>University of Nevada, Reno

<sup>2</sup>University of California, Riverside

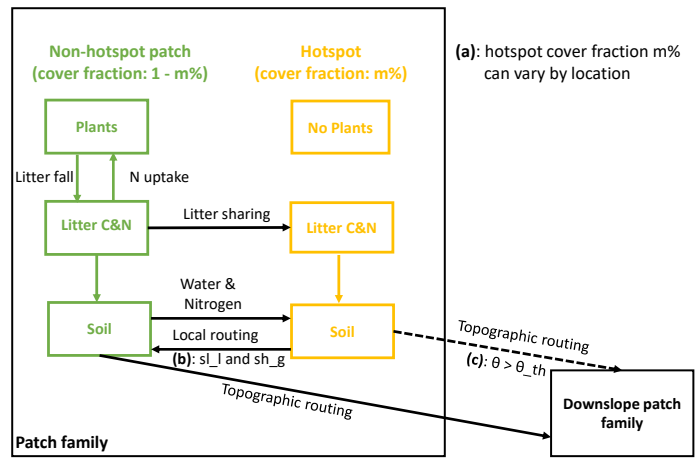
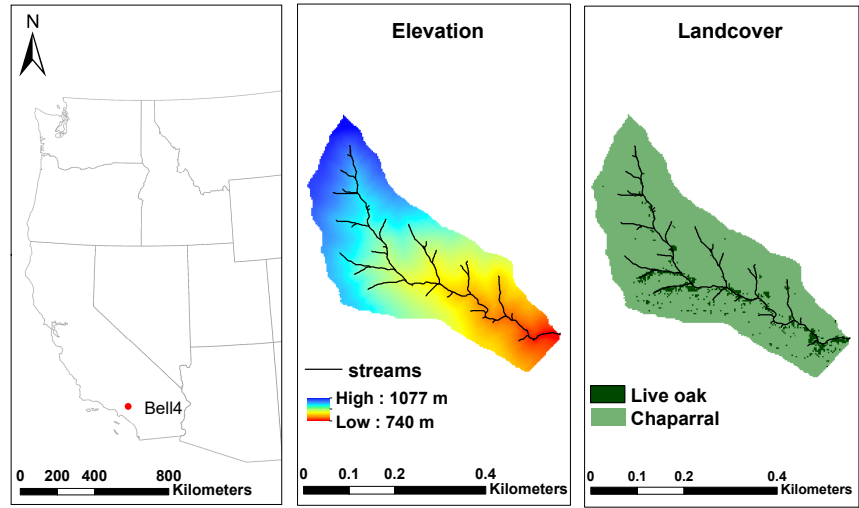
<sup>3</sup>University of California, Santa Barbara

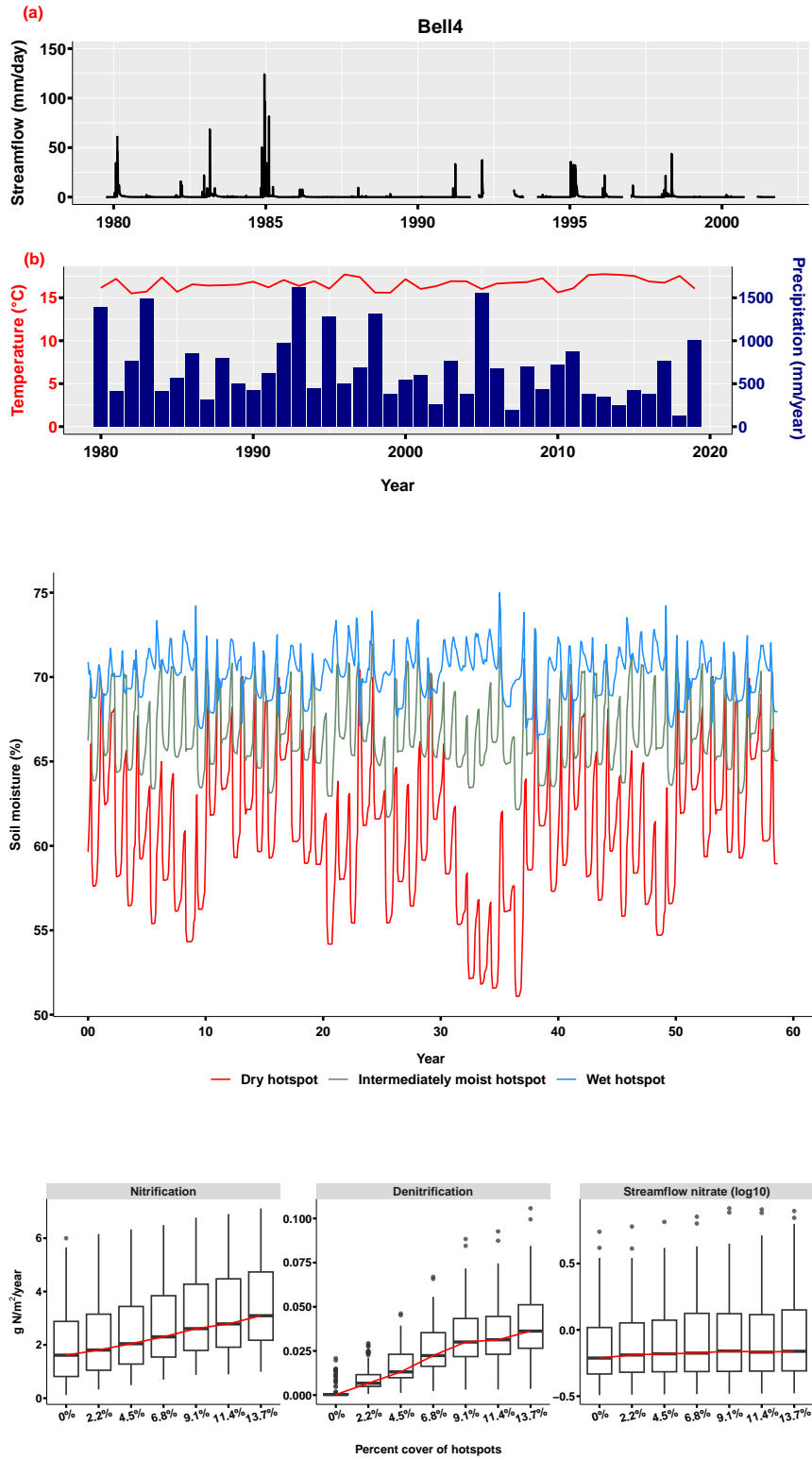
<sup>4</sup>USDA Forest Service Rocky Mountain Research Station

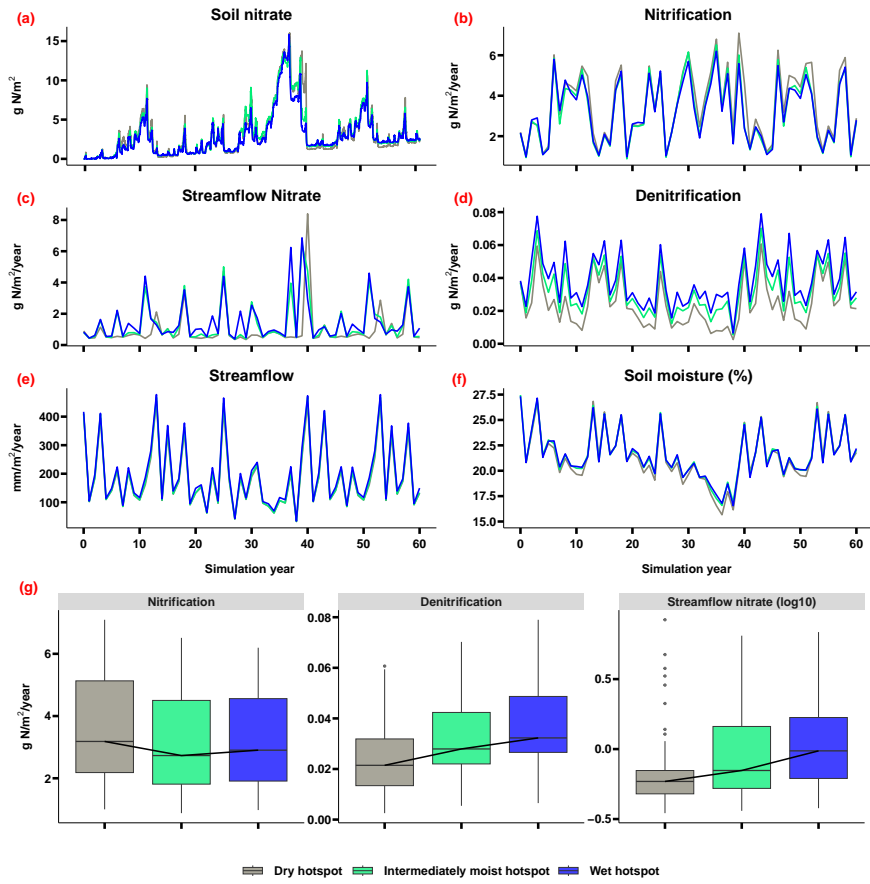
August 8, 2023

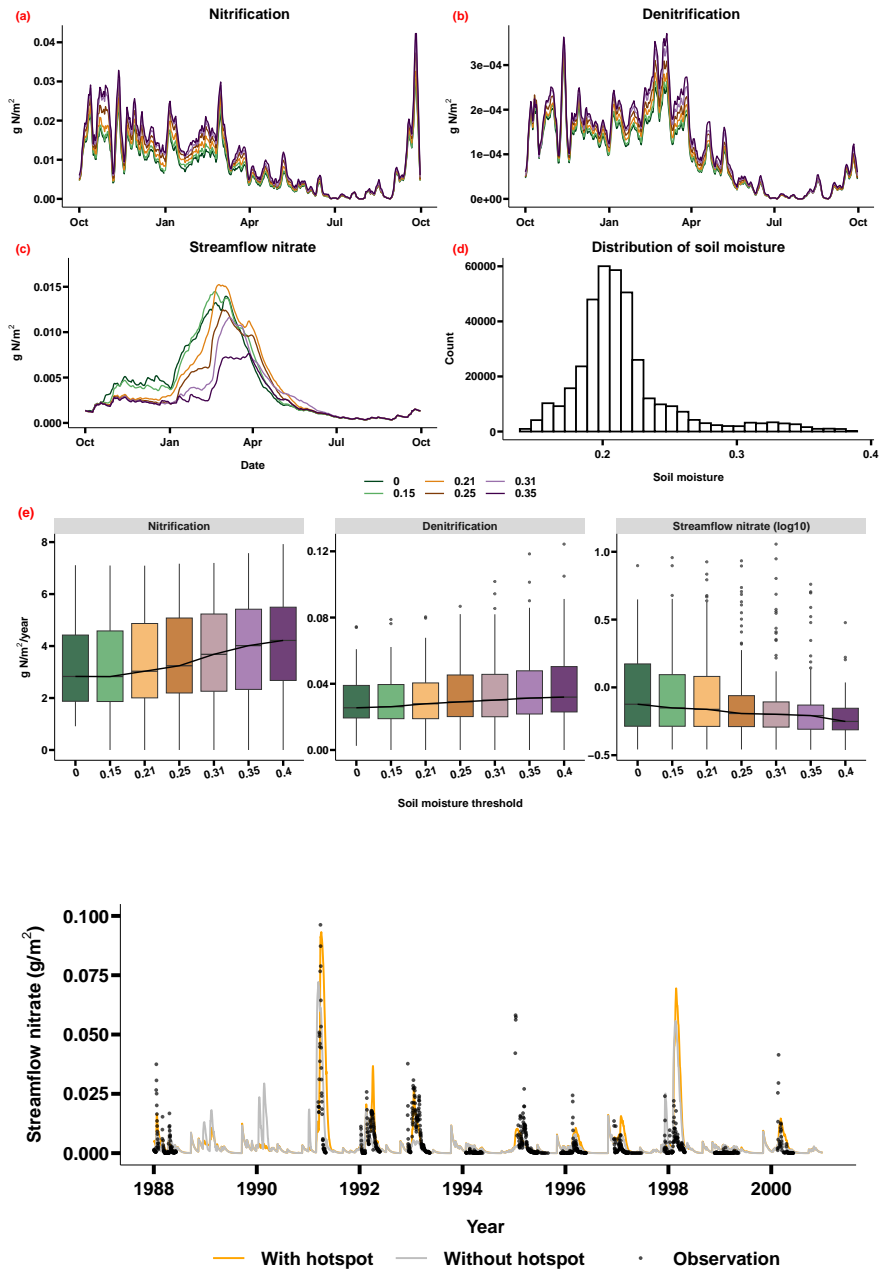
## Abstract

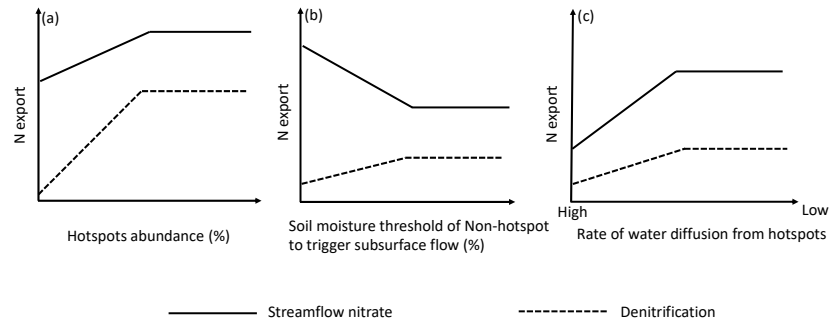
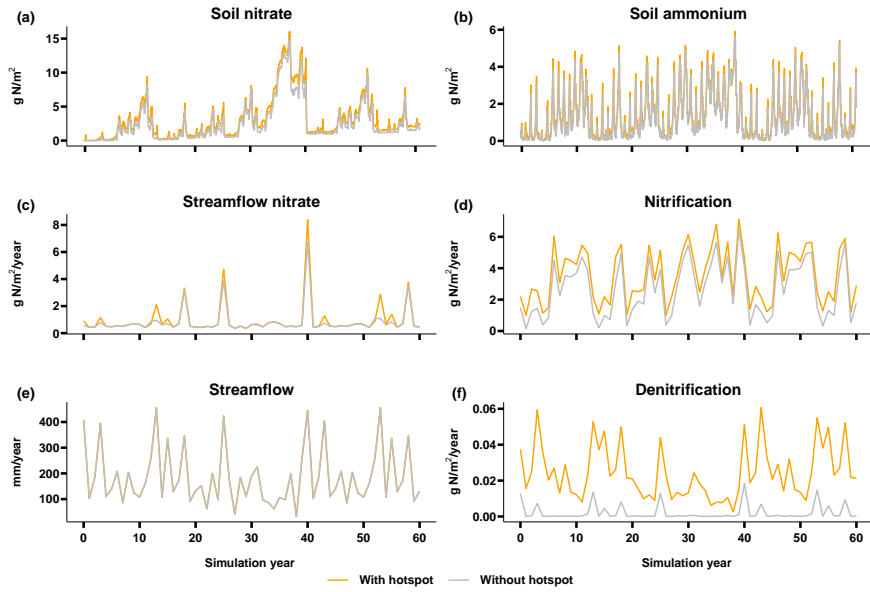
Climate change and nitrogen (N) pollution are altering biogeochemical and ecohydrological processes in dryland watersheds, increasing N export, and threatening water quality. While simulation models are useful for projecting how N export will change in the future, most models ignore biogeochemical “hotspots” that develop in drylands as moist microsites become hydrologically disconnected from plant roots when soils dry out. These hotspots enable N to accumulate over dry periods and rapidly flush to streams when soils wet up. To better project future N export, we developed a framework for representing hotspots using the ecohydrological model RHESSys. We then conducted a series of virtual experiments to understand how uncertainties in model structure and parameters influence N export. Modeled export was sensitive to the abundance of hotspots in a watershed, increasing linearly and then reaching an asymptote with increasing hotspot abundance. Peak streamflow N was also sensitive to a soil moisture threshold at which subsurface flow from hotspots reestablished, allowing N to be transferred to streams; it increased and then decreased with an increasing threshold value. Finally, N export was generally higher when water diffused out of hotspots slowly. In a case study, we found that when hotspots were modeled explicitly, peak streamflow nitrate export increased by 29%, enabling us to better capture the timing and magnitude of N losses observed in the field. This modeling framework can improve projections of N export in watersheds where hotspots play an increasingly important role in water quality.











1 **Simulating the role of biogeochemical hotspots in driving nitrogen export**  
2 **from dryland watersheds**

3 <sup>1</sup>Jianning Ren, <sup>1</sup>Erin J. Hanan, <sup>2</sup>Aral Greene, <sup>3</sup>Christina Tague, <sup>4</sup>Alexander H. Krichels, <sup>1</sup>William  
4 D. Burke, <sup>5</sup>Joshua P. Schimel, <sup>2</sup>Peter M. Homyak

5 <sup>1</sup>Department of Natural Resources and Environmental Science, University of Nevada, Reno,  
6 89501, Reno, USA

7 <sup>2</sup>Department of Environmental Sciences, University of California, Riverside, 92521, Riverside,  
8 USA

9 <sup>3</sup>Bren School of Environmental Science & Management, University of California, Santa Barbara,  
10 93106, Santa Barbara, USA

11 <sup>4</sup>USDA Forest Service Rocky Mountain Research Station, 87102, Albuquerque, USA

12 <sup>5</sup>Department of Ecology, Evolution and Marine Biology, University of California, Santa Barbara,  
13 93106, Santa Barbara, USA

14 Correspondence:

15 Jianning Ren ([nren@unr.edu](mailto:nren@unr.edu), [renjianning@gmail.com](mailto:renjianning@gmail.com))

16 Erin Hanan ([ehanan@unr.edu](mailto:ehanan@unr.edu))

17 Key Points:

- 18 • We developed a model framework to represent biogeochemical hotspots in dryland  
19 ecosystems.
- 20 • Nitrogen export is sensitive to parameters controlling hotspot abundance, subsurface  
21 hydrologic connectivity, and soil moisture dynamics.
- 22 • The abundance and physical characteristics of hotspots can affect the timing of hot  
23 moments.

24 **Abstract**

25           Climate change and nitrogen (N) pollution are altering biogeochemical and  
26 ecohydrological processes in dryland watersheds, increasing N export, and threatening water  
27 quality. While simulation models are useful for projecting how N export will change in the  
28 future, most models ignore biogeochemical “hotspots” that develop in drylands as moist  
29 microsites become hydrologically disconnected from plant roots when soils dry out. These  
30 hotspots enable N to accumulate over dry periods and rapidly flush to streams when soils wet up.  
31 To better project future N export, we developed a framework for representing hotspots using the  
32 ecohydrological model RHESSys. We then conducted a series of virtual experiments to  
33 understand how uncertainties in model structure and parameters influence N export. Modeled  
34 export was sensitive to the abundance of hotspots in a watershed, increasing linearly and then  
35 reaching an asymptote with increasing hotspot abundance. Peak streamflow N was also sensitive  
36 to a soil moisture threshold at which subsurface flow from hotspots reestablished, allowing N to  
37 be transferred to streams; it increased and then decreased with an increasing threshold value.  
38 Finally, N export was generally higher when water diffused out of hotspots slowly. In a case  
39 study, we found that when hotspots were modeled explicitly, peak streamflow nitrate export  
40 increased by 29%, enabling us to better capture the timing and magnitude of N losses observed  
41 in the field. N export further increased in response to interannual variability in precipitation,  
42 particularly when multiple dry years were followed by a wet year. This modeling framework can  
43 improve projections of N export in watersheds where hotspots play an increasingly important  
44 role in water quality.

## 45 **1 Introduction**

46 Climate change and atmospheric nitrogen (N) deposition are accelerating biogeochemical  
47 cycling in dryland ecosystems and increasing N loading in streams, which can pose a major  
48 threat to water quality (Borer & Stevens, 2022; Fenn et al., 2003). However, the extent to which  
49 deposited N is exported to streams remains difficult to predict, in part because models are limited  
50 in their ability to capture hotspots—defined as wetter microsites in the soil that have  
51 disproportionately high rates of biogeochemical cycling—which can strongly influence N fluxes  
52 in dryland soils (Vargas et al., 2013). For example, hotspots enable N to accumulate over dry  
53 periods and rapidly flush to streams when soils wet up (McClain et al., 2003; Parker & Schimel,  
54 2011). This can occur even when plants are N-limited because precipitation pulses can mobilize  
55 accumulated N more quickly than plants are able to take it up (Homyak et al., 2014). As the  
56 global distribution of drylands expands with climate warming (Seager et al., 2018), and as  
57 urbanization increases rates of N deposition (Borer & Stevens, 2022), it is critical to better  
58 account for the mechanisms driving N export in models (Gustine et al., 2022; Schimel, 2018).

59 Hotspots can range in size from microsites within soil aggregates (Ebrahimi & Or, 2018)  
60 to islands of fertility within landscape patches (Osborne et al., 2020). While landscape models  
61 may effectively represent the later by parameterizing plant physiological processes that promote  
62 resource heterogeneity—for example, transpiration-driven nutrient accumulation beneath woody  
63 plant canopies in savannas; (Ridolfi et al., 2008)—representing the role of microscale  
64 biogeochemical hotspots is much more challenging at watershed scales. For one, soil moisture  
65 and subsurface transport processes are often oversimplified and not fully integrated into  
66 landscape-scale N-cycling models (Ouyang et al., 2017; Poblador et al., 2017; Schmidt et al.,  
67 2007; Zhang et al., 2018). When models do incorporate coupled hydrological-biogeochemical

68 processes, they often reduce spatial heterogeneity by averaging soil hydraulic parameters across  
69 a basin (Crow et al., 2012; Lin et al., 2015; Tague, 2009; Zhu et al., 2012, 2015). As a result,  
70 these models do not capture the role of soil microsites that remain wetter than bulk soils for at  
71 least some time into the dry season. While more detailed representation of soil heterogeneity is  
72 needed, at least three key uncertainties remain in scaling microsite processes across an entire  
73 watershed: (1) how hotspots are distributed across watersheds (McClain et al., 2003) (2) the  
74 amount of precipitation required to reestablish for hydrological connection between hotspots and  
75 bulk soils and to generate subsurface flow (Zhu et al., 2018), and (3) how the physical  
76 parameters governing fine-scale water diffusion from hotspots are distributed across a watershed  
77 (Clark et al., 2017).

78 A common modeling approach to represent the effects of fine-scale spatial heterogeneity  
79 on large-scale hydrologic fluxes is to incorporate distributions of sub-grid state variables that  
80 influence large-scale fluxes (i.e., statistical-dynamical flux parameterizations occurring within a  
81 grid cell; the smallest spatially explicit model unit; Clark et al., 2017; Wood et al., 1992). For  
82 example, Burke et al. (2021) developed an approach using the ecohydrological model RHESSys,  
83 which uses a distribution of aspatial, sub-grid vegetation patches that interact to influence grid-  
84 scale ecohydrological processes. This approach can better capture spatial heterogeneity without  
85 requiring detailed spatial information at sub-grid scales or increasing computational costs. To  
86 better predict how climate change modifies N retention and export, we developed a framework  
87 for modeling belowground hotspots and their interactions with soil moisture and subsurface flow  
88 by expanding the Burke et al. (2021) aspatial approach.

89

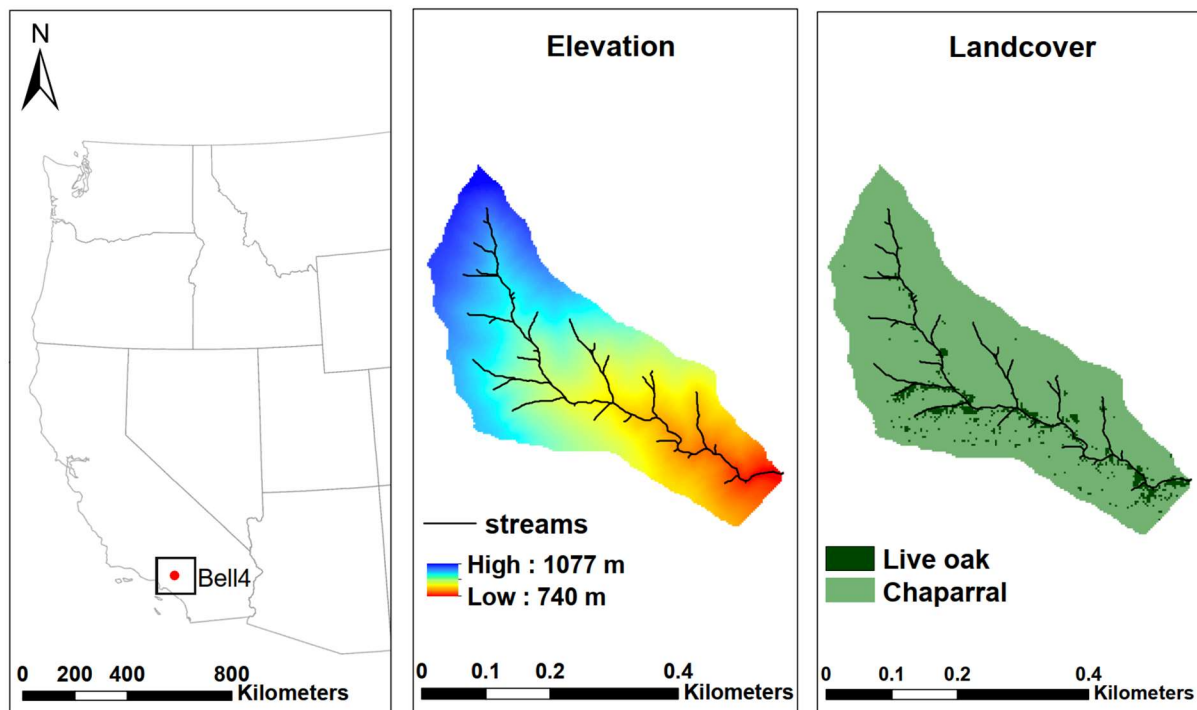
90 Our new modeling framework enables N to accumulate in microscale hotspots—  
91 represented aspatially within 10-m resolution grid cells—which contain sufficient moisture for  
92 decomposition to occur but are hydrologically disconnected from roots when the soils dry out.  
93 These micro-scale hotspot patches slowly lose water through diffusion and evaporation over the  
94 course of the dry season and can become hydrologically reconnected to the surrounding  
95 vegetated patches when soils wet up. Using this framework, we conducted a set of virtual  
96 experiments in a dryland, chaparral watershed in Southern California to characterize model  
97 sensitivity to three key sources of uncertainty: (1) the area percentage of hotspots within the  
98 watershed, (2) the length of time it takes for water to diffuse from hotspots during periods of  
99 drought, and (3) the moisture conditions under which hydrological connectivity between hotspot  
100 and non-hotspot locations reestablishes. Finally, we used field observations of N export to  
101 optimize the parameters controlling N dynamics and then with an optimized model, we  
102 investigated how precipitation patterns can influence hotspot effects on N export. This case study  
103 demonstrates how our modeling framework can be used to improve our theoretical understanding  
104 of the role biogeochemical hotspots play in N cycling and retention in drylands.

## 105 **2 Methods**

### 106 **2.1 Study area**

107 Model simulations were conducted in the Bell 4 basin (0.14 km<sup>2</sup>), which is part of the  
108 San Dimas experimental forest located northeast of Los Angeles, California (34°12'N, 117°47'E;  
109 Figure 1). Elevations in Bell 4 range from 700 to 1024 meters. The topography is characterized  
110 by steep slopes with steep channel gradients. Soils are shallow, coarse-textured sandy loams,  
111 which are weathered from granite (Chaney et al., 2016; Dunn et al., 1988) and classified as Typic  
112 Xerorthents (Soil Survey Staff, 2022) The region has hot, dry summers (June to September

113 around 17 mm precipitation) and cool, moist winters (698 mm precipitation); mean annual  
114 precipitation is around 715 mm and daily temperatures range from -8 °C to 40 °C. Vegetation  
115 cover is mainly mixed chaparral with chamise (*Adenostoma fasciculatum*), ceanothus  
116 (*Ceanothus spp.*), and black sage (*Salvia mellifera*) on south-facing slopes; ceanothus and  
117 California laurel (*Umbellularia californica*) on north-facing slopes; and some live oak (*Quercus*  
118 *agrifolia*) along riparian areas (Wohlgemuth, 2006).



120 *Figure 1. Bell 4 watershed in the San Dims experimental forest located in Southern California,*  
121 *U.S. (34°12'N, 117°47'E). The watershed is 0.14 km<sup>2</sup>.*

## 122 **2.2 RHESSys model**

123 The regional hydro-ecologic simulation system (RHESSys) is a spatially distributed,  
124 process-based model that simulates interacting ecohydrological and biogeochemical processes at  
125 multiple scales (Chen et al., 2020; Hanan et al., 2017; Tague, 2009; Tague & Band, 2004). The  
126 smallest spatial unit is the “patch,” which has a 10-meter resolution in the current study. At the

127 patch scale, vertical hydrologic fluxes include canopy interception, transpiration, evaporation,  
128 infiltration, capillary rise, and drainage from the rooting zone to the saturated zone. Carbon (C)  
129 cycling processes are tightly coupled with hydrology and soil moisture and include  
130 photosynthesis, allocation of net photosynthate, plant and soil respiration, and litter and soil  
131 decomposition. Nitrogen cycling includes atmospheric N deposition, mineralization, nitrification,  
132 immobilization, denitrification, plant uptake, and export to streams (Hanan et al., 2017; Lin et  
133 al., 2015). RHESSys has been parameterized and validated in several watersheds across the  
134 western USA, including in several chaparral watersheds (Burke et al., 2021; Chen et al., 2020;  
135 Hanan et al., 2017, 2021; Lin et al., 2015; Meentemeyer & Moody, 2002; Ren et al., 2021, 2022;  
136 Tague, 2009).

137         There are four layers for vertical soil moisture processes, including a surface detention  
138 store, a root zone store, an unsaturated store below the root zone, and a saturated store. The  
139 vertical hydrologic processes also include canopy layers, snowpack, and litter moisture stores.  
140 Rain throughfall from multiple canopy layers and a litter layer provide potential infiltration. If  
141 the precipitation falls as snow, snow throughfall updates a snowpack store. Then the surface  
142 detention storage receives water from canopy throughfall and snowmelt at a daily time step.  
143 Following precipitation and throughfall, water infiltrates into the soil following the Phillip  
144 (1957) infiltration equation. At a daily timestep, ponded water that has not infiltrated is added to  
145 detention storage and any water that is above detention storage capacity generates overland flow.

146         Infiltration updates one of three possible stores: a saturated store when the water table  
147 reaches the surface, a rooting zone store, or an unsaturated store for unvegetated patches. A  
148 portion of infiltrated water can bypass the rooting zone and unsaturated store through  
149 macropores. This bypass flow (carrying N) is added to a deeper groundwater store at the

150 subbasin scale. Water drains vertically from the unsaturated store or root zone store based on  
 151 hydraulic conductivity. Capillary rise moves water from the saturated zone to the root zone or  
 152 unsaturated store based on Eagleson (1978). Lateral fluxes can occur through both shallow  
 153 subsurface flow between patches and through bypass flow that contributes to a deeper hillslope-  
 154 scale groundwater flow model. Shallow subsurface saturated flow between patches follows  
 155 topography and changes with saturation deficit and transmissivity.

156 RHESSys simulates subsurface lateral redistribution of water and N between patches  
 157 based on topographic gradients and soil hydraulic parameters (Tague, 2009). Nitrification rates  
 158 in RHESSys are calculated based on the CENTURY<sub>NGAS</sub> model, where the nitrification rate is a  
 159 function of soil pH ( $f_{pH}$ ; Hanan et al 2017), moisture ( $f_{H_2O}$ ), soil temperature ( $f_T$ ), and available  
 160 soil ammonium ( $f_{NH_4}$ ; Parton, 1996):

$$161 \quad N_{nitrif} = soil.NH4 \times f_{pH} \times f_{H_2O} \times f_T \times f_{NH_4} \quad \text{Eq (1)}$$

162 The pH scalar ( $f_{pH}$ ) is calculated as:

$$163 \quad f_{pH} = \frac{0.56 + \arctan(\pi \times 0.45 \times (-5 + pH))}{\pi} \quad \text{Eq (2)}$$

164 The soil moisture scalar ( $f_{H_2O}$ ) is calculated as:

$$165 \quad f_{H_2O} = \left(\frac{\theta - b}{a - b}\right)^d \left(\frac{b - a}{a - c}\right)^{\left(\frac{\theta - c}{a - c}\right)} d \quad \text{Eq (3)}$$

166 Where  $a$ ,  $b$ ,  $c$ , and  $d$  are parameters related to soil texture based on Parton et al. (1996) and  $\theta$  is  
 167 volumetric soil moisture.

168 The temperature scalar ( $f_T$ ) is calculated as:

$$169 \quad f_T = 0.06 + 0.13 \exp^{0.07T_{soil}} \quad \text{Eq (4)}$$

170 Where  $T_{soil}$  is the surface soil temperature in degrees C.

171 The ammonium concentration available for nitrification is calculated as:

$$172 \quad f_{NH_4} = 1.0 - \exp^{-0.0105 * NH_{4concl}} \quad \text{Eq (5)}$$

173 Where  $NH_{4con}$  is the soil ammonium concentration in the fast-cycling soil layer.

174 N export includes denitrification and subsurface lateral flow of ammonium, nitrate, and  
175 dissolved organic N (DON). Denitrification is calculated based on a maximum denitrification  
176 rate ( $R_{NO_3}$ ), and is modified by soil moisture ( $f_{H_2O}$ ), and soil respiration ( $f_{hrCO_2}$ ):

$$177 \quad N_{denitrif} = R_{NO_3} \times f_{H_2O} \times f_{hrCO_2} \quad \text{Eq (6)}$$

178 The maximum denitrification rate is calculated as:

$$179 \quad R_{NO_3} = 0.0011 + \frac{a \tan(\pi \times 0.002 \times (\frac{NO_{3\_soil}}{N_{soil} + C_{soil}} - 180))}{\pi} \quad \text{Eq (7)}$$

180 Where  $NO_{3\_soil}$  is the available nitrate (kg N/m<sup>2</sup>) in soil and  $N_{soil}$  and  $C_{soil}$  are soil N (kg N/m<sup>2</sup>)  
181 and C (kg C/m<sup>2</sup>) amounts, respectively.

182 The soil moisture limitation is calculated as:

$$183 \quad f_{H_2O} = \frac{a}{b(\frac{c}{b^{d \times \theta}})} \quad \text{Eq (7)}$$

184  $\theta$ ,  $a$ ,  $b$ ,  $c$ , and  $d$  are defined in eq. 3 above.

185 The effect of soil respiration is calculated as:

$$186 \quad f_{hrCO_2} = \frac{0.0024}{1 + \frac{200}{e^{(3.5 \times hr)}}} - 0.00001 \quad \text{Eq (8)}$$

187 Where  $hr$  is total daily respiration (g C/m<sup>2</sup>/day).

188 Nitrate enters the soil from infiltration or from the surface detention store. Nitrate in the  
189 soil is transported by subsurface flow in the saturated zone, while in the unsaturated soil, there is  
190 no lateral nitrate transport (Chen et al., 2020; Tague & Band, 2004). Vertical distribution of  
191 nitrate in the unsaturated zone soil profile is assumed to follow an exponential decay function,  
192 where the surface layer has more nitrate and deeper soil has less. the available nitrate at soil  
193 depth  $z$  is calculated as

$$194 \quad NO_{3\_soil}(z) = NO_{3\_surface} \times \exp^{-N_{decay} \times z} \quad \text{Eq (10)}$$

195 Where  $NO_{3\_surface}$  is nitrate at soil surface and  $N_{decay}$  is a soil specific parameter that defines the  
196 rate of nitrate decay. When water is moving between the unsaturated zone and the saturated  
197 zone, through downward leaching or upward capillary rise, nitrate moves with water based on its  
198 concentration.

199 Nitrate export follows the flushing hypothesis (Chen et al., 2020). As the water table rises, more  
200 N becomes available for flushing. The total soil nitrate export ( $NO_{3\_out}$ ) is calculated as the  
201 integration of soil nitrate below the water table:

$$202 \quad NO_{3\_out} = \int_{z_{max}}^{z_s} \frac{q_z}{S_z} NO_{3\_soil} NO_{3\_mobile} \quad \text{Eq (11)}$$

203 Where  $z_{max}$  is the maximum water table depth,  $z_s$  is current water table depth,  $q_z$  is the net lateral  
204 transport of water from the patch at depth  $Z$ ;  $S_z$  is the soil water content (in meters) and  $NO_{3\_mobile}$   
205 is a parameter that defines the portion of nitrate that is mobile (related to soil type). Mobile  
206 surface N can also be transported to deep ground water through preferential flow paths.

207 Recent improvements to RHESSys enable users to account for fine-scale (within patch)  
208 heterogeneity (e.g., different types of vegetation cover and associated soil layers that may share

209 water within a single patch; Burke et al. 2021). These are referred to as "aspatial patches." When  
210 running RHESSys using the aspatial patch framework, "patch families" become the smallest  
211 spatially explicit model unit, and aspatial patches (nested within a patch family) are the smallest  
212 aspatial model unit. Note that an aspatial patch within a patch family is used to represent  
213 a distribution of a given vegetation type (e.g., trees or shrubs) based on observed (or  
214 hypothetical) distributions. It can but does not necessarily represent a single stand or clump  
215 of vegetation cover; vegetation from a single aspatial patch within a patch family does not have a  
216 defined distribution in RHESSys, so the assumption is that biophysical interactions, such as the  
217 extent to which a given cover type shares water, are more important than their physical location  
218 within the finest grid cell. Because there are no physical locations of aspatial patches within a  
219 patch family, within patch heterogeneity can be modeled without explicitly parameterizing and  
220 modeling fine scale spatial units that would be both computationally prohibitive and nearly  
221 impossible to parameterize with measured data.

222         Local water routing between aspatial patches inside a patch family is based on root access  
223 to water (Figure 2). Local routing moves water between aspatial patches based on user defined  
224 rules. Most commonly, water is distributed among aspatial patches as a function of relative  
225 differences between their rooting and unsaturated zone water contents and mediated by gaining  
226 and losing coefficients defined for each cover type. In this framework, an aspatial patch will gain  
227 water if its water content is below the patch family mean and vice versa, with the rate of water  
228 transfer controlled by sharing coefficients. Sharing coefficients to capture the integrated effects  
229 of uncertain, fine-scale variation in root distributions, and how root distributions and forest  
230 structure interact with fine-scale soil drainage characteristics. Nitrate and dissolved organic C are

231 exchanged along with water during local routing. A detailed description of aspatial patches can  
232 be found in Burke et al. (2021).

### 233 **2.3 Model development**

234 To enable RHESSys to account for biogeochemical hotspots, we expanded the aspatial  
235 patch framework to incorporate “hotspot” aspatial patches within each patch family. These  
236 aspatial patches represent a distribution of unvegetated microsites where biogeochemical cycling  
237 can be hydrologically disconnected, as soils dry out, from aspatial patches that contain plant  
238 roots (Figure 2). To model hotspot aspatial patches (hereafter called hotspots), we implemented  
239 three key model developments: (1) model algorithms that enable hotspots to access soil and litter  
240 C and N from neighboring non-hotspot patches for decomposition and biogeochemical cycling,  
241 and (2) algorithms and parameters that control the moisture conditions under which hotspots are  
242 hydrologically disconnected from other aspatial patches in the saturated zone, (3) parameters that  
243 control water diffusion in the unsaturated and/or root zone between hotspot and non-hotspot  
244 patches as soils dry out.

245 Research has shown that N-rich microsites can occur in unvegetated locations where  
246 there is less N uptake and less water demand from plants (Zhu et al., 2018). In the original  
247 RHESSys framework, unvegetated patches were used to represent large (e.g., 10 to 30-m) areas  
248 with no vegetation. Without vegetation inputs, these patches did not develop C and N stores to  
249 support microbial biogeochemical cycling. To generate hotspots, we implemented a litter sharing  
250 scheme that moves litter from vegetated aspatial patches to hotspots at an annual timestep to  
251 coincide with litter fall (Figure 2). Because we assume that hotspot aspatial patches occur at fine  
252 scales across a given 10-m patch family, it is reasonable to assume that they have access to plant  
253 litter for decomposition and N cycling from other aspatial patches within the patch family. The

254 amount of litter shared ( $CN_{share}$ ) is a function of the mean litter C and N content of the patch  
 255 family ( $CN_{mean}$ ), where the amount of C and N in a hotspot patch after litter sharing ( $CN_{hotspot}$ )  
 256 cannot be above the patch family mean (Eq 12). To enable N cycling in hotspots, hotspots also  
 257 have access to 1% of the protected soil organic C and N pools from the vegetated patch families.  
 258 The litter C and N routing is described as

$$259 \quad CN_{share} = \frac{(\sum_{i=1}^{n_{veg}} (CN_{veg\_i} - CN_{mean}) \times coef\_litter)}{n_{hotspot}} \quad \text{Eq (12)}$$

$$260 \quad CN_{hotsp\_after} = \min (CN_{hotspot\_before} + CN_{share}, CN_{mean}) \quad \text{Eq (13)}$$

$$261 \quad CN_{veg\_after\_i} = CN_{veg\_i} - (CN_{veg\_i} - CN_{mean}) \times coef\_litter \quad \text{Eq (14)}$$

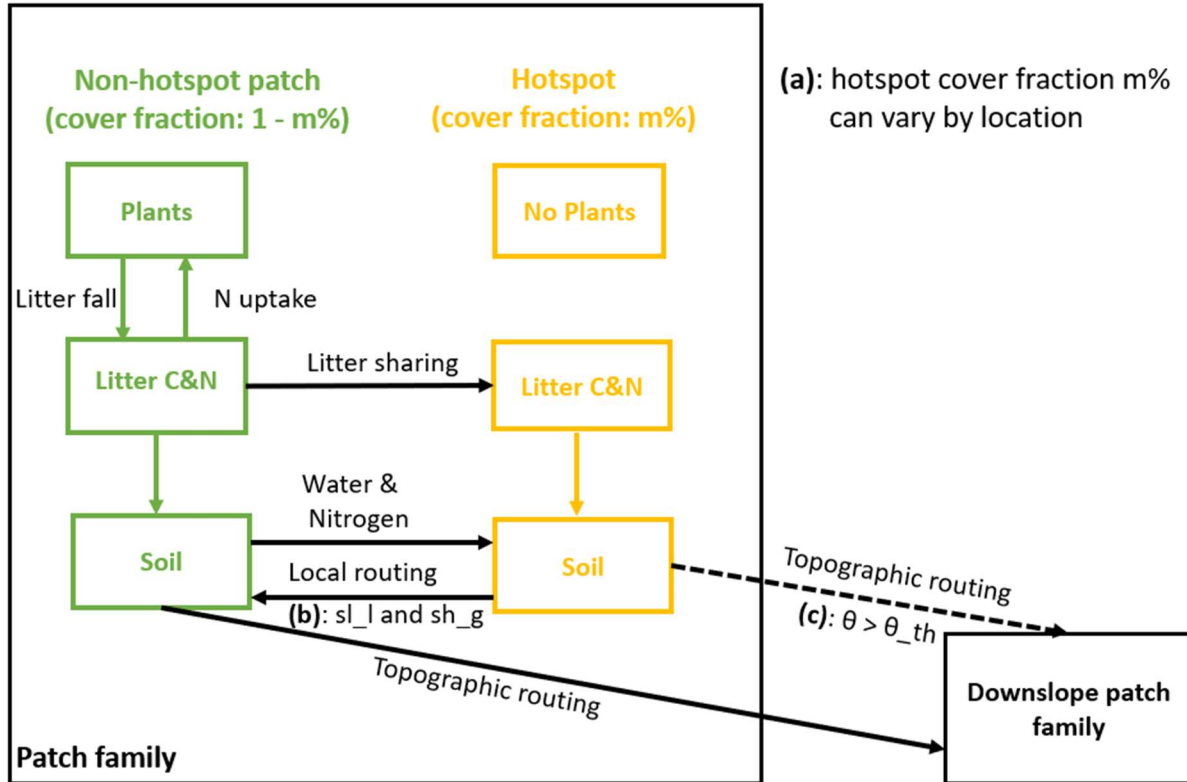
262 Where,  $n_{veg}$  is the number of non-hotspot patches in a patch family,  $CN_{veg}$  is the amount  
 263 of litter C and N in a non-hotspot patch,  $n_{hotspot}$  is the number of hotspot patches in a patch  
 264 family.  $Coef\_litter$  is the sharing coefficient parameter that controls the amount of litter sharing.  
 265 Hotspot patches can also be assigned a finer soil texture (e.g., loam), which can hold more water  
 266 than non-hotspot patches. In the current model, non-hotspot patches were comprised of sandy  
 267 loam (based on the POLARIS database; Chaney et al., 2016).

268 To control subsurface hydrologic flow from hotspots to vegetated patches, we set up a  
 269 soil moisture threshold for non-hotspot patches ( $\theta_{th}$ ), above which, water flows into them from  
 270 the saturated zone in hotspots. In other words, when non-hotspot patches dry down, they become  
 271 hydrologically disconnected from hotspots and they become reconnected when soils wet up  
 272 (Figure 2c & Eq 15).

$$273 \quad \begin{cases} \theta_{veg} > \theta_{th}: \text{subsurface flow move water and nitrate from hotspots to neighboring non - hotspot pathes} \\ \theta_{veg} \leq \theta_{th}: \text{no subsurface flow from hotspots to neighbor normal patches} \end{cases} \quad \text{Eq (15)}$$

274 This threshold is used to define a condition where “water films” can form as soils dry  
275 down, which enables microscale biogeochemical cycling while reducing nitrate leaching from  
276 hotspots over the course of the hot, dry summer (Parker & Schimel, 2011). When soils are  
277 rewetted at the onset of the rainy season, the water table rises, and hydrologic connectivity  
278 reestablishes between hotspot and non-hotspot patches. This can lead to rapid nitrification and  
279 nitrate export before plants become active and gain access to N that accumulated during dry  
280 periods of hydrologic disconnection (Parker & Schimel, 2011). While the thresholds at which  
281 hydrologic connectivity reestablishes are not currently well established, the threshold parameter  
282 can be calibrated to match field observations.

283 Although subsurface flow from hotspot patches remains somewhat disconnected during  
284 the dry season, water can still slowly diffuse from hotspots as soils dry out. To account for this,  
285 we developed water gain coefficients ( $sh\_g$ ) and water loss coefficients ( $sh\_l$ ) that constrain  
286 local routing to and from hotspots and the unsaturated and rooting zone in the surrounding non-  
287 hotspot patches (Figure 2a). During the dry season (June to November), the default  $sh\_g$  was set  
288 to 0.05 and  $sh\_l$  was set to 0.9 to simulate hotspots losing water. During the wet season  
289 (December to May), the default  $sh\_g$  was 0.9 and  $sh\_l$  was 0.05 to simulate hotspots gaining  
290 water. We rely on sharing coefficients here to capture “film” dynamics that depend on micro-  
291 scale characteristics that are not feasible to explicitly model but have been documented to  
292 influence hot-spot dynamics in field and lab-studies (Homyak et al., 2016; Parker & Schimel,  
293 2011). To summarize, while soil moisture gradients control whether routing occurs in the  
294 saturated zone between hotspot and non-hotspot patches, the sharing coefficients control the rate  
295 of local water transfer in the unsaturated zone.



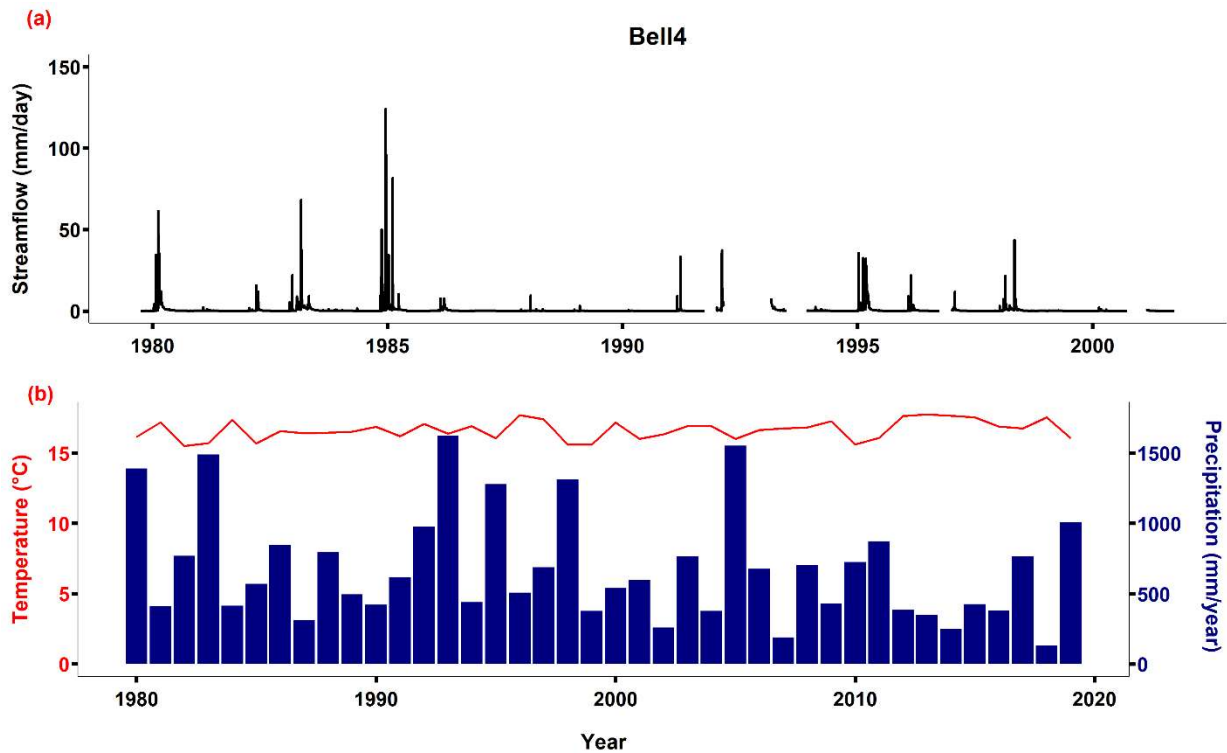
296

297 *Figure 2. Conceptual overview of hotspots patches nested within each patch family. Each year,*  
 298 *vegetated patches share litter C and N with hotspot patches from the portions of their stores that*  
 299 *are greater than the patch family means. Note that the conceptual figure does not indicate that*  
 300 *there is only one hotspot and one non-hotspot patch in a patch family, but rather represents their*  
 301 *cover fraction. Key model uncertainties include: (a) hotspot cover fraction  $m\%$ , which can vary*  
 302 *by location, (b) local routing of water and N in the unsaturated zone between aspatial patches*  
 303 *based on the mean water content of the patch family, which can be mediated by sharing*  
 304 *coefficients  $sh_l$  and  $sh_g$ ; and (c) topographic routing in the saturated zone from patches in one*  
 305 *patch family to patches in downslope patch families, which can be controlled by a soil moisture*  
 306 *threshold  $\theta_{th}$ . The dashed lines signify that hotspots are hydrologically disconnected from non-*  
 307 *hotspot patches during dry periods but reconnect during wet periods when soil moisture in non-*  
 308 *hotspot patch is larger than  $\theta_{th}$ . The extent of hydrological routing between hotspot and non-*  
 309 *hotspot patches is controlled by  $\theta_{th}$ , which can be calibrated to match field observations.*

## 310 2.4 Data

311 To generate metrological inputs for RHESSys scenarios in Bell 4 using the new hotspot  
 312 framework, we compared daily meteorological data from gridMET (Abatzoglou, 2013),  
 313 including maximum and minimum temperatures, precipitation, relative humidity, radiation, and  
 314 wind speed, from 1979 to 2020, to daily meteorological data at a station located near Bell 4 (San

315 Dimas Tanbark) from the U.S. Forest Service (USFS). Because gridMET matched closely with  
316 ground station data but does not require gap filling, gridMET was selected as a suitable  
317 meteorological forcing dataset for our analyses. To calibrate drainage parameters, we used  
318 streamflow data from the USFS for the years 1980 to 2002; data were missing for some months  
319 (Figure 3). We omitted 8 years of streamflow data (1984-1992) following a prescribed fire that  
320 occurred in 1984 (Meixner et al., 2006). We selected streamflow data from 1993 to 2002 for  
321 model calibration and 1980 to 1983 for validation (described in section 2.5 below).



322  
323 *Figure 3. Streamflow and climate data for Bell 4. The temperature is yearly average, and*  
324 *streamflow is calculated as the volume divided by the catchment area (0.14 km<sup>2</sup>).*

325 We aggregated a 1-m resolution Digital Elevation Model (DEM) from LiDAR to 10  
326 meters to represent topography across the watershed. To map landcover, we aggregated 1-m  
327 resolution land cover data from the National Agriculture Imagery Program (NAIP; collected on  
328 June 5, 2016) to 3-m and classified three land cover types: chaparral, live oak, and bare ground

329 (Maxwell et al., 2017). We then overlapped the 10-meter DEM with 3-meter vegetation cover  
330 data to classify aspatial patch distributions in each patch family using a k-means function  
331 (Hartigan & Wong, 1979) in R version 4.3.0 (R Core Team, 2022). This resulted in  
332 approximately 11 aspatial patches in each patch family and 375 different vegetation  
333 combinations across the watershed. We acquired soil texture data from POLARIS (Chaney et al.,  
334 2016).

335 To measure streamflow, two pressure transducers (Water level data loggers),  
336 compensated for barometric pressure (Barologgers; Solinst Canada Ltd, Georgetown, Ontario,  
337 Canada), were used to record stream stage at the Bell 4 weir. Water stage was measured at 5-  
338 minute intervals and converted to discharge using a rating curve developed for the v-notch weir.  
339 Stream samples were collected using an automatic sampler (Teledyne, ISCO model 6712C,  
340 Lincoln, Nebraska, US) set to collect 500-mL samples every 2 hours over a 48-hour period at the  
341 onset of flow. Samples were then filtered through pre-baked whatman GF/F filters and stored at -  
342 20 °C. Nitrate and ammonium concentrations were measured colorimetrically using an AQ2  
343 SEAL discrete analyzer (methods EPA-129-A and EPA-126-A).

## 344 **2.5 Model initialization, calibration, and evaluation**

345 We initialized the soil C and N pools by spinning them up to steady state (i.e., running  
346 the model until the pools stabilized). For the vegetation C and N pools, we used a target-driven  
347 method that allows vegetation to grow until it reaches target leaf area index (LAI) values from  
348 remote sensing data (Hanan et al., 2018). This method enables C and N pools to spin up  
349 mechanistically while still capturing landscape heterogeneity resulting from local resource  
350 limitations and disturbance histories. To construct a map of target LAI values, we chose the

351 clearest available NAIP image during the growing season (i.e., April 24, 2010). We then  
 352 calculated NDVI using equation 1.

$$353 \quad NDVI = \frac{\rho_{NIR} - \rho_R}{\rho_{NIR} + \rho_R} \quad (1)$$

354 In this equation,  $\rho_{NIR}$  is the reflectance in the near-infrared, and  $\rho_R$  is reflectance in the red  
 355 (Hanan et al., 2018). We then estimated LAI using a generalized NDVI-LAI model developed by  
 356 (Baret et al. 1989; equation 2).

$$357 \quad LAI = -\frac{1}{k} \times \ln \left( \frac{NDVI_{max} - NDVI}{NDVI_{max} - NDVI_{back}} \right) \quad (2)$$

358 Here,  $k$  is the extinction of solar radiation through a canopy.  $NDVI_{max}$  is the maximum NDVI  
 359 occurring in the region, and  $NDVI_{back}$  is the background NDVI (i.e., from pixels without  
 360 vegetation). We obtained  $k$  value from Smith et al. (1991) and White et al. (2000). The other  
 361 parameters were obtained for each vegetation type (Table 1).

362 *Table 1. Parameters used for calculating LAI from NDVI*

| Vegetation type | $k$   | $NDVI_{max}$ | $NDVI_{back}$ |
|-----------------|-------|--------------|---------------|
| Live oak        | 0.500 | 0.379        | -0.160        |
| Chaparral       | 0.371 | 0.372        | -0.160        |

363

364 We used observed streamflow for Bell 4 to calibrate six soil parameters: saturated  
 365 hydraulic conductivity ( $K_{sat}$ ), the decay of  $K_{sat}$  with depth (m), pore size index (b), air entry  
 366 pressure ( $\phi$ ), bypass flow to deeper groundwater storage ( $gw_1$ ), and deep groundwater drainage  
 367 rates to stream ( $gw_2$ ). We selected the best parameter set by comparing observed and modeled  
 368 streamflow using monthly Nash-Sutcliffe efficiency (NSE; Nash & Sutcliffe, 1970) and percent

369 error in annual flow estimates. NSE is used to evaluate peak flows and can range from  $-\infty$  to 1,  
 370 where 1 represents a perfect fit between modeled and observed data. Percent error is used to  
 371 compare differences between the total quantity of modeled and observed streamflow; values  
 372 closer to zero represent better fit.

373 **2.6 Sensitivity analyses and simulation scenarios:**

374 After model initialization and calibration, we used the new model framework to build in  
 375 microscale hotspots. We assumed the hotspots were evenly distributed across the landscape and  
 376 converted one bare ground patch inside of every patch family to an aspatial hotspot patch. Note  
 377 that this does not mean that there was only one hotspot in a patch family, but one aspatial patch  
 378 was used to represent the distribution (or percent cover) of microscale hotspots. If no bare  
 379 ground patches existed in the patch family, we instead converted a chaparral patch to an aspatial  
 380 hotspot patch. Because there were approximately 11 patches in each patch family, this setup  
 381 resulted in approximately 9% of each patch family (and of the overall basin) consisting of  
 382 microscale hotspots. We also assigned a loam soil texture to hotspot patches to represent the soil  
 383 physical properties that may also increase moisture retention. The default parameters used to  
 384 represent hotspot hydrological and biogeochemical dynamics are shown in Table 2.

385 *Table 2. Default parameters for hotspots.  $sh\_l$  and  $sh\_g$  control water diffusion in the*  
 386 *unsaturated zone between hotspot and non-hotspot patches, the default values promote strong*  
 387 *seasonality in hotspot soil moisture. The soil moisture threshold controls water flow in the*  
 388 *saturated zone between hotspot and non-hotspot patches; the default value promotes the*  
 389 *maximum peak streamflow  $N$ . We defined one aspatial patch as a hotspot inside of each family.*  
 390 *This leads to 9.1% cover of hotspot patches evenly distributed across the landscape.*

| Parameters  | Value                               |
|---|-------------------------------------|
| Sharing coefficient of losing water in unsaturated zone from hotspots ( $sh\_l$ ) | Dry season: 0.9<br>Wet season: 0.05 |
| Sharing coefficient of gaining water in unsaturated zone of hotspots ( $sh\_g$ )  | Dry season: 0.05<br>Wet season: 0.9 |

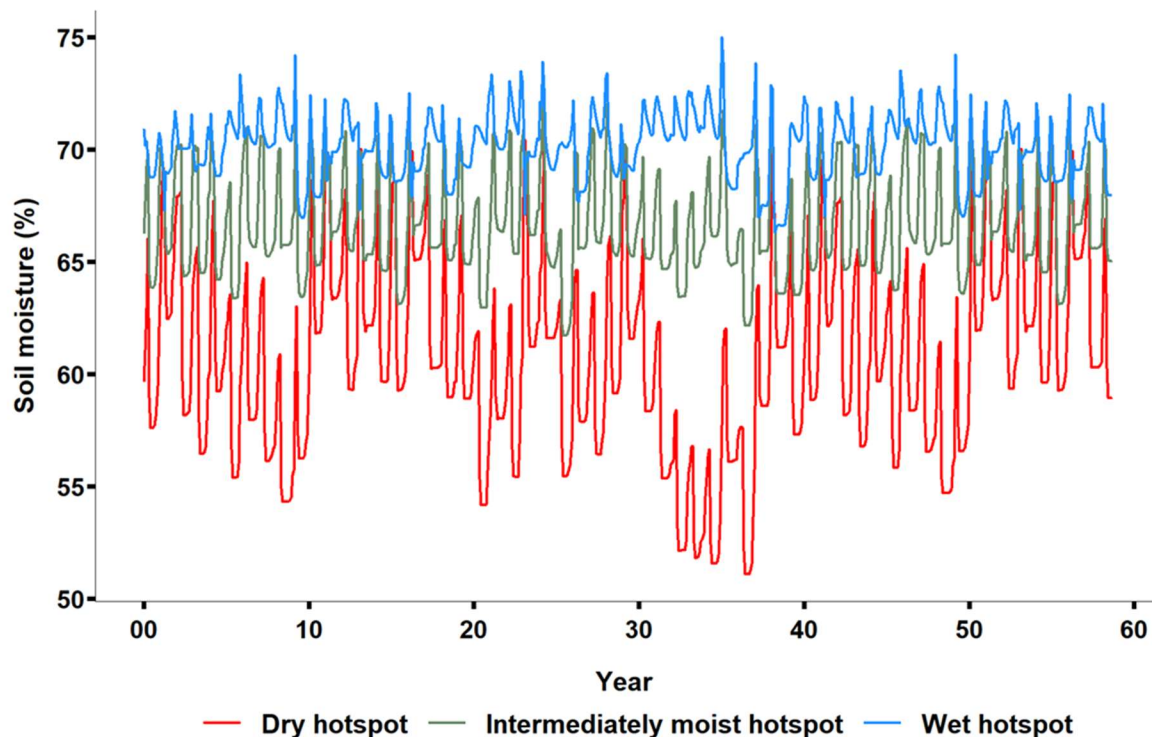
|   |      |
|---|------|
| Soil moisture threshold of non-hotspot above which water in saturated zone flows from hotspots to non-hotspot ( $\theta_{th}$ ) | 21%  |
| Percentage cover of hotspots  | 9.1% |
| Sharing coefficient of litter from non-hotspot patches to hotspot patches (coef_litter)   | 1    |

391

392 To evaluate the uncertainties related to model structure and parameters, we conducted a set of  
393 virtual experiments, or sensitivity analyses. For each sensitivity analysis, we ran RHESSys for 60  
394 years by looping the available climate data from 1979-2020. Results are presented as simulation  
395 years and capture the climate variability from the available record. First, we examined how the  
396 percentage cover of hotspots can influence N export. We built hotspot patches from zero percent  
397 to 13.7 percent at 2.3 percent increments (i.e., 0%, 2.2%, 4.5%, 6.8%, 9.1%, 11.4%, 13.7%).  
398 When the hotspot percentage was equal to 9.1%, there were exactly one aspatial hotspot patch in  
399 each patch family. When the hotspot percentage was larger than 9.1%, we needed to convert two  
400 aspatial patches in some patch families to hotspot patches. For example, the scenario with 11.4%  
401 hotspot cover at the watershed scale, required 2.3% of patch families to have two aspatial hotspot  
402 patches. Again, this does not mean that there were only one or two hotspots in a patch family,  
403 but one or two aspatial patches were used to represent their distribution.

404         Second, we investigated how the saturation status of hotspots influences nitrate export.  
405 We built three soil moisture conditions for hotspots by changing the sharing coefficients for local  
406 routing which influenced connectivity between hotspot and surrounding patches (Figure 2b): wet  
407 (sh\_l was 0.05 and sh\_g was 0.9 throughout the year; water diffused slowly from hotspots), dry  
408 (sh\_l and sh\_g were set to default values, hotspots diffused water quickly during the dry season),  
409 and intermediate (sh\_l was 0.1 and sh\_g was 0.8 during the dry season but used default values in  
410 the wet season; water diffused from hotspots at an intermediate rate). The hotspots in the wet

411 scenario were saturated almost all the time and had small interannual variation in soil moisture.  
412 The hotspots in the dry scenario lost water during dry periods and had large interannual soil  
413 moisture variation. The hotspots in the intermediate scenario had soil moisture dynamics in  
414 between the levels observed in the dry and wet scenarios (Figure 4).



415  
416 *Figure 4. Hotspot volumetric soil moisture conditions used to examine the sensitivity of N*  
417 *cycling and export to hotspot soil moisture saturation status and timing.*

418 Lastly, we examined how uncertainty in the subsurface connectivity threshold parameter,  
419 which determines when non-hotspot patches become reconnected and can receive substantial N  
420 and water from the hotspot ( $\theta_{th}$ ; Figure 2c). By establishing conditions for this larger scale  
421 connectivity, this parameter can influence streamflow nitrate export. We then compared modeled  
422 streamflow nitrate export (under a range of parameter values based on the range of basin scale  
423 soil moisture: 0.15, 0.21, 0.25, 0.31, 0.35) to observed data (from 1988 to 2001).

424           Following the sensitivity analyses, we used available data and literature to estimate the  
425 most likely value for these parameters. We selected hotspot abundance of 9.1% assuming every  
426 patch family had the same hotspot coverage (using the default value in Table 2). We then  
427 selected the “dry” hotspot scenario in order to most closely match the seasonality of N dynamics  
428 observed in dryland ecosystems (Parker & Schimel 2011). Finally, as a simple optimization  
429 strategy, we selected a value for the soil moisture threshold parameter that enabled us to best  
430 capture observed peak N export. Then using these values, we conducted modeling scenarios to  
431 investigate how biogeochemical hotspots influence N export.

432           Modeling scenarios were based on the presence or absence of biogeochemical hotspots.  
433 For the hotspot scenario, we used the optimized soil moisture threshold determined using the  
434 approach described above, along with default parameters shown in Table 2, which created “dry”  
435 hotspots (i.e., with rapid water diffusion) that had distinct seasonality in denitrification as  
436 observed in field data (Li et al., 2006; Parker & Schimel, 2011). In this scenario, the hotspot  
437 patches received litter and protected C and N from vegetated patches and both biogeochemical  
438 and hydrologic processes still occurred within the hotspot patches. For the non-hotspot scenario,  
439 we used unvegetated patches in place of the hotspot patches, which were initialized to zero.  
440 However, in these unvegetated patches, we did not route litter and recalcitrant soil C and N from  
441 the vegetated patches. As a result, only hydrologic processes occurred there. We ran these two  
442 scenarios for 120 years, 60 years to stabilize the hotspot patches, and another 60 years to  
443 compare differences between scenarios.

## 444 **3 Results**

### 445 **3.1 Initialization and calibration results**

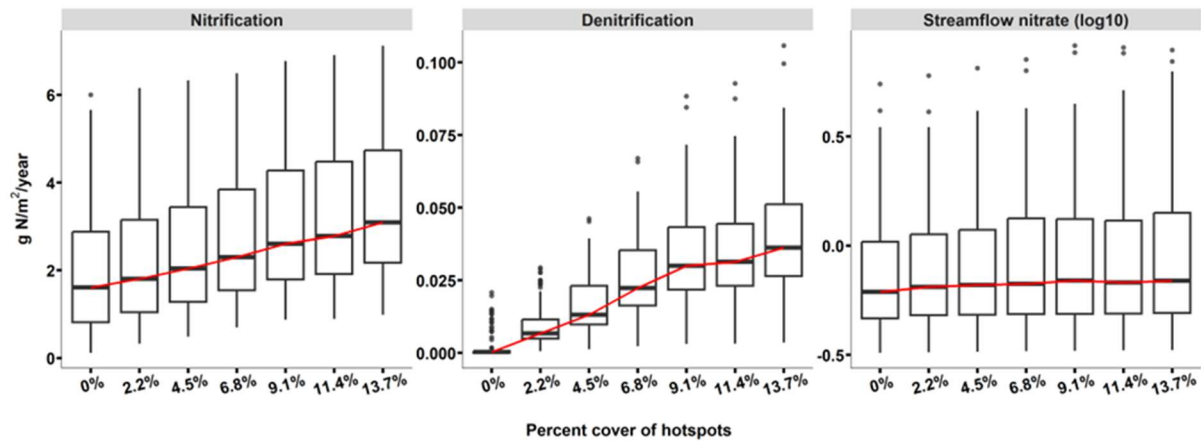
446 Using the target-driven initialization method of Hanan et al. (2018), we were able to  
447 capture the spatial distribution of leaf area index (LAI) and associated C stores across the Bell 4  
448 watershed, with some minor underestimates in riparian areas (covered by live oak) and  
449 overestimates in a small percentage of patches, which occurred because RHESSys allocates C to  
450 LAI at the end of growing season. Overall, the initialized and remotely sensed LAI were a strong  
451 match (Figure S1).

452 During the calibration period, the monthly NSE (a metric to evaluate the extent to which  
453 models capture peak streamflow; values close to 1 represent the best correspondence between  
454 modeled and observed values) was 0.88. Percent error (a metric to evaluate total flow; values  
455 close to 0 represent low error in the total amount of streamflow for modeled vs. observed data)  
456 was 5.45%. For the evaluation period, the monthly NSE was 0.8 with a percent error of -3.92%.  
457 In general, the model captured the seasonality, recession, and low flow patterns observed in the  
458 streamflow record.

### 459 **3.2 Sensitivity of N fluxes to the abundance of hotspots**

460 Total N export increased with increasing hotspot cover and then reached an asymptote  
461 when hotspot cover was greater than 9.1% (Figure 5). Denitrification rates were very low in the  
462 zero percent hotspot cover scenario and increased with an increasing percentage of hotspot  
463 patches. However, the rate of increase declined when hotspot cover was greater than 9.1%.  
464 Median streamflow nitrate export began increasing when hotspot cover was above 4.5% but  
465 reached an asymptote at 9.1%. Maximum streamflow nitrate export also increased with  
466 increasing hotspot cover, but the rate of increase declined when cover was above 9.1%. This

467 occurred because increasing hotspot cover led to concomitant decreases in vegetation cover and  
 468 therefore less carbon and nitrogen inputs from vegetation to soil. As a result, N cycling processes  
 469 became limited by productivity of the patch family. Although this result was partly an artifact of  
 470 the model's structure—which resulted in more than one aspatial hotspot patch occurring in some  
 471 patch families when the hotspot percentage cover exceeded 9.1%—it still demonstrates the  
 472 mechanism by which increases in hotspot cover above a given threshold can decrease  
 473 productivity. However, the actual threshold value should be interpreted with caution.



474

475 *Figure 5. Sensitivity of N processes to the percent cover of hotspots. Box plots show 25<sup>th</sup>,*  
 476 *median, and 75<sup>th</sup> percentile values, and the red line connects the median of each scenario to show*  
 477 *trends. Streamflow nitrate is calculated as total mass of nitrate in discharge divided by the basin*  
 478 *area.*

479 **3.3 The sensitivity of N fluxes to the parameters controlling water diffusion during periods**  
 480 **of hydrologic disconnection.**

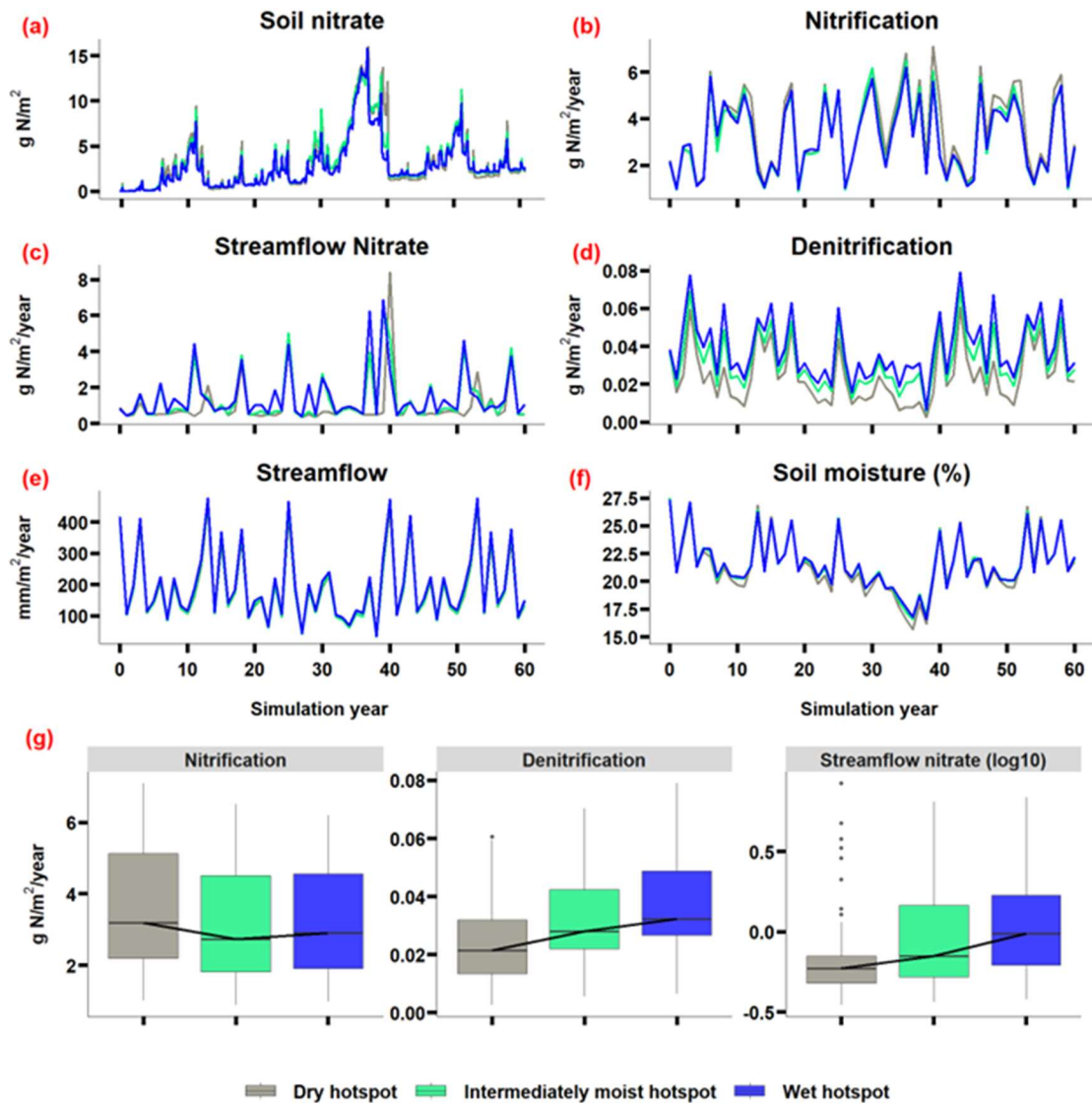
481 To examine how the rate at which hotspots dry out during periods of hydrologic  
 482 disconnection influences N fluxes, we ran three scenarios: a scenario where soil moisture in the  
 483 hotspots diffused slowly to non-hotspot patches and hotspots retained their soil moisture  
 484 throughout the year (i.e., a wet hotspot scenario), and a scenario where the diffusion speed was  
 485 intermediate (i.e., an intermediately moist hotspot scenario), and a scenario where soil moisture

486 diffused relative quickly from hotspot to non-hotspot patches (i.e., a dry hotspot scenario). We  
487 found that basin-scale nitrification rates can increase or decrease with the moisture content of  
488 hotspots (Figure 6 b&g). Higher moisture content in hotspots led to relatively lower moisture  
489 content in non-hotspot patches (based on water balance). In the wet-hotspot scenario, basin-scale  
490 nitrification was lower than in the dry-hotspot scenario where water slowly diffused to non-  
491 hotspot patches. This occurred because in the wet-hotspot scenario, soil moisture in non-hotspot  
492 patches was lower, which reduced total nitrification, even though nitrification rates increased in  
493 the hotspots.

494 Basin-scale denitrification increased with higher moisture content in hotspots since  
495 denitrification mainly occurs in those locations (Figure 6 d&g). For both nitrification and  
496 denitrification, the differences between the three scenarios were most pronounced during dry  
497 years when soil moisture differences between hotspots and non-hotspot patches were higher  
498 (Figure 6 b&d). During dry and average years, streamflow nitrate export was higher in the  
499 scenarios where hotspots remained saturated or close to saturated (i.e., the wet- and  
500 intermediately-moist- hotspot scenarios) than in the scenario where water diffused rapidly during  
501 dry periods (i.e., the dry-hotspot scenario). However, there was higher total annual and peak  
502 streamflow nitrate export during the wet years in the dry-hotspot scenario especially after  
503 multiple dry years (Figure 6c&e). Altogether, the closer hotspots are to being water-saturated,  
504 the more quickly N is exported to streamflow.

505 During multiple dry years, for the rapid diffusion (dry hotspot) scenario, nitrate  
506 accumulated in the saturated zone. Once a wet year occurred, that nitrate was flushed out to  
507 streams (Figure 6a). In the more continuously saturated (wet hotspot) hotspot scenario, higher  
508 denitrification, and faster leaching of nitrate from hotspots led to less nitrate accumulation in the

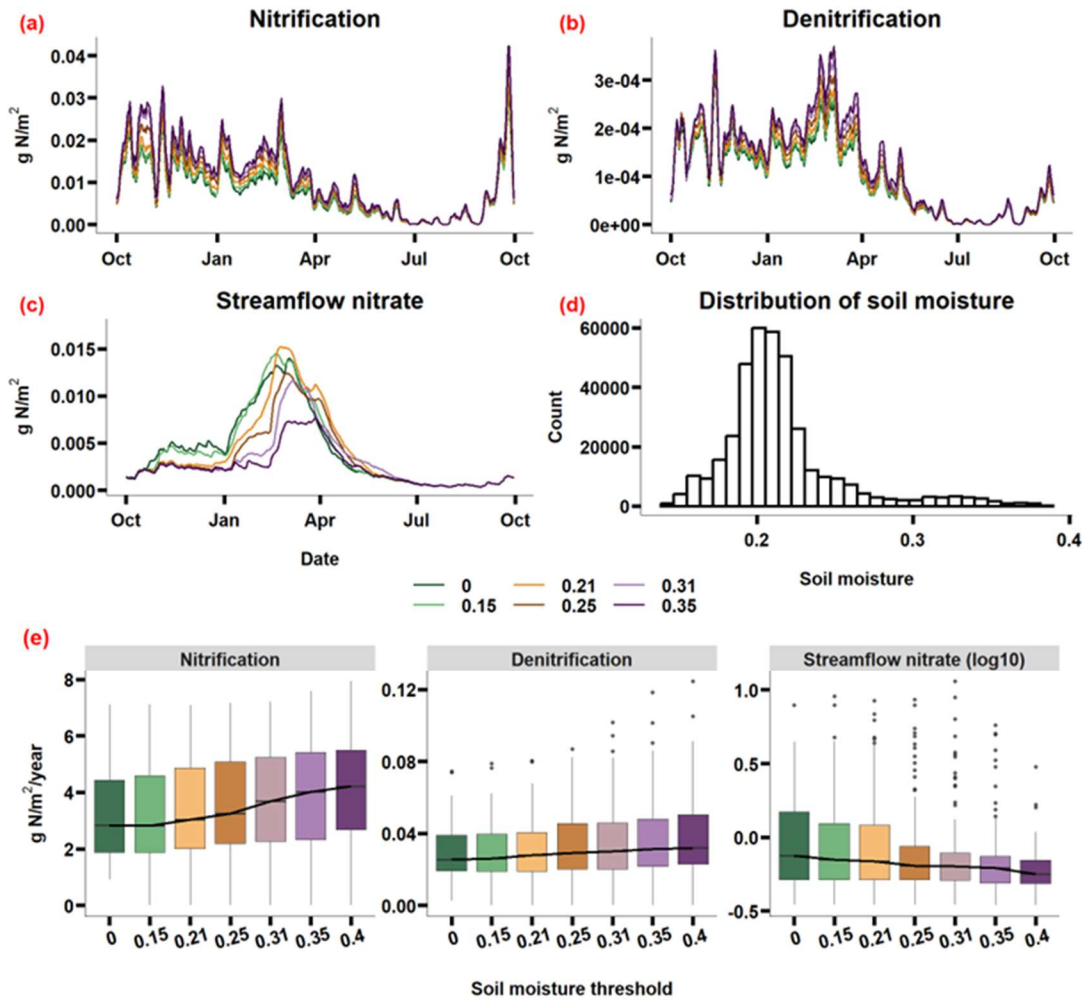
509 saturated zone. This suggests that soil moisture in hotspots and the subsurface flow interact to  
 510 drive N movement from soil to streams.



511  
 512 *Figure 6. N processes for three different scenarios, one where hotspots were saturated most of*  
 513 *the time (i.e., the slow diffusion, wet hotspot scenario), one where water diffused more rapidly*  
 514 *from hotspots during the dry season (i.e., the rapid diffusion, dry hotspot scenario), and one*  
 515 *where diffusion was intermediate (i.e., the intermediately moist hotspot scenario). Streamflow is*  
 516 *calculated as the average water depth over the basin area of Bell 4 (0.14 km<sup>2</sup>). Panel (g) is the*  
 517 *distribution of annual N fluxes, box plots show 25<sup>th</sup>, median, 75<sup>th</sup> percentile, and the black line*  
 518 *connects the median of each scenario.*

### 519 3.4 Sensitivity of N export to the subsurface connectivity parameter

520 The soil moisture threshold, which controls the connectivity of hotspots to non-hotspot  
521 patches, had a stronger influence on streamflow nitrate export than on nitrification and  
522 denitrification fluxes (Figure 7). This occurred because streamflow N export is influenced by  
523 both soil moisture content and subsurface lateral transport. Thus, when the threshold was high  
524 (i.e., when more moisture was required to establish hydrologic connectivity), streamflow N  
525 export was close to zero. With a higher soil moisture threshold, hotspots also tended to have  
526 higher moisture content, which increased nitrification and denitrification (Figure 7e), although  
527 the increases were small. The soil moisture threshold affected both the magnitude and timing of  
528 streamflow nitrate export. At a very low threshold of 0.15, there was higher magnitude and  
529 similar timing of peak nitrate export to streams compared to the no-threshold scenario (fully  
530 connected). This occurred because soil moisture in non-hotspot patches was higher than 0.15  
531 most of the time (Figure 7d). A threshold of 0.21, which was around the median basin-scale soil  
532 moisture, caused the largest peak in streamflow nitrate export. This occurred because  
533 connectivity was delayed until the threshold was reached, allowing nitrate to accumulate. When  
534 the threshold was larger than 0.21, peak streamflow nitrate was smaller and came later because  
535 hotspots were disconnected from non-hotspot patches most of the time.



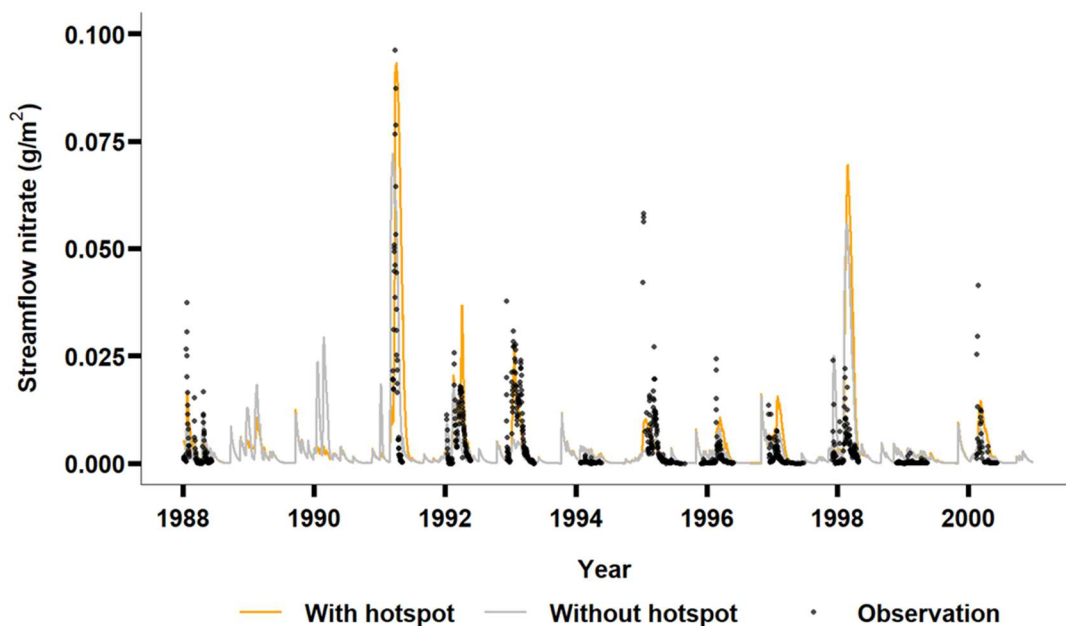
536

537 Figure 7. Sensitivity of N fluxes to the soil moisture threshold. Panels (a), (b) and (c) are mean  
 538 daily N fluxes over 60 years. Panel (d) is the distribution of daily soil moisture at the basin scale  
 539 over 60 years. Panel (e) is the distribution of annual fluxes, box plots show 25<sup>th</sup>, median, 75<sup>th</sup>  
 540 percentile, and the black line connects the median of each scenario. Different colors represent  
 541 different soil moisture thresholds.

### 542 3.5 Prediction of streamflow N export compared with observations.

543 We selected the optimal soil moisture threshold from section 3.2 for capturing the  
 544 magnitude of observed nitrate export (i.e., 0.21; this parameter value maximized peak  
 545 streamflow nitrate export) and we used the default values shown in Table 2 for the other  
 546 parameters. Using these values, we found that hydrologic disconnection of soil hotspots during  
 547 the dry periods and reconnection during wet periods enabled us to capture the observed

548 magnitude of nitrate export in streamflow, which we could not otherwise capture in the non-  
549 hotspot scenario (Figure 8). For example, the non-hotspot scenario underestimated nitrate export  
550 with a NSE of 0.22, while the hotspot scenario increased the estimation peak streamflow nitrate  
551 by 29% and captured its timing better with a NSE of 0.4 (in 1988, 1991, 1992, 1993, 2000).  
552 However, after optimizing the moisture threshold parameter, the timing of stream nitrate export  
553 was still slightly off; for example, in 1998, the modeled stream nitrate export peak was higher  
554 and occurred slightly later than observed.



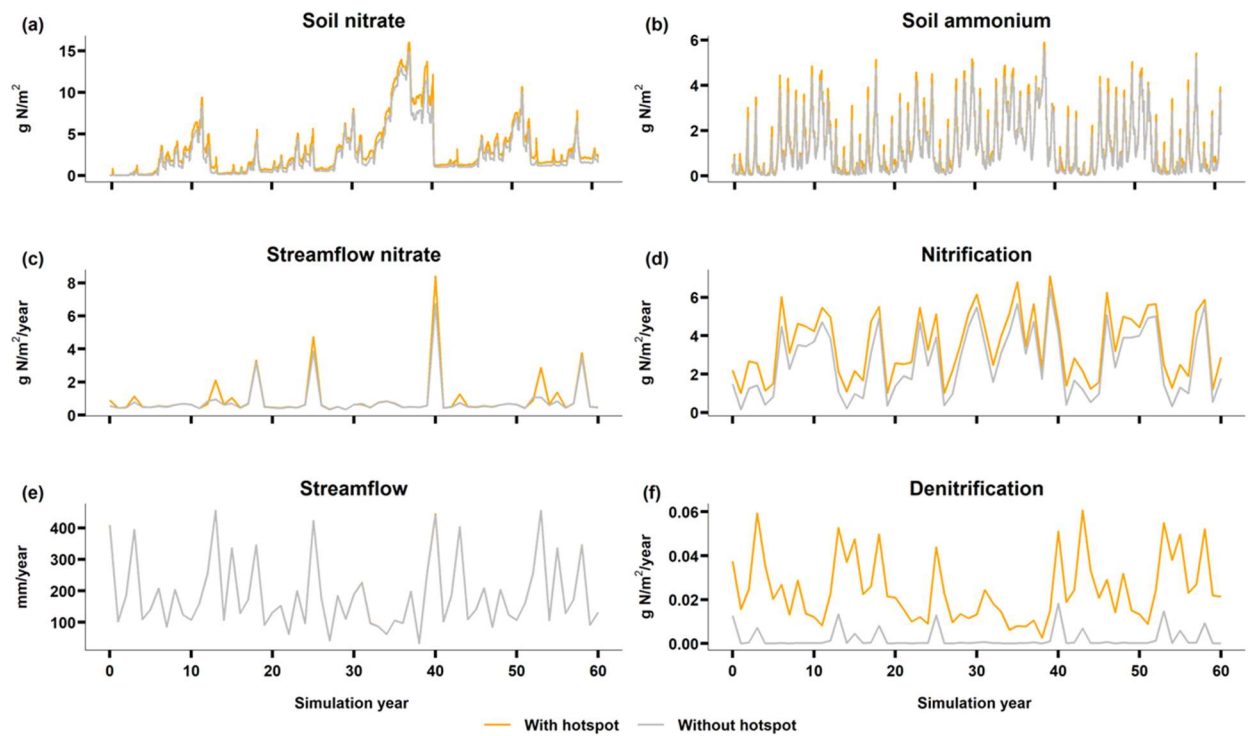
555

556 *Figure 8. Simulated and observed nitrate export in streamflow. The dots show observed*  
557 *streamflow nitrate.*

### 558 **3.6 Comparison of hotspot and non-hotspot scenarios**

559 At the basin-scale, there was higher N export in the hotspot scenario than in the non-  
560 hotspot scenario (Figure 9). Increases in streamflow nitrate with the hotspot scenario closely  
561 corresponded with increases in soil nitrate. Nitrate accumulated during dry years and there was  
562 substantial nitrate export to streams in wet years, especially when a wet year followed multiple

563 dry years (e.g., in year 40). We also found that streamflow nitrate export was further influenced  
 564 by interannual precipitation patterns. The differences between the hotspot and non-hotspot  
 565 scenarios were most evident during wet years when the basin was more connected. During wet  
 566 years, more nitrate was flushed out from hotspots, which illustrates how subsurface connectivity  
 567 can be an important factor driving streamflow N export. Consequently, the differences in  
 568 streamflow nitrate between the hotspot and non-hotspot scenarios were less consistent than the  
 569 differences in nitrification and denitrification, which had similar temporal patterns but differing  
 570 magnitude (e.g., Figure 9 c&d).



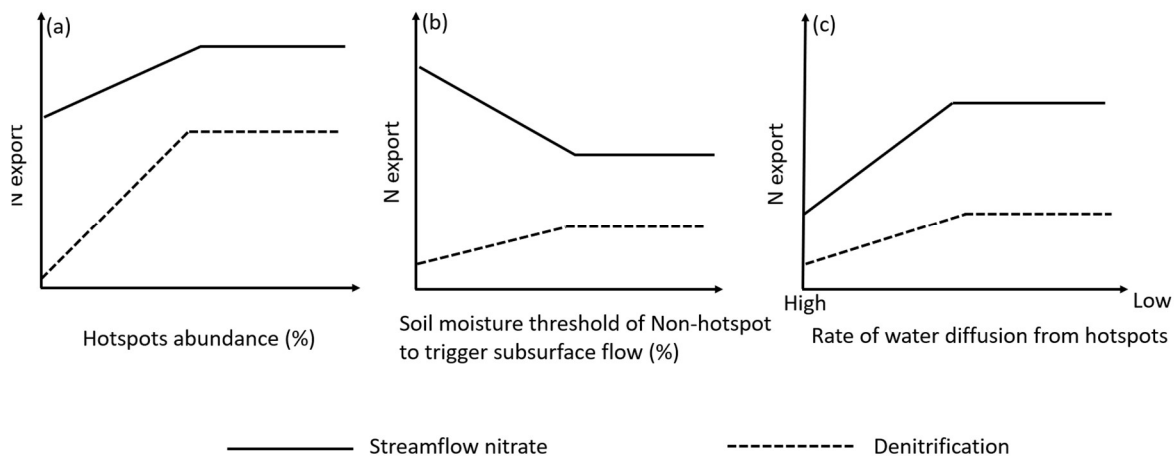
571

572 *Figure 9. Nitrogen and hydrologic cycling processes (annual sum) and nitrate pools (annual*  
 573 *mean) at the full basin scale for Bell 4.*

574 **4 Discussion**

575 Modeling hotspots at watershed scales has been challenging because most models,  
 576 including RHESSys, lack corresponding fine-scale (e.g., below 1-meter resolution) parameters

577 and variables (Tague, 2009). To address this limitation, we developed a framework for  
 578 representing hotspots aspatially within 10-m resolution patches. Using this framework, we  
 579 conducted a series of virtual experiments to investigate how uncertainties in model structure and  
 580 parameters influence N cycling and export. Then using the new modeling framework, we  
 581 examined how precipitation can affect N export in a dryland watershed in California. Our model  
 582 framework and virtual experiments improve our ability to connect plot-scale measurements to  
 583 catchment scale projections by developing integrative model algorithms and parameters that  
 584 control the biophysical behavior of hotspots across a landscape. These parameters can be  
 585 optimized using field observations of N cycling and export. We illustrate how uncertainty in  
 586 model parameters can influence projections of N export. Future research should aim to reduce  
 587 these uncertainties, and ultimately represent hotspot behavior more mechanistically across  
 588 watersheds.



589  
 590 *Figure 10. Conceptual framework summarizing how total annual streamflow nitrate and*  
 591 *denitrification respond to (a) hotspots abundance, (b) the soil moisture threshold required to*  
 592 *trigger subsurface flow, and (c) the rate of water diffusion from hotspots.*

#### 593 4.1. Uncertainties related to hotspot abundance and distribution

594 Estimating nitrogen (N) export at watershed and regional scales is limited by uncertainty  
595 in how hotspots are distributed across landscapes. Our research is among the few studies that  
596 have evaluated how hotspot abundance influences watershed-scale N export and illustrates the  
597 need to quantify hotspot cover to effectively scale N dynamics from ecosystems to watersheds  
598 (Anderson et al., 2015; Groffman, 2012). We parameterized the hotspots with varying cover  
599 percentages across a small watershed (0.14 km<sup>2</sup>) and found that N export increased with hotspot  
600 abundance (Figure 5& Figure 10), but with an asymptotic relationship due to limitations in N  
601 inputs and plant productivity (i.e., energy input for denitrification). However, in less N-limited  
602 and more mesic sites (e.g., under elevated N deposition and increasing precipitation), N export  
603 may be more sensitive to increasing hotspot abundance.

604 One limitation of our study is that we did not examine how the spatial distribution of  
605 hotspots influences N export. Previous research has shown that hotspots can be more  
606 concentrated in riparian corridors and wetlands where moisture content is higher (Pinay et al.,  
607 2015). We did however find that wet hotspots, which may serve as a surrogate for riparian and  
608 wetland locations, can in some cases increase both denitrification and N export in streams  
609 (Figure 6). However, because the location and arrangement of hotspots across a landscape can  
610 significantly influence streamflow N export (Laudon et al., 2011; Pinay et al., 2015), more  
611 research is needed to understand these spatial relationships (Haas et al., 2013). For example,  
612 combining high-resolution remote sensing data with field observations may help us better constrain  
613 hotspot distribution and abundance in ecohydrological models (Goodridge et al., 2018;  
614 Groffman, 2012; Tague, 2009; Walter et al., 2000).

## 615 4.2 Uncertainties in how rapidly hotspots dry out

616 Soil moisture is a major factor regulating denitrification and streamflow nitrate export  
617 (Pinay et al., 2015; Zhu et al., 2012). Our modeling experiments illustrate how the relationships  
618 between soil moisture and N dynamics can be complex and non-linear. Elevated soil moisture  
619 may reduce nitrification, increase denitrification, and ultimately decrease the amount of nitrate  
620 available for hydrologic flushing. Drier soils on the other hand can decrease denitrification and  
621 increase the amount of nitrate available for flushing (Homyak et al., 2016). We found that during  
622 dry and average years, higher moisture in hotspots increased nitrate infiltration from the  
623 unsaturated zone to the saturated zone, resulting in elevated and more rapid nitrate export to  
624 streams (Figure 6c). However, during wet years, higher soil moisture led to less nitrate export to  
625 streams due to increases in denitrification combined with less nitrate in the subsurface from the  
626 legacy effects of leaching in prior average and dry years. The dry hotspot scenario captured the  
627 observed nitrate-flushing better than the wet scenario, suggesting that hotspots are not likely to  
628 be continuously saturated (Figure 6). Because recent studies have shown that very small changes  
629 in soil moisture can change N fluxes abruptly (Castellano et al., 2013; Evans et al., 2016), it is  
630 important to improve our representation of soil moisture conditions in hotspots to accurately  
631 predict nitrate export.

632 Soil water residence time is an important factor affecting N export (Pinay et al., 2015;  
633 Zarnetske et al., 2011). The slower water diffuses from hotspots, the longer nitrate is exposed to  
634 denitrifying conditions (McClain et al., 2003). Our study shows that longer water residence time  
635 in hotspots (i.e., in the wet hotspot scenario) increases both denitrification and total N export to  
636 streams (Figure 6 & Figure 10). We used water diffusion coefficients to model water residence  
637 time in hotspots and we selected coefficients that enabled us to best capture the plausible timing

638 of denitrification and streamflow N fluxes. While this is a simplified, proxy approach, adding  
639 further complexity by explicitly modeling diffusion maybe infeasible since it would require  
640 local, spatially explicit soil parameters (Wood et al., 2011). However, further investigation into  
641 how proxy parameters may be calibrated is recommended for future research.

642 Stream nitrate export was also affected by precipitation patterns. When there were  
643 multiple dry years in a row, nitrate accumulated to a greater extent than in average years (Figure  
644 6a). When a wet year followed a multi-year drought, there was higher streamflow nitrate export  
645 in the dry hotspot scenario (Figure 6c). This is corroborated by field observations, which suggest  
646 that severe drought promoted nitrate accumulation in soil due to less denitrification and plant  
647 uptake, resulting in more nitrate available for flushing with the return of precipitation (Winter et  
648 al. 2023). We found that the length of drought and precipitation variability were more important  
649 in driving streamflow N export than the amount of precipitation (Figure 6c&e). For example,  
650 even with similar amount of precipitation in simulation years 26 and 40, N export was much  
651 higher in year 40 due to the legacy of a multi-year drought (Figure 6c&e). Recent research has  
652 similarly shown that precipitation variability can have positive or negative legacy effects on  
653 dryland productivity, which can in turn influence N cycling and export (Gherardi & Sala, 2015;  
654 Krichels et al., 2022). However, the direction of N responses vary along long-term precipitation  
655 gradients (Gherardi & Sala, 2015, 2019).

#### 656 **4.3 Uncertainties in hydrologic connectivity**

657 The subsurface flow threshold also plays a role in how much nitrate is transported to  
658 streams. In this study, we found that the optimal volumetric soil moisture to trigger subsurface  
659 flow from hotspot to non-hotspot patches was around 21% (Figure 7). Other studies have  
660 similarly shown that to trigger a subsurface flow, the soil moisture needs to reach a threshold of

661 18% (Liao et al., 2016). However, this threshold may vary with soil texture and water potential  
662 dynamics. While our new model framework can improve the prediction of streamflow nitrate  
663 with a static soil moisture threshold, topography and vegetation cover can also influence the  
664 connectivity and amount of subsurface flow, suggesting that soil moisture thresholds should be  
665 dynamic (Crow et al., 2012, Zhu et al., 2018).

666 Coupling soil biogeochemical models with hydrological models has become increasingly  
667 popular for investigating N cycling and export (Schimel, 2018). To save time, researchers  
668 typically prefer to couple existing models rather than build new ones (Malek et al., 2017; Zhu et  
669 al., 2018). Since most hydrologic models do not account for fine-scale heterogeneity in available  
670 moisture, they may not be able to capture biogeochemical hotspots even when coupled with  
671 biogeochemical models (Chen et al., 2020). Our new model framework provides a relatively  
672 simple way to capture hotspots without having to explicitly represent sub-meter scale spatial  
673 heterogeneity. While this intermediate complexity approach enables us to represent hotspots  
674 across a watershed, it does not fully capture some of the potential controls on hotspot function.  
675 For example, although our model captured the variability and magnitude of streamflow nitrate,  
676 there was some error associated with its timing (Figure 8). Future work can build upon our  
677 simple hotspot model to develop more process-based and dynamic representation of subsurface  
678 flow thresholds. This can be achieved by improving our understanding of hydrology and N  
679 processes in soil through hydrogeochemical observations.

#### 680 **4.4 The role of hotspots and hot moments in watershed models**

681 We found that the catchment-scale denitrification rate in the hotspot scenarios was  
682 significantly higher than that observed in the non-hotspot scenario (Figure 5& Figure 9), aligning  
683 with the concept that small areas often account for a high percentage of denitrification activity

684 (McClain et al., 2003). Additionally, denitrification was more sensitive to hotspot abundance,  
685 while N export to streams was more sensitive to the soil moisture threshold that triggers  
686 subsurface flow (Figure 10). Both are affected by the speed at which water diffuses from  
687 hotspots, which influences soil moisture levels, water residence time in soil, and vertical and  
688 horizontal transport of water. Our virtual experiments provide information on model uncertainty  
689 and sensitivity that can inform future studies focused on scaling N processes from plots to  
690 catchments. For example, in areas with high N deposition, managers who are interested in  
691 predicting how much N ends up in streams should focus on reducing model uncertainties in  
692 subsurface flow thresholds and soil moisture retention in hotspots.

693         In the context of predicting N export, hot moments—defined as wet periods after a  
694 prolonged dry spell (Groffman et al., 2009)—are currently better represented in the RHESSys  
695 model than hotspots. Even in our no hotspot scenario, there was a pulse of streamflow N export  
696 when wet years followed multiple dry years (Figure 6 & Figure 9). However, models of how hot  
697 moments influence streamflow N export are still limited by uncertainties in soil moisture  
698 dynamics. For instance, we found that in the wet hotspot scenario, there was an earlier  
699 streamflow N pulse than in the dry hotspot scenario (Figure 6c). Thus, hotspot conditions can  
700 affect the timing of hot moments, which has not been previously explored in modeling studies. In  
701 future studies, it is important to consider interactions between hotspots and hot moments rather  
702 than discussing them in isolation.

## 703 **5 Conclusion**

704         Coupling hydrologic processes with biogeochemical processes in watershed-scale models  
705 is challenging due to subsurface heterogeneity and the existence of hotspots and hot moments  
706 that are not well represented in models. We developed a framework for representing hotspots

707 explicitly in dryland watersheds and using this framework, we demonstrated how hydrologic  
708 connectivity and precipitation can affect N export in a dryland watershed in California. With  
709 increasing hotspot coverage (up to a threshold), both denitrification and N export to streams  
710 increased. The partitioning between denitrification and N-export, and the timing and magnitude  
711 of N-export were largely controlled by hotspot soil moisture dynamics. Specifically, we found  
712 that when the soil moisture threshold required for reestablishing subsurface flow was  
713 intermediate, nitrate was able to accumulate during drier periods and then be flushed to the  
714 stream upon wet up. This led to the highest peak nitrate export to streams, which tended to  
715 better-capture observed nitrate patterns. To our knowledge, this is the first time biogeochemical  
716 hotspots have been modeled explicitly using a coupled biogeochemical-ecohydrological model in  
717 a dryland watershed. This modeling framework can help better project N export in dryland  
718 watersheds where hotspots may play an increasingly important role in governing water quality as  
719 drought and N deposition continue to increase.

## 720 **6 Acknowledgments**

721 This project was supported by National Science Foundation of the United States under award  
722 number DEB-1916658. We thank Tom Dilts for helping with preparing input maps and data of  
723 RHESSys. We thank Pete Wohlgemuth for helping with streamflow data processing and model  
724 calibration. This study was supported in part by the USDA Forest Service Rocky Mountain  
725 Research Station. The findings and conclusions in this publication are those of the author and  
726 should not be construed to represent any official USDA or U.S. Government determination or  
727 policy.

## 728 **Conflict of Interest**

729 The authors declare no conflicts of interest relevant to this study.

### 730 **Data Availability Statement**

731 The data sets used to run simulations for this study can be found in the Open Science Forum:

732 <https://osf.io/ukpjpg/>, and the model code can be found on GitHub:

733 <https://doi.org/10.5281/zenodo.7754375>.

### 734 **References**

735 Abatzoglou, J. T. (2013). Development of gridded surface meteorological data for ecological

736 applications and modelling. *International Journal of Climatology*, 33(1), 121–131.

737 <https://doi.org/10.1002/joc.3413>

738 Anderson, T. R., Groffman, P. M., & Walter, M. T. (2015). Using a soil topographic index to

739 distribute denitrification fluxes across a northeastern headwater catchment. *Journal of*

740 *Hydrology*, 522, 123–134. <https://doi.org/10.1016/j.jhydrol.2014.12.043>

741 Baret, F., Olioso, A., Luciani, J. L., Hanocq, J. F., & Monterrot, J. C. (1989). Estimation à partir

742 de mesures de réflectance spectrale du rayonnement photosynthétiquement actif absorbé

743 par une culture de blé. *Agronomie*, 9(9), 885–895. <https://doi.org/10.1051/agro:19890906>

744 Borer, E. T., & Stevens, C. J. (2022). Nitrogen deposition and climate: an integrated synthesis.

745 *Trends in Ecology & Evolution*. <https://doi.org/10.1016/j.tree.2022.02.013>

746 Burke, W. D., Tague, C., Kennedy, M. C., & Moritz, M. A. (2021). Understanding How Fuel

747 Treatments Interact With Climate and Biophysical Setting to Affect Fire, Water, and

748 Forest Health: A Process-Based Modeling Approach. *Frontiers in Forests and Global*

749 *Change*, 3. <https://doi.org/10.3389/ffgc.2020.591162>

750 Castellano, M. J., Lewis, D. B., & Kaye, J. P. (2013). Response of soil nitrogen retention to the  
751 interactive effects of soil texture, hydrology, and organic matter. *Journal of Geophysical*  
752 *Research: Biogeosciences*, *118*(1), 280–290. <https://doi.org/10.1002/jgrg.20015>

753 Chaney, N. W., Wood, E. F., McBratney, A. B., Hempel, J. W., Nauman, T. W., Brungard, C.  
754 W., & Odgers, N. P. (2016). POLARIS: A 30-meter probabilistic soil series map of the  
755 contiguous United States. *Geoderma*, *274*, 54–67.  
756 <https://doi.org/10.1016/j.geoderma.2016.03.025>

757 Chen, X., Tague, C. L., Melack, J. M., & Keller, A. A. (2020). Sensitivity of nitrate  
758 concentration-discharge patterns to soil nitrate distribution and drainage properties in the  
759 vertical dimension. *Hydrological Processes*, *34*(11), 2477–2493.  
760 <https://doi.org/10.1002/hyp.13742>

761 Clark, M. P., Bierkens, M. F. P., Samaniego, L., Woods, R. A., Uijlenhoet, R., Bennett, K. E., et  
762 al. (2017). The evolution of process-based hydrologic models: historical challenges and  
763 the collective quest for physical realism. *Hydrology and Earth System Sciences*, *21*(7),  
764 3427–3440. <https://doi.org/10.5194/hess-21-3427-2017>

765 Crow, W. T., Berg, A. A., Cosh, M. H., Loew, A., Mohanty, B. P., Panciera, R., et al. (2012).  
766 Upscaling sparse ground-based soil moisture observations for the validation of coarse-  
767 resolution satellite soil moisture products. *Reviews of Geophysics*, *50*(2).  
768 <https://doi.org/10.1029/2011RG000372>

769 Dunn, P. H., Barro, S. C., Wells, W. G., Poth, M. A., Wohlgenuth, P. M., & Colver, C. G.  
770 (1988). *The San Dimas experimental forest: 50 years of research* (No. PSW-GTR-104)  
771 (p. PSW-GTR-104). Berkeley, CA: U.S. Department of Agriculture, Forest Service,

772 Pacific Southwest Forest and Range Experiment Station. <https://doi.org/10.2737/PSW->  
773 GTR-104

774 Eagleson, P. S. (1978). Climate, soil, and vegetation: 3. A simplified model of soil moisture  
775 movement in the liquid phase. *Water Resources Research*, 14(5), 722–730.  
776 <https://doi.org/10.1029/WR014i005p00722>

777 Ebrahimi, A., & Or, D. (2018). On Upscaling of Soil Microbial Processes and Biogeochemical  
778 Fluxes From Aggregates to Landscapes. *Journal of Geophysical Research:*  
779 *Biogeosciences*, 123(5), 1526–1547. <https://doi.org/10.1029/2017JG004347>

780 Evans, S., Dieckmann, U., Franklin, O., & Kaiser, C. (2016). Synergistic effects of diffusion and  
781 microbial physiology reproduce the Birch effect in a micro-scale model. *Soil Biology and*  
782 *Biochemistry*, 93, 28–37. <https://doi.org/10.1016/j.soilbio.2015.10.020>

783 Fenn, M. E., Baron, J. S., Allen, E. B., Rueth, H. M., Nydick, K. R., Geiser, L., et al. (2003).  
784 Ecological Effects of Nitrogen Deposition in the Western United States. *BioScience*,  
785 53(4), 404–420. [https://doi.org/10.1641/0006-3568\(2003\)053\[0404:EEONDI\]2.0.CO;2](https://doi.org/10.1641/0006-3568(2003)053[0404:EEONDI]2.0.CO;2)

786 Gherardi, L. A., & Sala, O. E. (2015). Enhanced precipitation variability decreases grass- and  
787 increases shrub-productivity. *Proceedings of the National Academy of Sciences*, 112(41),  
788 12735–12740. <https://doi.org/10.1073/pnas.1506433112>

789 Gherardi, L. A., & Sala, O. E. (2019). Effect of interannual precipitation variability on dryland  
790 productivity: A global synthesis. *Global Change Biology*, 25(1), 269–276.  
791 <https://doi.org/10.1111/gcb.14480>

792 Goodridge, B. M., Hanan, E. J., Aguilera, R., Wetherley, E. B., Chen, Y.-J., D'Antonio, C. M.,  
793 & Melack, J. M. (2018). Retention of Nitrogen Following Wildfire in a Chaparral  
794 Ecosystem. *Ecosystems*, 21(8), 1608–1622. <https://doi.org/10.1007/s10021-018-0243-3>

795 Groffman, P. M. (2012). Terrestrial denitrification: challenges and opportunities. *Ecological*  
796 *Processes*, 1(1), 1–11. <https://doi.org/10.1186/2192-1709-1-11>

797 Groffman, P. M., Butterbach-Bahl, K., Fulweiler, R. W., Gold, A. J., Morse, J. L., Stander, E. K.,  
798 et al. (2009). Challenges to incorporating spatially and temporally explicit phenomena  
799 (hotspots and hot moments) in denitrification models. *Biogeochemistry*, 93(1–2), 49–77.  
800 <https://doi.org/10.1007/s10533-008-9277-5>

801 Gustine, R. N., Hanan, E. J., Robichaud, P. R., & Elliot, W. J. (2022). From burned slopes to  
802 streams: how wildfire affects nitrogen cycling and retention in forests and fire-prone  
803 watersheds. *Biogeochemistry*, 157(1), 51–68. [https://doi.org/10.1007/s10533-021-00861-](https://doi.org/10.1007/s10533-021-00861-0)  
804 [0](https://doi.org/10.1007/s10533-021-00861-0)

805 Haas, E., Klatt, S., Fröhlich, A., Kraft, P., Werner, C., Kiese, R., et al. (2013). LandscapeDNDC:  
806 a process model for simulation of biosphere–atmosphere–hydrosphere exchange  
807 processes at site and regional scale. *Landscape Ecology*, 28(4), 615–636.  
808 <https://doi.org/10.1007/s10980-012-9772-x>

809 Hanan, E. J., Tague, C. (Naomi), & Schimel, J. P. (2017). Nitrogen cycling and export in  
810 California chaparral: the role of climate in shaping ecosystem responses to fire.  
811 *Ecological Monographs*, 87(1), 76–90. <https://doi.org/10.1002/ecm.1234>

812 Hanan, E. J., Tague, C., Choate, J., Liu, M., Kolden, C., & Adam, J. (2018). Accounting for  
813 disturbance history in models: using remote sensing to constrain carbon and nitrogen pool  
814 spin-up. *Ecological Applications: A Publication of the Ecological Society of America*,  
815 28(5), 1197–1214. <https://doi.org/10.1002/eap.1718>

816 Hanan, E. J., Ren, J., Tague, C. L., Kolden, C. A., Abatzoglou, J. T., Bart, R. R., et al. (2021).  
817 How climate change and fire exclusion drive wildfire regimes at actionable scales.

818 *Environmental Research Letters*, 16(2), 024051. <https://doi.org/10.1088/1748->  
819 9326/abd78e

820 Hartigan, J. A., & Wong, M. A. (1979). Algorithm AS 136: A K-Means Clustering Algorithm.  
821 *Journal of the Royal Statistical Society. Series C (Applied Statistics)*, 28(1), 100–108.  
822 <https://doi.org/10.2307/2346830>

823 Homyak, P. M., Sickman, J. O., Miller, A. E., Melack, J. M., Meixner, T., & Schimel, J. P.  
824 (2014). Assessing Nitrogen-Saturation in a Seasonally Dry Chaparral Watershed:  
825 Limitations of Traditional Indicators of N-Saturation. *Ecosystems*, 17(7), 1286–1305.  
826 <https://doi.org/10.1007/s10021-014-9792-2>

827 Homyak, P. M., Blankinship, J. C., Marchus, K., Lucero, D. M., Sickman, J. O., & Schimel, J. P.  
828 (2016). Aridity and plant uptake interact to make dryland soils hotspots for nitric oxide  
829 (NO) emissions. *Proceedings of the National Academy of Sciences*, 113(19), E2608–  
830 E2616. <https://doi.org/10.1073/pnas.1520496113>

831 Krichels, A. H., Greene, A. C., Jenerette, G. D., Spasojevic, M. J., Glassman, S. I., & Homyak,  
832 P. M. (2022). Precipitation legacies amplify ecosystem nitrogen losses from nitric oxide  
833 emissions in a Pinyon–Juniper dryland. *Ecology*, n/a(n/a), e3930.  
834 <https://doi.org/10.1002/ecy.3930>

835 Laudon, H., Berggren, M., Ågren, A., Buffam, I., Bishop, K., Grabs, T., et al. (2011). Patterns  
836 and Dynamics of Dissolved Organic Carbon (DOC) in Boreal Streams: The Role of  
837 Processes, Connectivity, and Scaling. *Ecosystems*, 14(6), 880–893.  
838 <https://doi.org/10.1007/s10021-011-9452-8>

839 Li, X., Meixner, T., Sickman, J. O., Miller, A. E., Schimel, J. P., & Melack, J. M. (2006).  
840 Decadal-scale Dynamics of Water, Carbon and Nitrogen in a California Chaparral

841 Ecosystem: DAYCENT Modeling Results. *Biogeochemistry*, 77(2), 217–245.  
842 <https://doi.org/10.1007/s10533-005-1391-z>

843 Liao, K.-H., Lv, L.-G., Yang, G.-S., & Zhu, Q. (2016). Sensitivity of simulated hillslope  
844 subsurface flow to rainfall patterns, soil texture and land use. *Soil Use and Management*,  
845 32(3), 422–432. <https://doi.org/10.1111/sum.12282>

846 Lin, L., Webster, J. R., Hwang, T., & Band, L. E. (2015). Effects of lateral nitrate flux and  
847 instream processes on dissolved inorganic nitrogen export in a forested catchment: A  
848 model sensitivity analysis. *Water Resources Research*, 51(4), 2680–2695.  
849 <https://doi.org/10.1002/2014WR015962>

850 Malek, K., Stöckle, C., Chinnayakanahalli, K., Nelson, R., Liu, M., Rajagopalan, K., et al.  
851 (2017). VIC–CropSyst-v2: A regional-scale modeling platform to simulate the nexus of  
852 climate, hydrology, cropping systems, and human decisions. *Geoscientific Model*  
853 *Development*, 10(8), 3059–3084. <https://doi.org/10.5194/gmd-10-3059-2017>

854 Maxwell, A. E., Warner, T. A., Vanderbilt, B. C., & Ramezan, C. A. (2017). Land Cover  
855 Classification and Feature Extraction from National Agriculture Imagery Program  
856 (NAIP) Orthoimagery: A Review. *Photogrammetric Engineering & Remote Sensing*,  
857 83(11), 737–747. <https://doi.org/10.14358/PERS.83.10.737>

858 McClain, M. E., Boyer, E. W., Dent, C. L., Gergel, S. E., Grimm, N. B., Groffman, P. M., et al.  
859 (2003). Biogeochemical Hot Spots and Hot Moments at the Interface of Terrestrial and  
860 Aquatic Ecosystems. *Ecosystems*, 6(4), 301–312. [https://doi.org/10.1007/s10021-003-](https://doi.org/10.1007/s10021-003-0161-9)  
861 0161-9

862 Meentemeyer, R. K., & Moody, A. (2002). Distribution of plant life history types in California  
863 chaparral: the role of topographically-determined drought severity. *Journal of Vegetation*  
864 *Science*, 13(1), 67–78. <https://doi.org/10.1111/j.1654-1103.2002.tb02024.x>

865 Meixner, T., Fenn, M. E., Wohlgemuth, P., Oxford, M., & Riggan, P. (2006). N Saturation  
866 Symptoms in Chaparral Catchments Are Not Reversed by Prescribed Fire. *Environmental*  
867 *Science & Technology*, 40(9), 2887–2894. <https://doi.org/10.1021/es051268z>

868 Nash, J. E., & Sutcliffe, J. V. (1970). River flow forecasting through conceptual models part I —  
869 A discussion of principles. *Journal of Hydrology*, 10(3), 282–290.  
870 [https://doi.org/10.1016/0022-1694\(70\)90255-6](https://doi.org/10.1016/0022-1694(70)90255-6)

871 Osborne, B. B., Nasto, M. K., Soper, F. M., Asner, G. P., Balzotti, C. S., Cleveland, C. C., et al.  
872 (2020). Leaf litter inputs reinforce islands of nitrogen fertility in a lowland tropical forest.  
873 *Biogeochemistry*, 147(3), 293–306. <https://doi.org/10.1007/s10533-020-00643-0>

874 Ouyang, W., Xu, X., Hao, Z., & Gao, X. (2017). Effects of soil moisture content on upland  
875 nitrogen loss. *Journal of Hydrology*, 546, 71–80.  
876 <https://doi.org/10.1016/j.jhydrol.2016.12.053>

877 Parker, S. S., & Schimel, J. P. (2011). Soil nitrogen availability and transformations differ  
878 between the summer and the growing season in a California grassland. *Applied Soil*  
879 *Ecology*, 48(2), 185–192. <https://doi.org/10.1016/j.apsoil.2011.03.007>

880 Parton, W. J. (1996). The CENTURY model. In D. S. Powlson, P. Smith, & J. U. Smith (Eds.),  
881 *Evaluation of Soil Organic Matter Models* (Vol. 38, pp. 283–291). Springer, Berlin,  
882 Heidelberg: Evaluation of Soil Organic Matter Models.

883 Phillip, J. (1957). The theory of infiltration: 4. Sorptivity and algebraic infiltration equation. *Soil*  
884 *Sci*, 84, 257–264.

885 Pinay, G., Peiffer, S., De Dreuzy, J.-R., Krause, S., Hannah, D. M., Fleckenstein, J. H., et al.  
886 (2015). Upscaling Nitrogen Removal Capacity from Local Hotspots to Low Stream  
887 Orders' Drainage Basins. *Ecosystems*, *18*(6), 1101–1120. [https://doi.org/10.1007/s10021-](https://doi.org/10.1007/s10021-015-9878-5)  
888 [015-9878-5](https://doi.org/10.1007/s10021-015-9878-5)

889 Poblador, S., Lupon, A., Sabaté, S., & Sabater, F. (2017). Soil water content drives  
890 spatiotemporal patterns of CO<sub>2</sub> and N<sub>2</sub>O emissions from a Mediterranean riparian forest  
891 soil. *Biogeosciences*, *14*(18), 4195–4208. <https://doi.org/10.5194/bg-14-4195-2017>

892 R Core Team. (2022). R: A Language and Environment for Statistical Computing. Retrieved  
893 from <https://www.R-project.org/>

894 Ren, J., Adam, J. C., Hicke, J. A., Hanan, E. J., Tague, C. L., Liu, M., et al. (2021). How does  
895 water yield respond to mountain pine beetle infestation in a semiarid forest? *Hydrology*  
896 *and Earth System Sciences*, *25*(9), 4681–4699. [https://doi.org/10.5194/hess-25-4681-](https://doi.org/10.5194/hess-25-4681-2021)  
897 [2021](https://doi.org/10.5194/hess-25-4681-2021)

898 Ren, J., Hanan, E., Hicke, J., Kolden, C., Abatzoglou, J. T., Tague, C., et al. (2022, March 23).  
899 Bark beetle effects on fire regimes depend on underlying fuel modifications in semiarid  
900 systems [preprint]. <https://doi.org/10.1002/essoar.10510802.1>

901 Ridolfi, L., Laio, F., & D'Odorico, P. (2008). Fertility Island Formation and Evolution in  
902 Dryland Ecosystems. *Ecology and Society*, *13*(1). [https://doi.org/10.5751/ES-02302-](https://doi.org/10.5751/ES-02302-130105)  
903 [130105](https://doi.org/10.5751/ES-02302-130105)

904 Schimel, J. P. (2018). Life in Dry Soils: Effects of Drought on Soil Microbial Communities and  
905 Processes. *Annual Review of Ecology, Evolution, and Systematics*, *49*(1), 409–432.  
906 <https://doi.org/10.1146/annurev-ecolsys-110617-062614>

907 Schmidt, J. P., Hong, N., Dellinger, A., Beegle, D. B., & Lin, H. (2007). Hillslope Variability in  
908 Corn Response to Nitrogen Linked to In-Season Soil Moisture Redistribution. *Agronomy*  
909 *Journal*, 99(1), 229–237. <https://doi.org/10.2134/agronj2006.0187>

910 Seager, R., Lis, N., Feldman, J., Ting, M., Williams, A. P., Nakamura, J., et al. (2018). Whither  
911 the 100th Meridian? The Once and Future Physical and Human Geography of America’s  
912 Arid–Humid Divide. Part I: The Story So Far. *Earth Interactions*, 22(5), 1–22.  
913 <https://doi.org/10.1175/EI-D-17-0011.1>

914 Smith, F. W., Sampson, D. A., & Long, J. N. (1991). Comparison of Leaf Area Index Estimates  
915 from Tree Allometrics and Measured Light Interception. *Forest Science*, 37(6), 1682–  
916 1688. <https://doi.org/10.1093/forestscience/37.6.1682>

917 Soil Survey Staff. (2022). *Keys to Soil Taxonomy*, 13th ed. USDA-Natural Resources.

918 Tague, C. (2009). Modeling hydrologic controls on denitrification: sensitivity to parameter  
919 uncertainty and landscape representation. *Biogeochemistry*, 93(1/2,), 79–90.

920 Tague, C. L., & Band, L. E. (2004). RHESSys: Regional Hydro-Ecologic Simulation System—  
921 An Object-Oriented Approach to Spatially Distributed Modeling of Carbon, Water, and  
922 Nutrient Cycling. *Earth Interactions*, 8(19), 1–42. [https://doi.org/10.1175/1087-3562\(2004\)8<1:RRHSSO>2.0.CO;2](https://doi.org/10.1175/1087-3562(2004)8<1:RRHSSO>2.0.CO;2)

923

924 Vargas, R., Sonnentag, O., Abramowitz, G., Carrara, A., Chen, J. M., Ciais, P., et al. (2013).  
925 Drought Influences the Accuracy of Simulated Ecosystem Fluxes: A Model-Data Meta-  
926 analysis for Mediterranean Oak Woodlands. *Ecosystems*, 16(5), 749–764.  
927 <https://doi.org/10.1007/s10021-013-9648-1>

928 Walter, M. T., Walter, M. F., Brooks, E. S., Steenhuis, T. S., Boll, J., & Weiler, K. (2000).  
929 Hydrologically sensitive areas: Variable source area hydrology implications for water  
930 quality risk assessment. *Journal of Soil and Water Conservation*, 55(3), 277–284.

931 White, M. A., Thornton, P. E., Running, S. W., & Nemani, R. R. (2000). Parameterization and  
932 Sensitivity Analysis of the BIOME–BGC Terrestrial Ecosystem Model: Net Primary  
933 Production Controls. *Earth Interactions*, 4(3), 1–85. [https://doi.org/10.1175/1087-  
934 3562\(2000\)004<0003:PASAOT>2.0.CO;2](https://doi.org/10.1175/1087-3562(2000)004<0003:PASAOT>2.0.CO;2)

935 Wohlgemuth, P. (2006). *Hillslope erosion and small watershed sediment yield following a  
936 wildfire on the San Dimas Experimental Forest, southern California*. Reno, Nevada.:  
937 Proceedings of the 8th Federal Interagency Sedimentation Conference. Retrieved from  
938 [https://www.semanticscholar.org/paper/HILLSLOPE-EROSION-AND-SMALL-  
939 WATERSHED-SEDIMENT-A-ON-  
940 Wohlgemuth/e666a9991c2c1813f3e63289a20636d4028fb7ec](https://www.semanticscholar.org/paper/HILLSLOPE-EROSION-AND-SMALL-WATERSHED-SEDIMENT-A-ON-Wohlgemuth/e666a9991c2c1813f3e63289a20636d4028fb7ec)

941 Wood, E. F., Lettenmaier, D. P., & Zartarian, V. G. (1992). A land-surface hydrology  
942 parameterization with subgrid variability for general circulation models. *Journal of  
943 Geophysical Research: Atmospheres*, 97(D3), 2717–2728.  
944 <https://doi.org/10.1029/91JD01786>

945 Wood, E. F., Roundy, J. K., Troy, T. J., van Beek, L. P. H., Bierkens, M. F. P., Blyth, E., et al.  
946 (2011). Hyperresolution global land surface modeling: Meeting a grand challenge for  
947 monitoring Earth’s terrestrial water. *Water Resources Research*, 47(5).  
948 <https://doi.org/10.1029/2010WR010090>

949 Zarnetske, J. P., Haggerty, R., Wondzell, S. M., & Baker, M. A. (2011). Dynamics of nitrate  
950 production and removal as a function of residence time in the hyporheic zone. *Journal of*  
951 *Geophysical Research: Biogeosciences*, 116(G1). <https://doi.org/10.1029/2010JG001356>

952 Zhang, J., Cai, Z., & Müller, C. (2018). Terrestrial N cycling associated with climate and plant-  
953 specific N preferences: a review. *European Journal of Soil Science*, 69(3), 488–501.  
954 <https://doi.org/10.1111/ejss.12533>

955 Zhu, Q., Schmidt, J. P., & Bryant, R. B. (2012). Hot moments and hot spots of nutrient losses  
956 from a mixed land use watershed. *Journal of Hydrology*, 414–415, 393–404.  
957 <https://doi.org/10.1016/j.jhydrol.2011.11.011>

958 Zhu, Q., Schmidt, J. P., & Bryant, R. B. (2015). Maize (*Zea mays* L.) yield response to nitrogen  
959 as influenced by spatio-temporal variations of soil–water–topography dynamics. *Soil and*  
960 *Tillage Research*, 146, 174–183. <https://doi.org/10.1016/j.still.2014.10.006>

961 Zhu, Q., Castellano, M. J., & Yang, G. (2018). Coupling soil water processes and the nitrogen  
962 cycle across spatial scales: Potentials, bottlenecks and solutions. *Earth-Science Reviews*,  
963 187, 248–258. <https://doi.org/10.1016/j.earscirev.2018.10.005>

964

965

Figure 1.

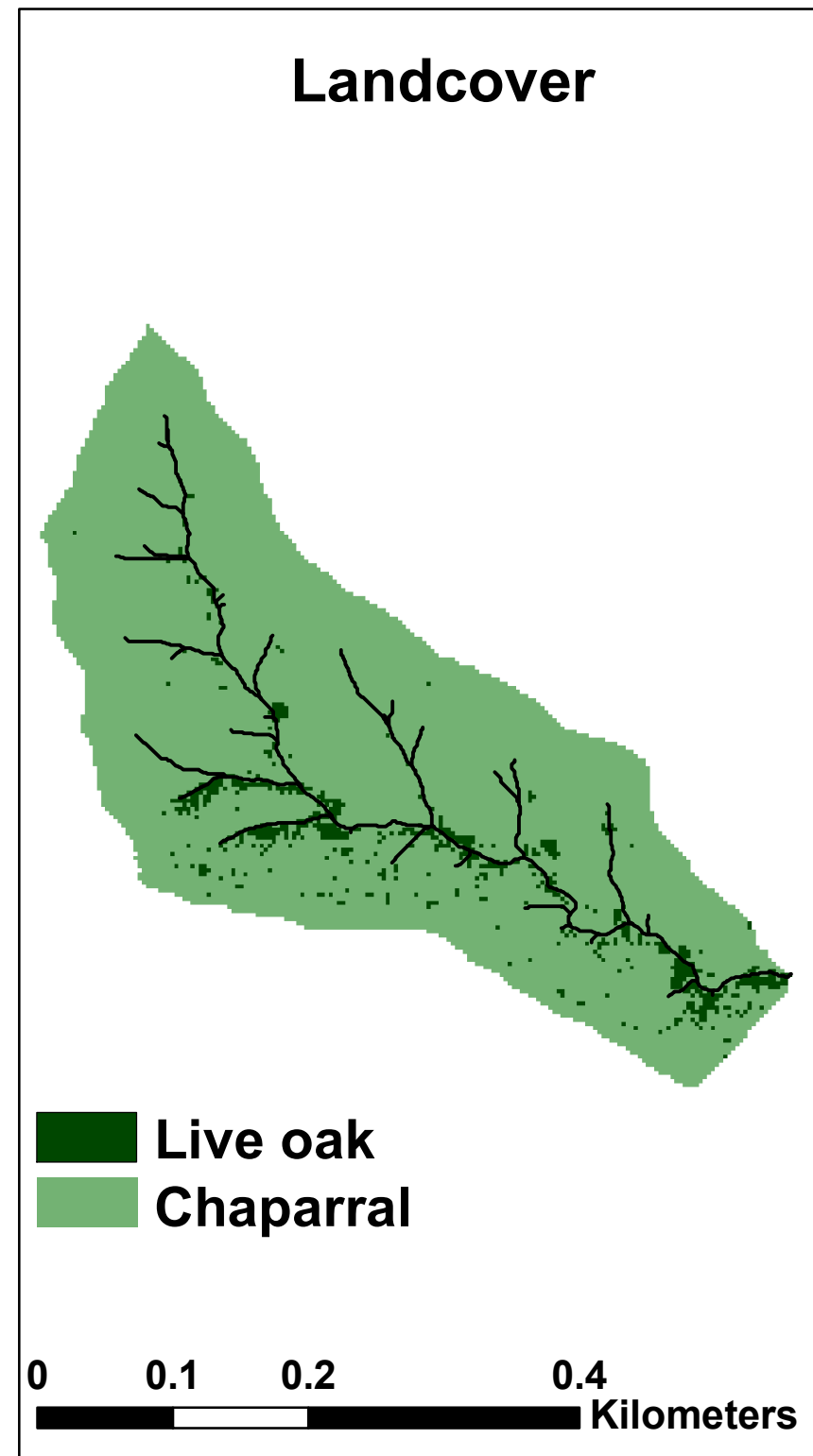
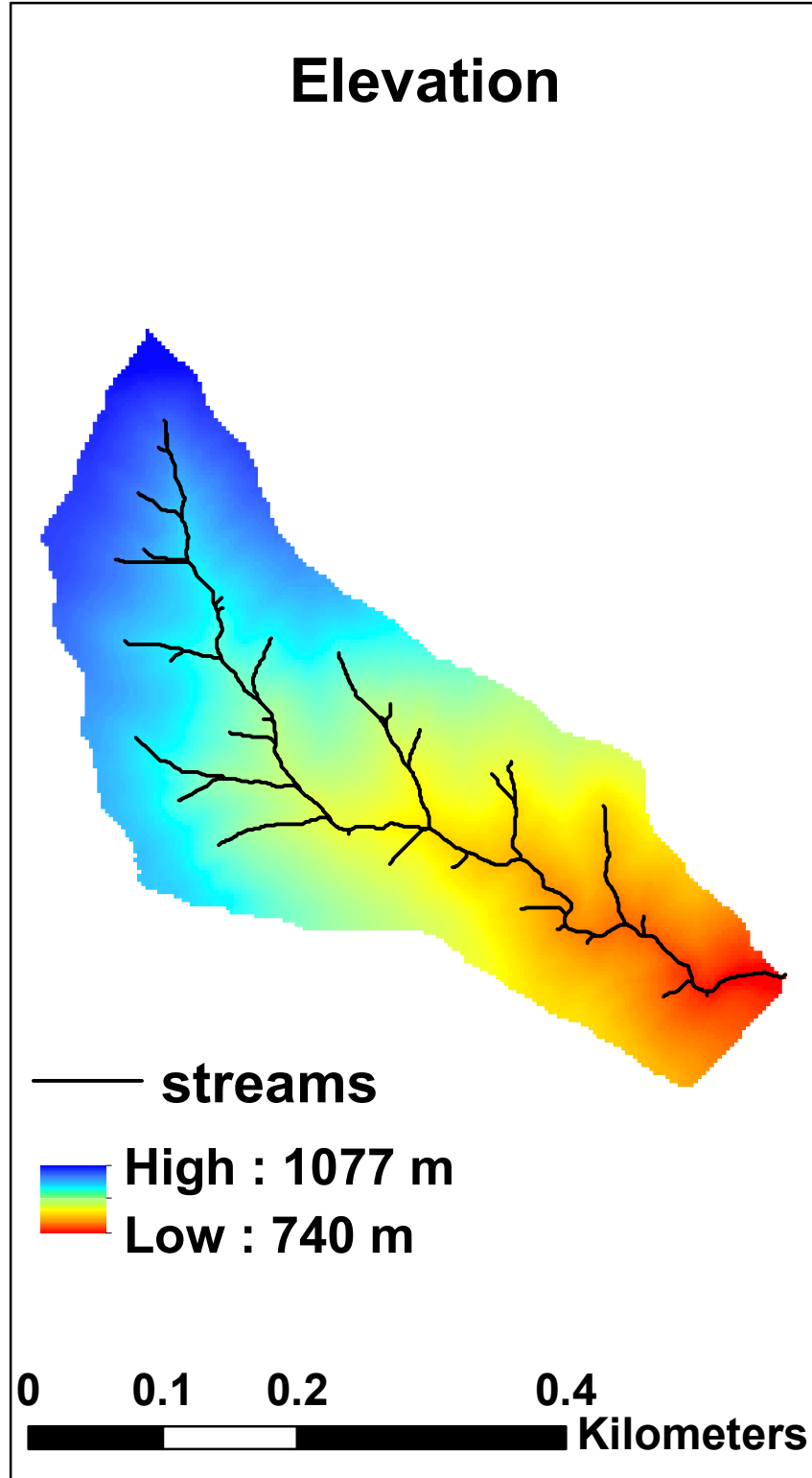


Figure 2.

**Non-hotspot patch**  
(cover fraction:  $1 - m\%$ )

**Hotspot**  
(cover fraction:  $m\%$ )

**(a):** hotspot cover fraction  $m\%$   
can vary by location



Litter fall

N uptake

Litter sharing

Water &  
Nitrogen

Local routing

**(b):**  $sl_l$  and  $sh_g$

Topographic routing

**(c):**  $\theta > \theta_{th}$

Topographic routing

**Downslope patch family**

**Patch family**

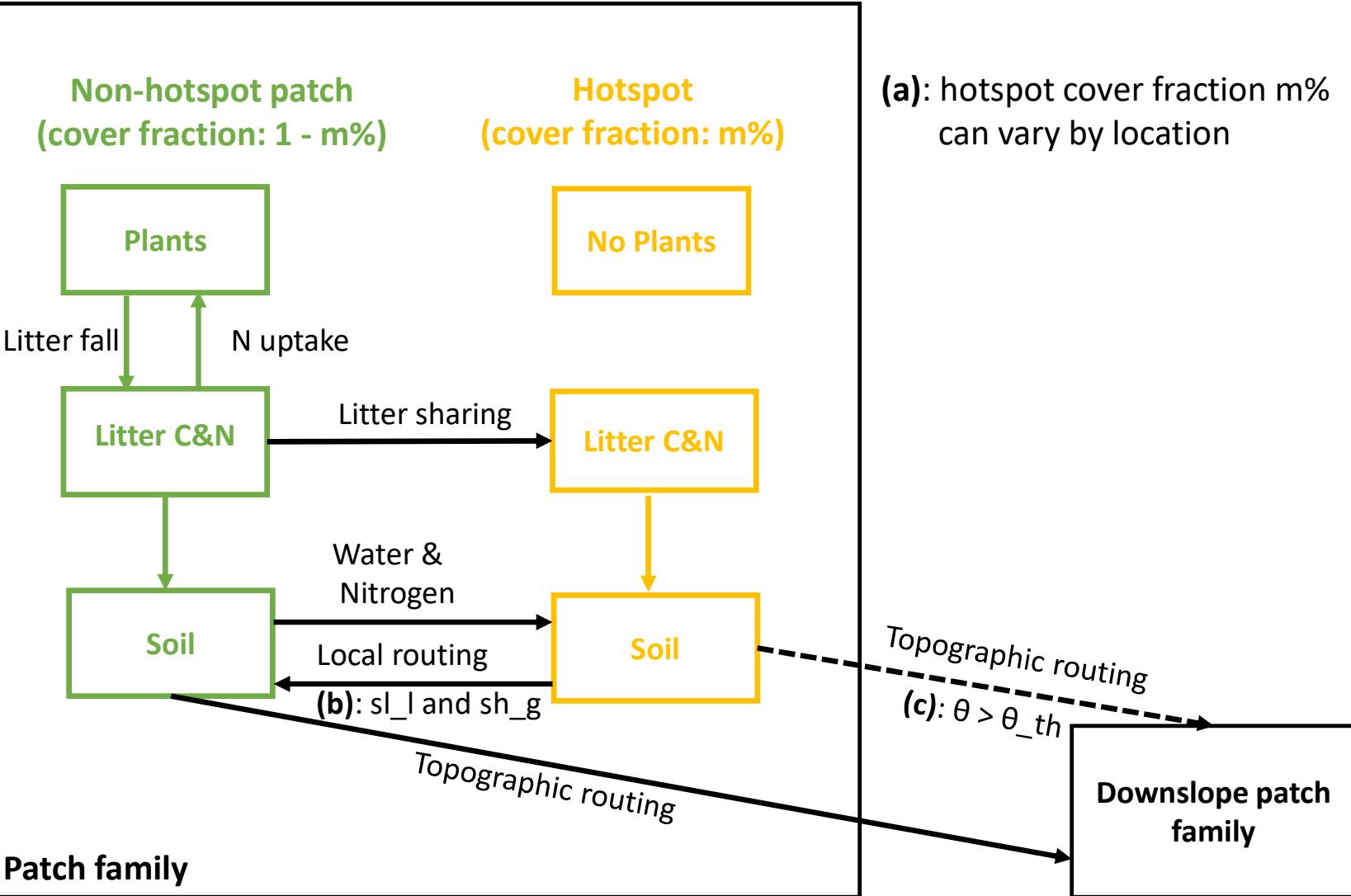
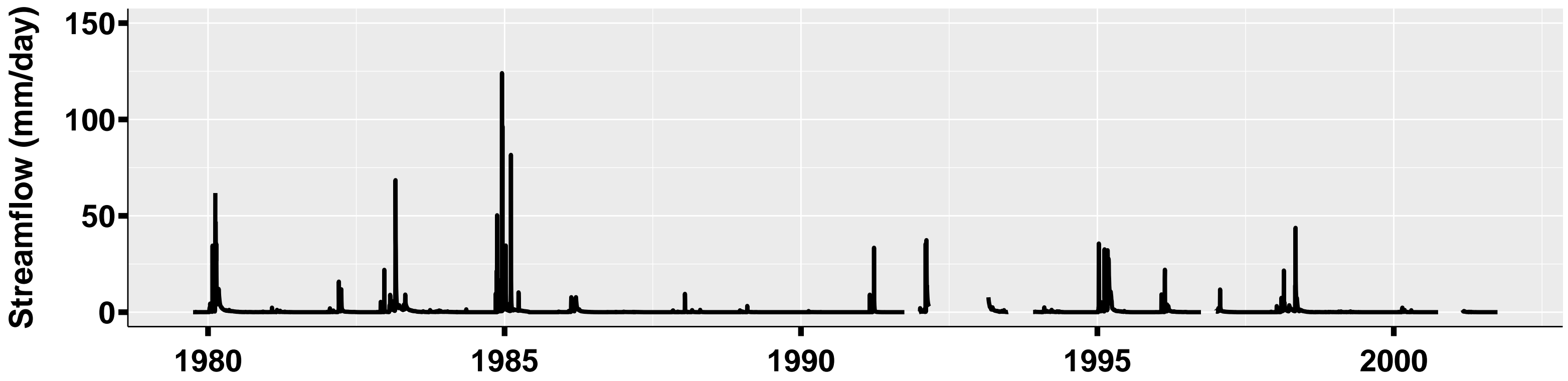


Figure 3.

(a)

# Bell4



(b)

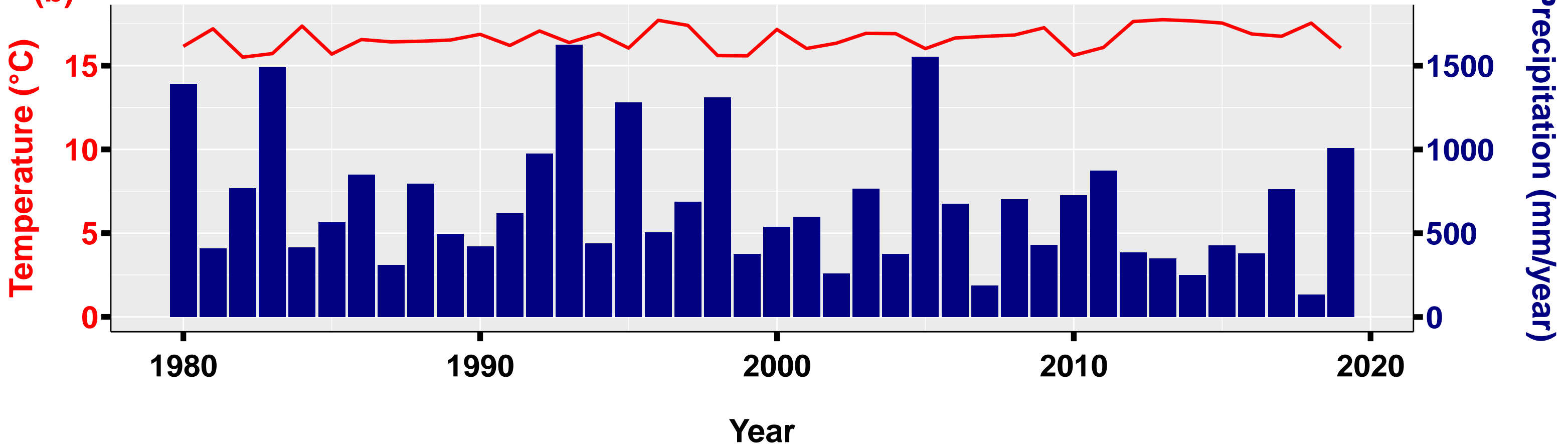


Figure 4.

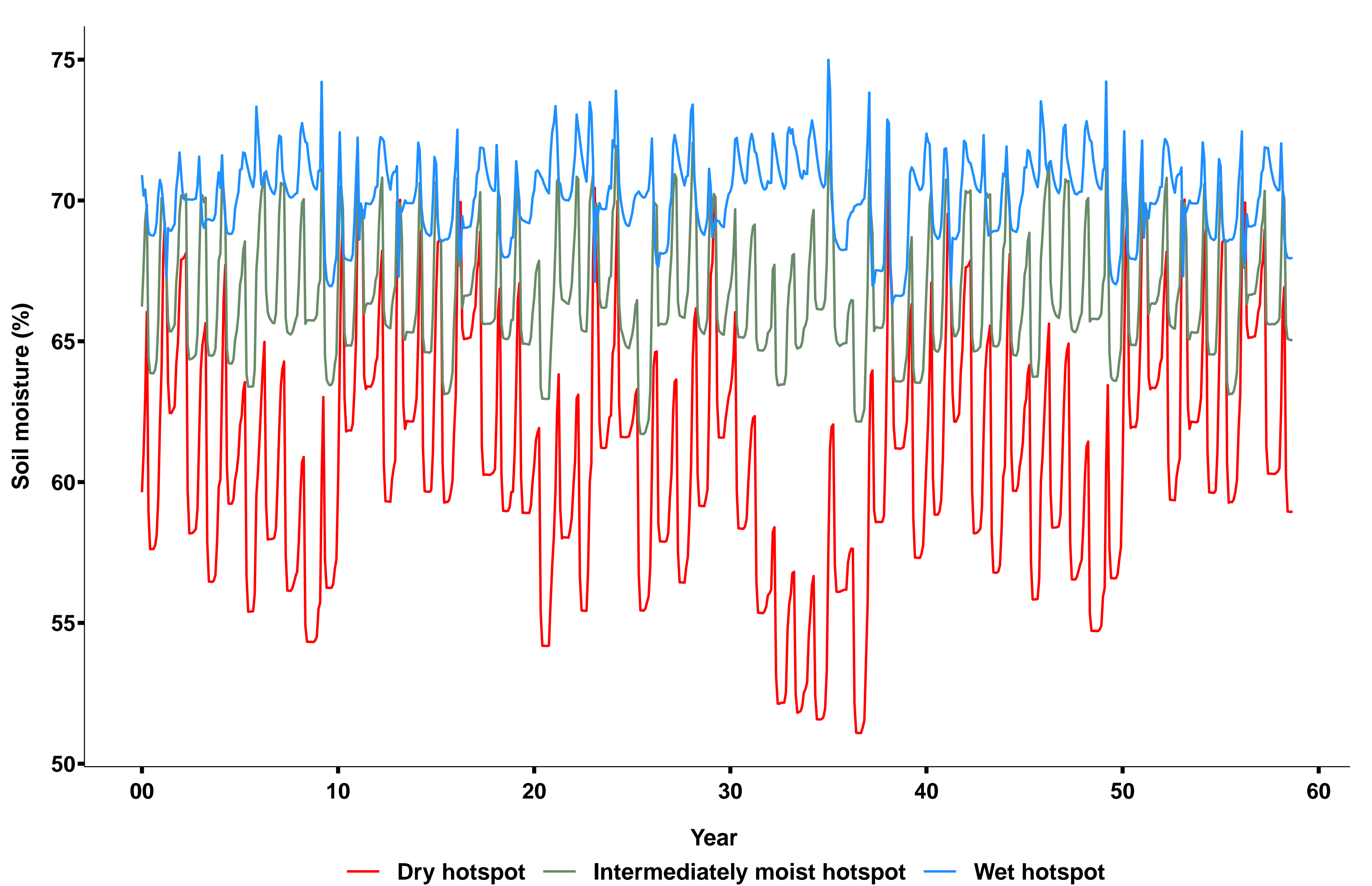


Figure 5.

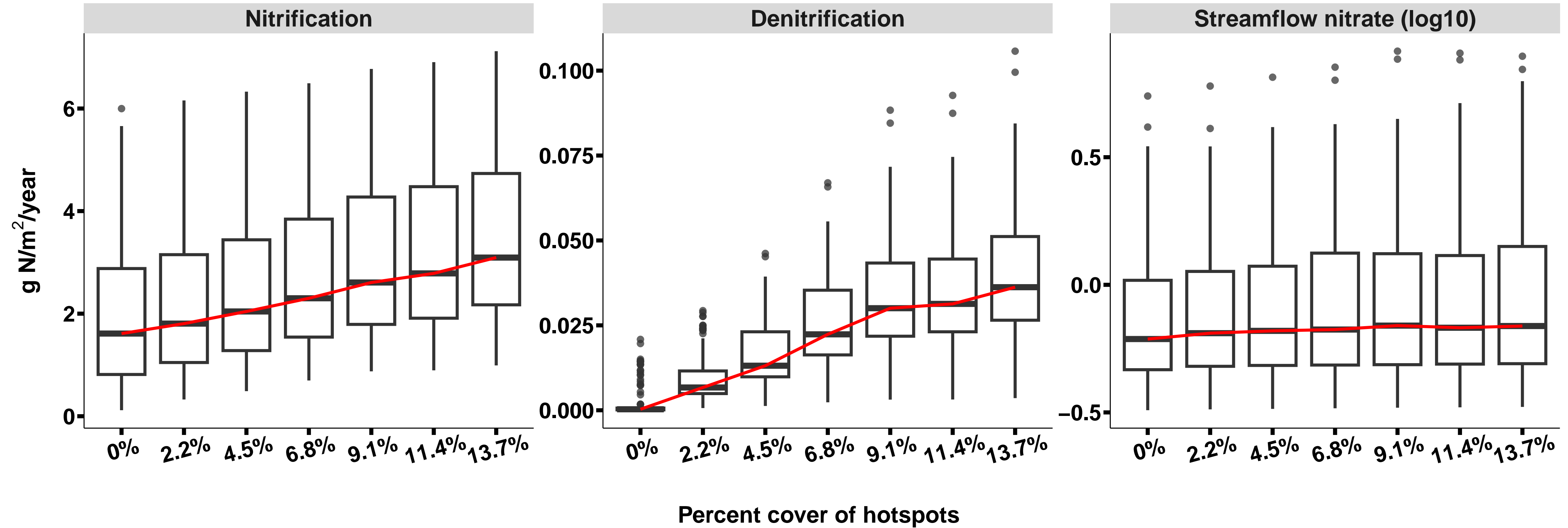


Figure 6.

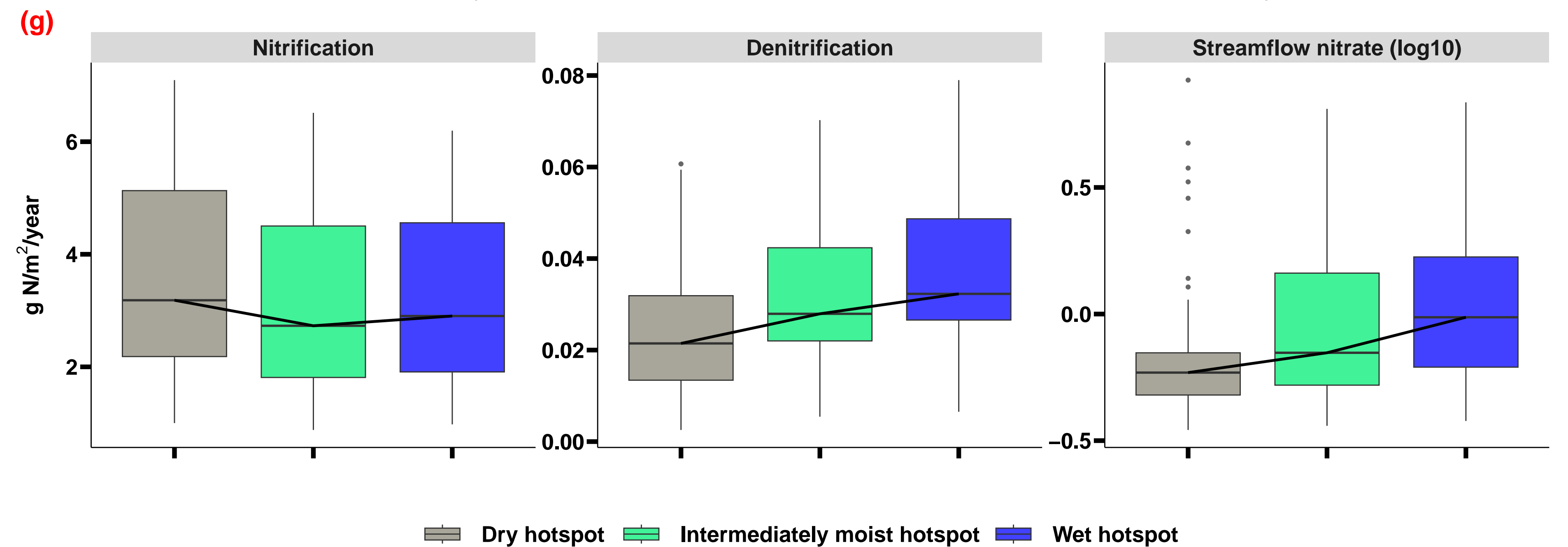
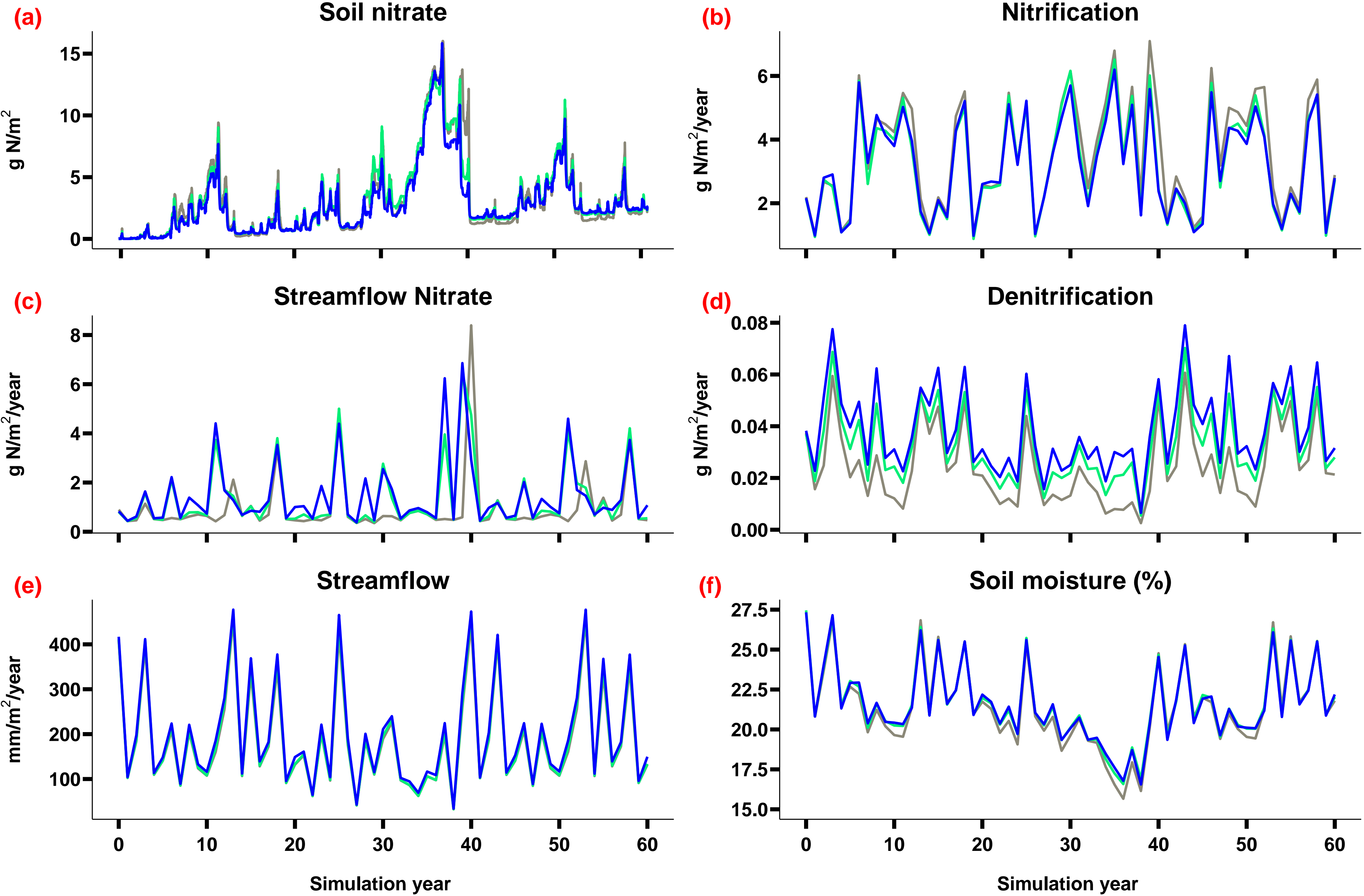


Figure 7.

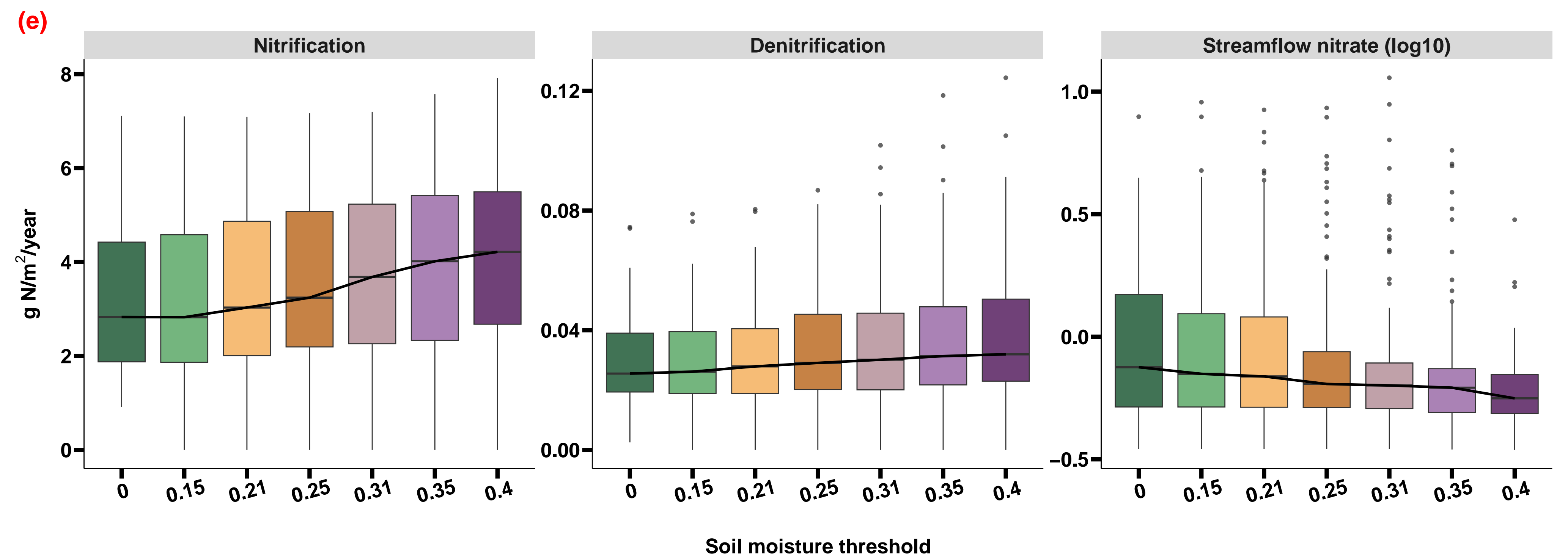
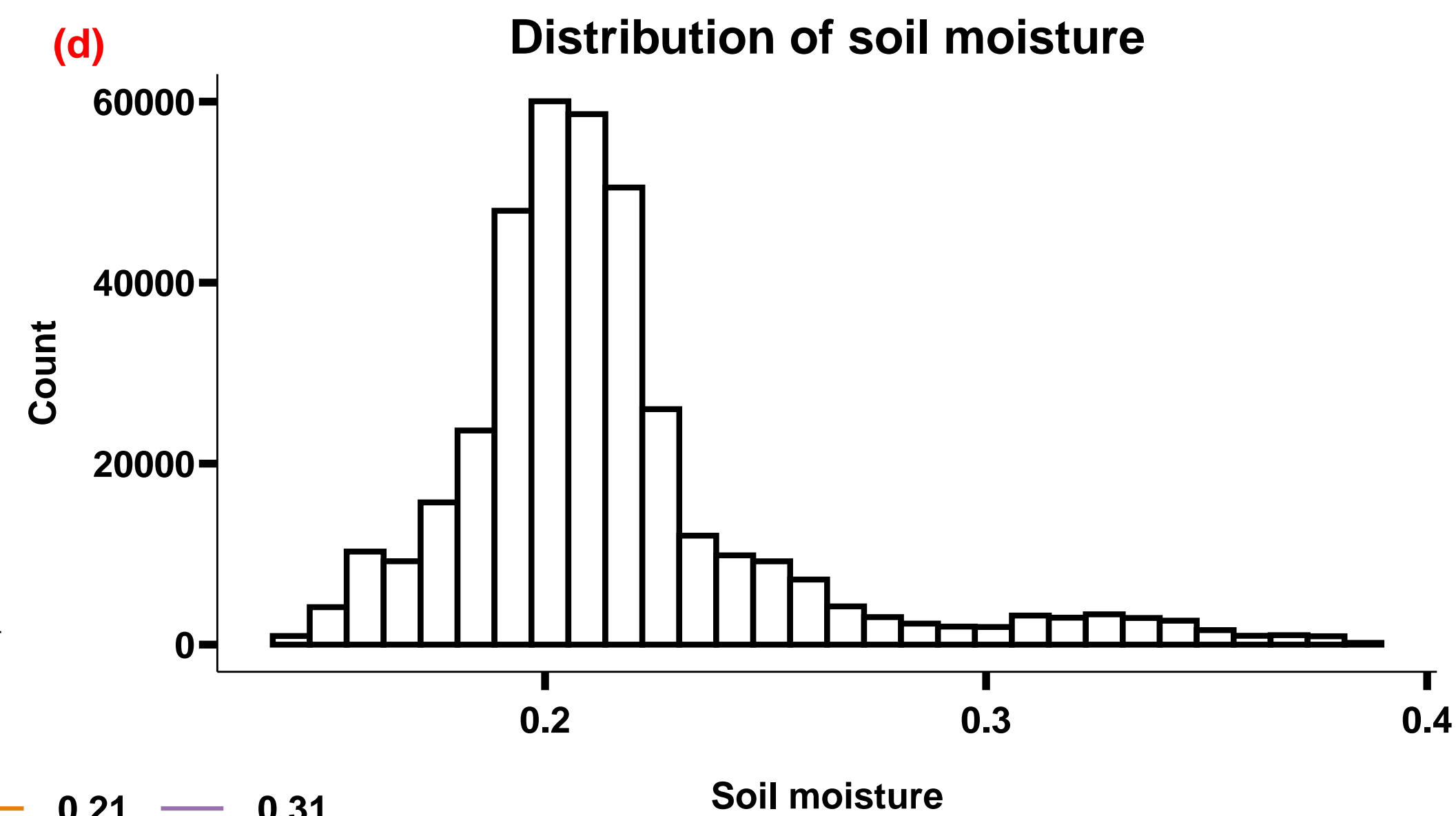
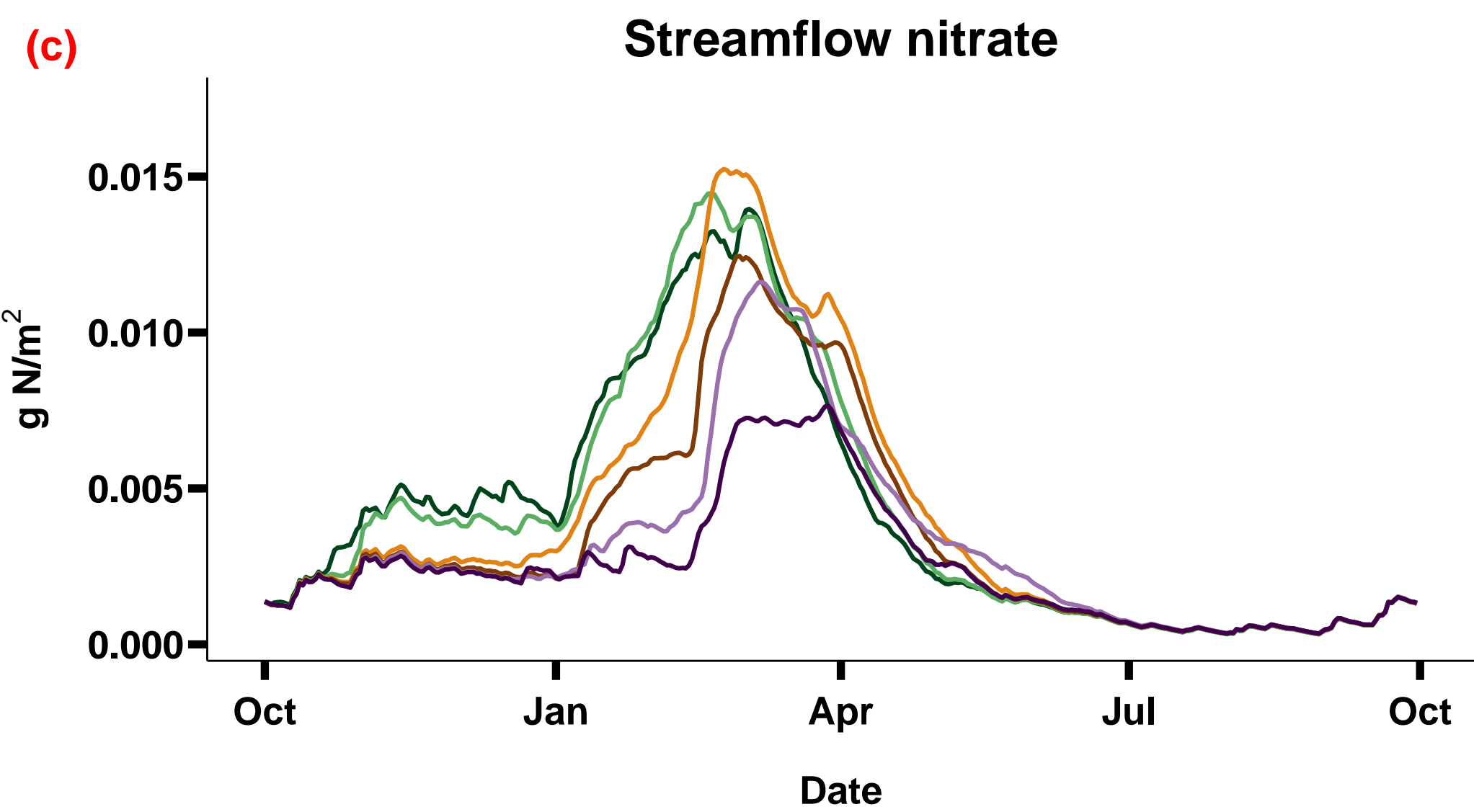
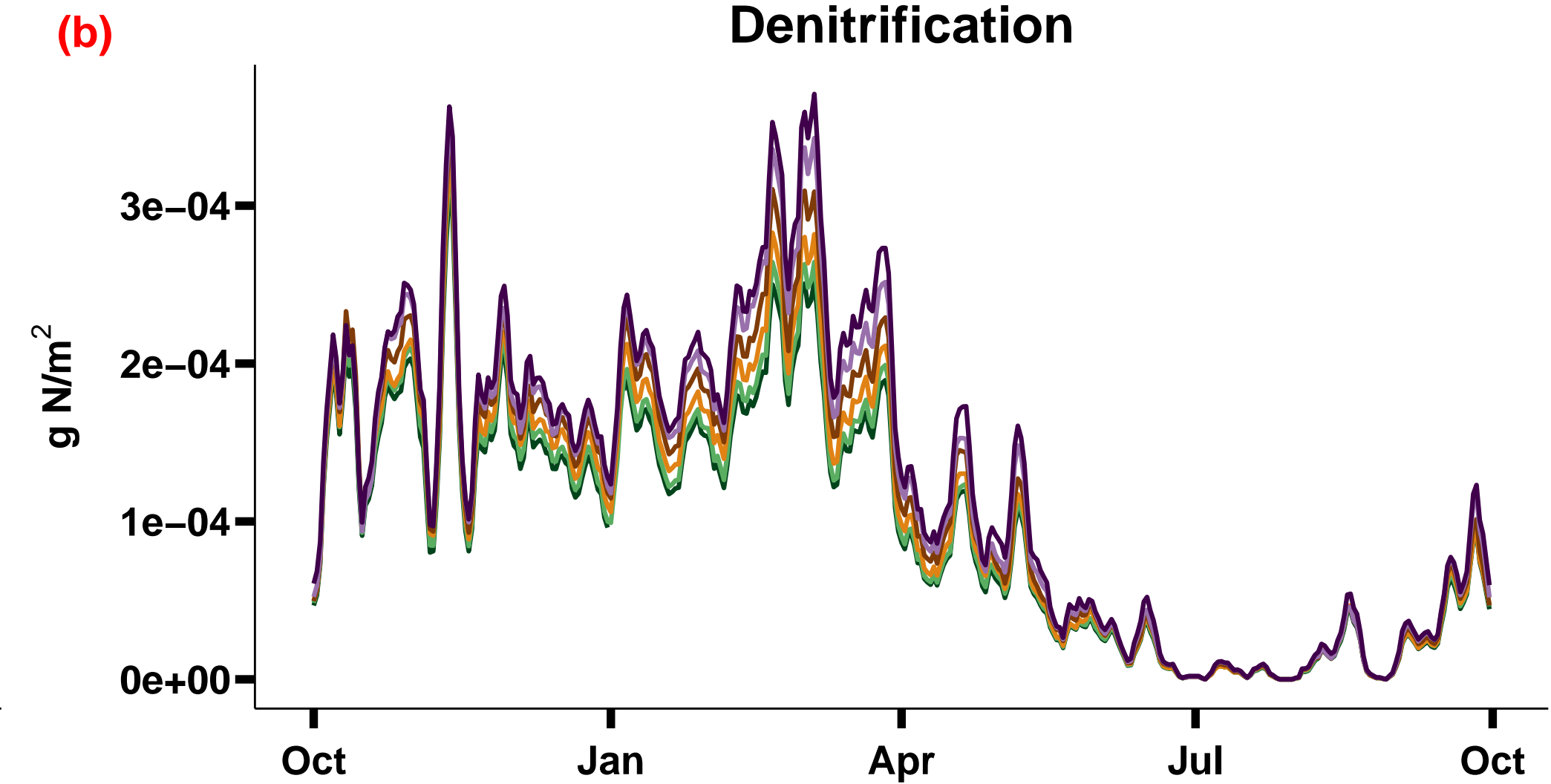
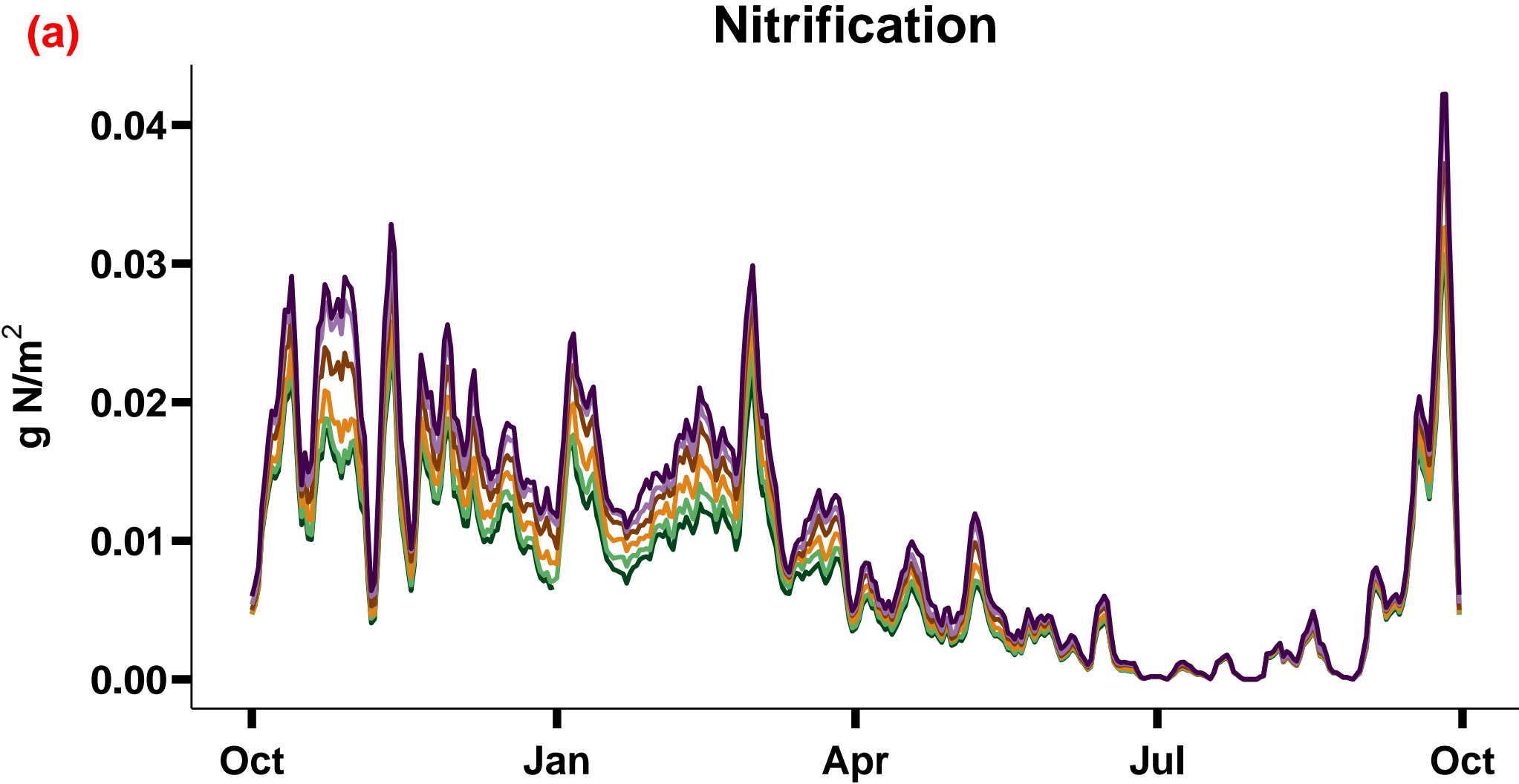


Figure 8.

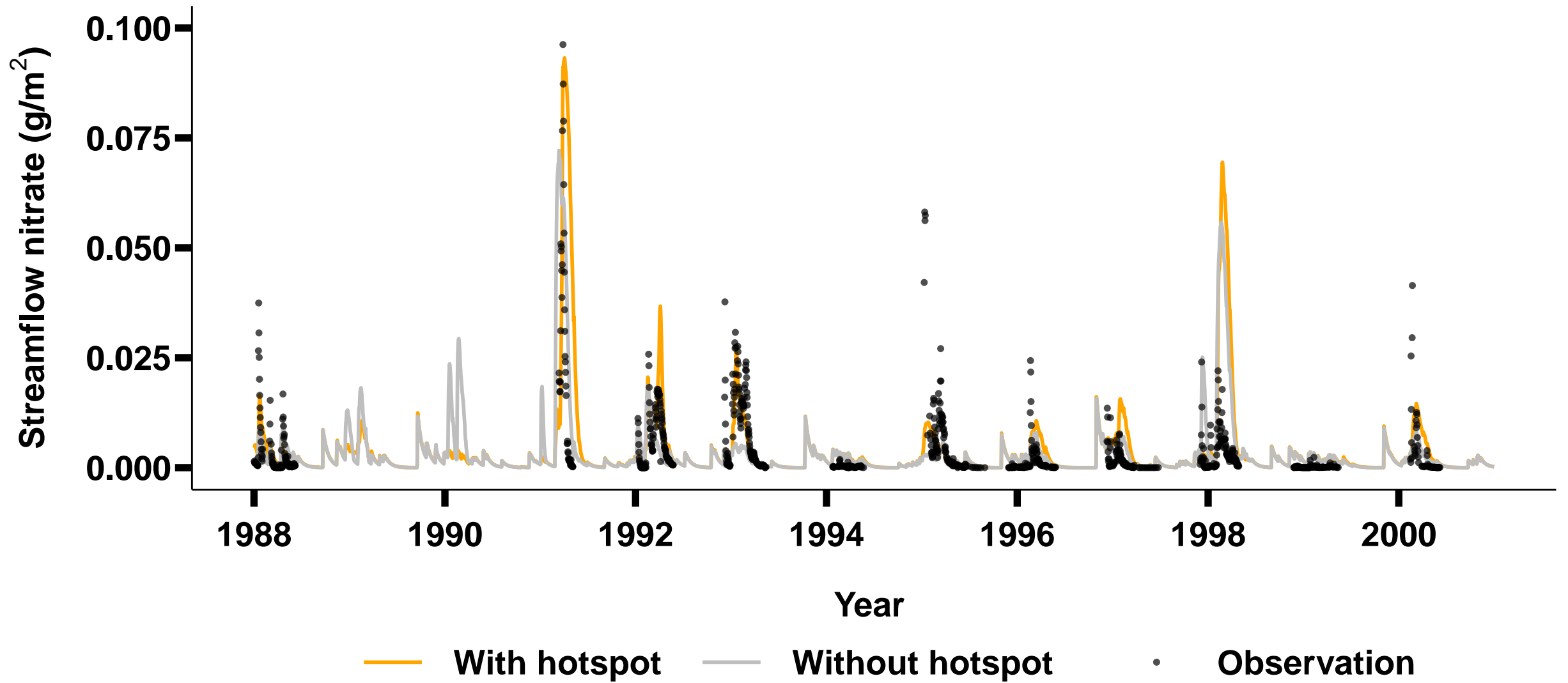
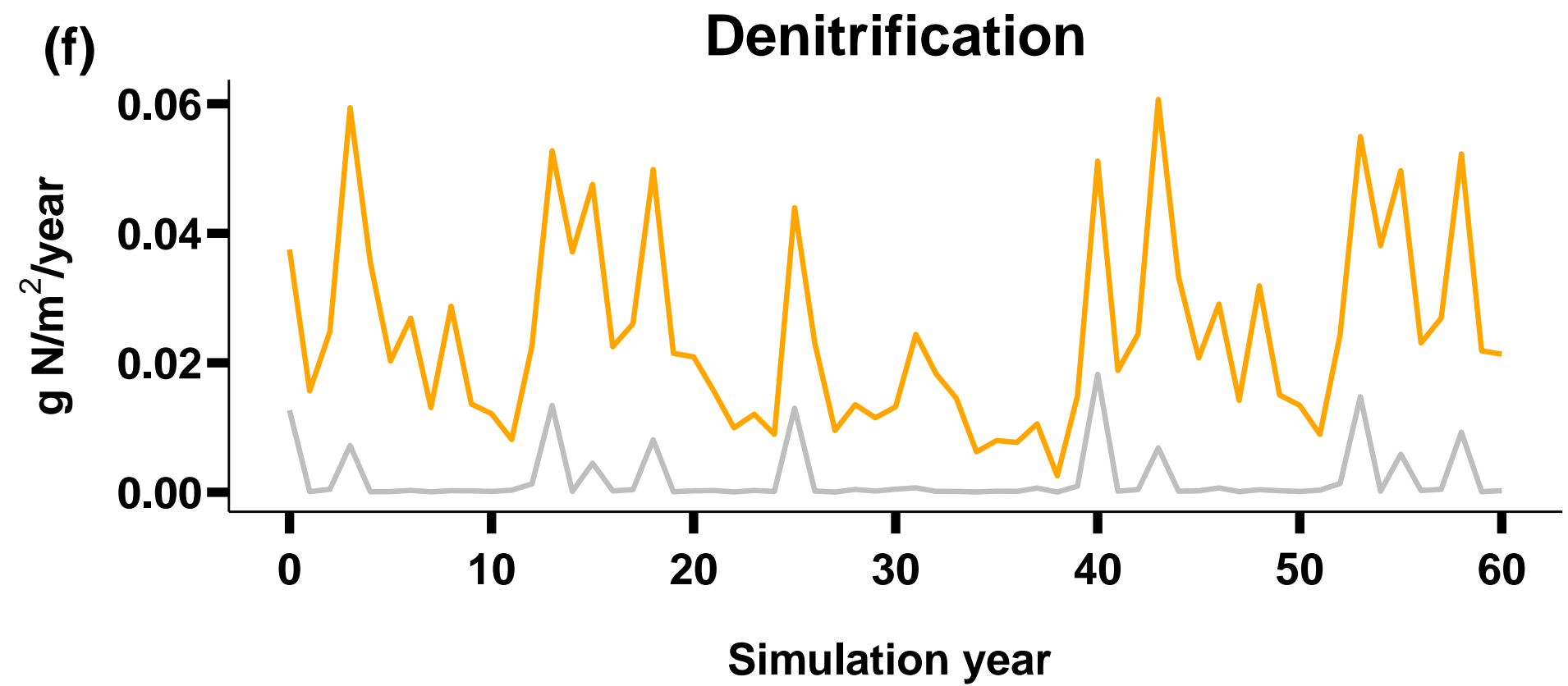
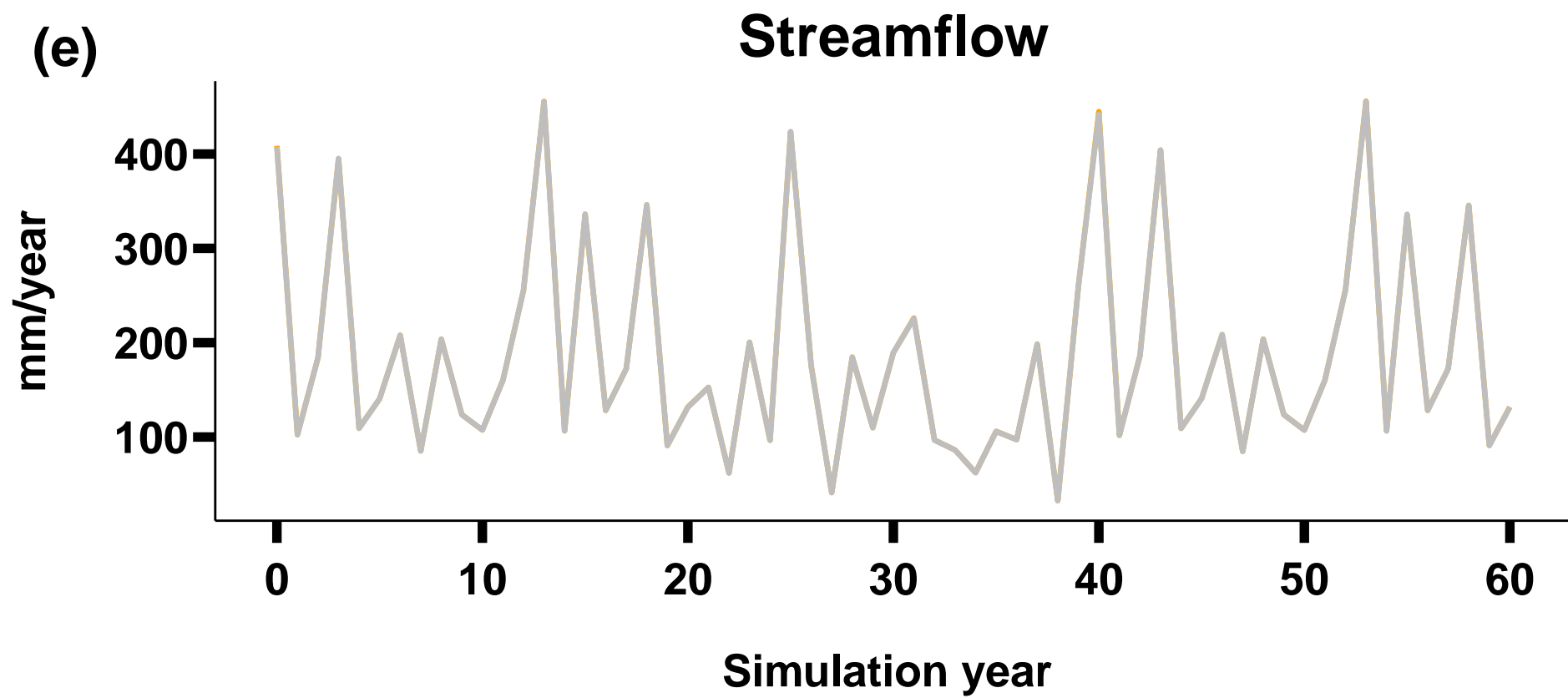
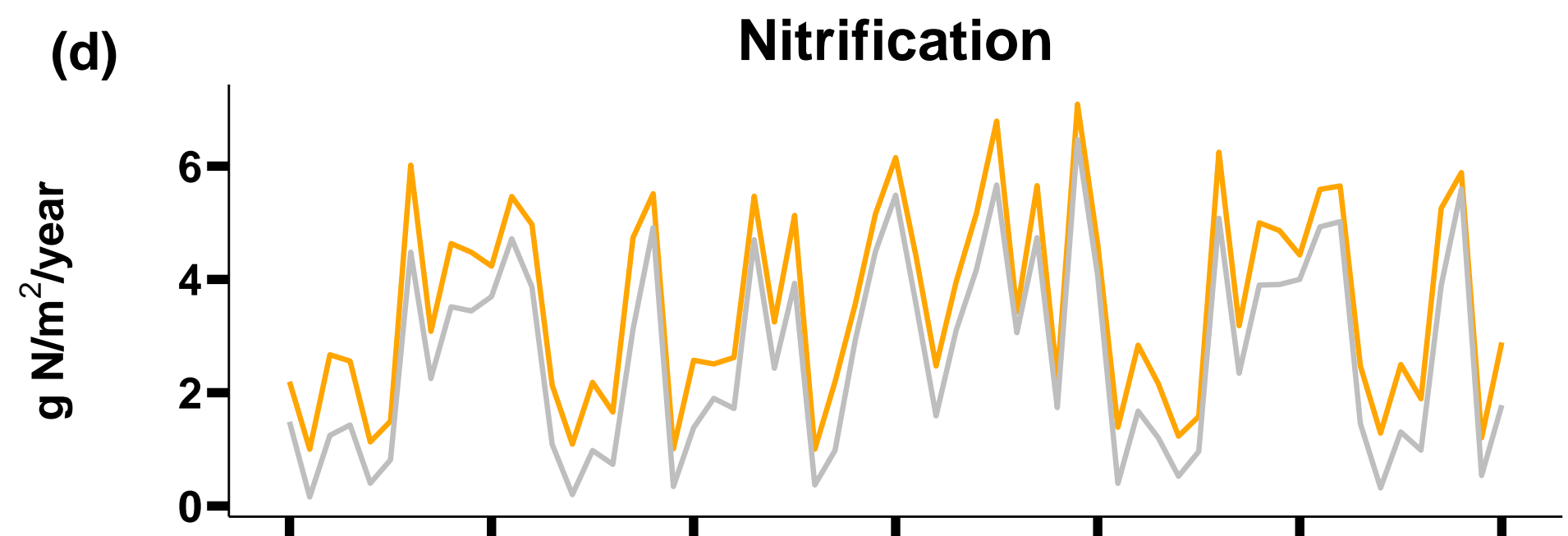
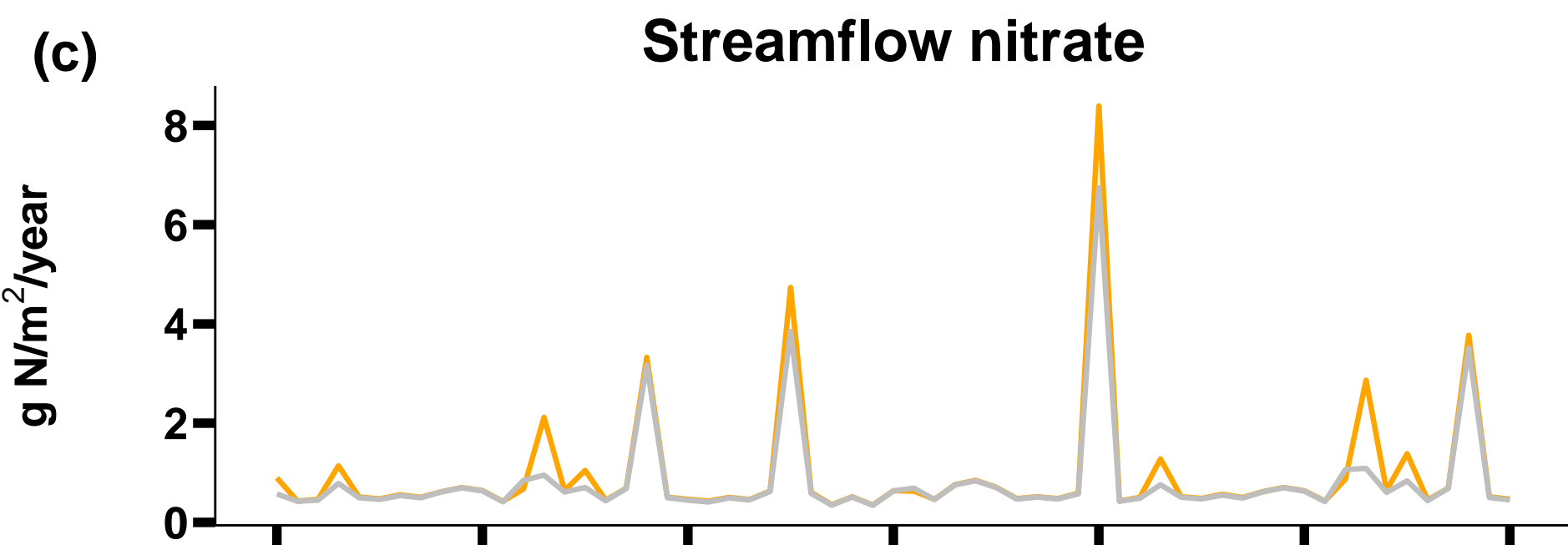
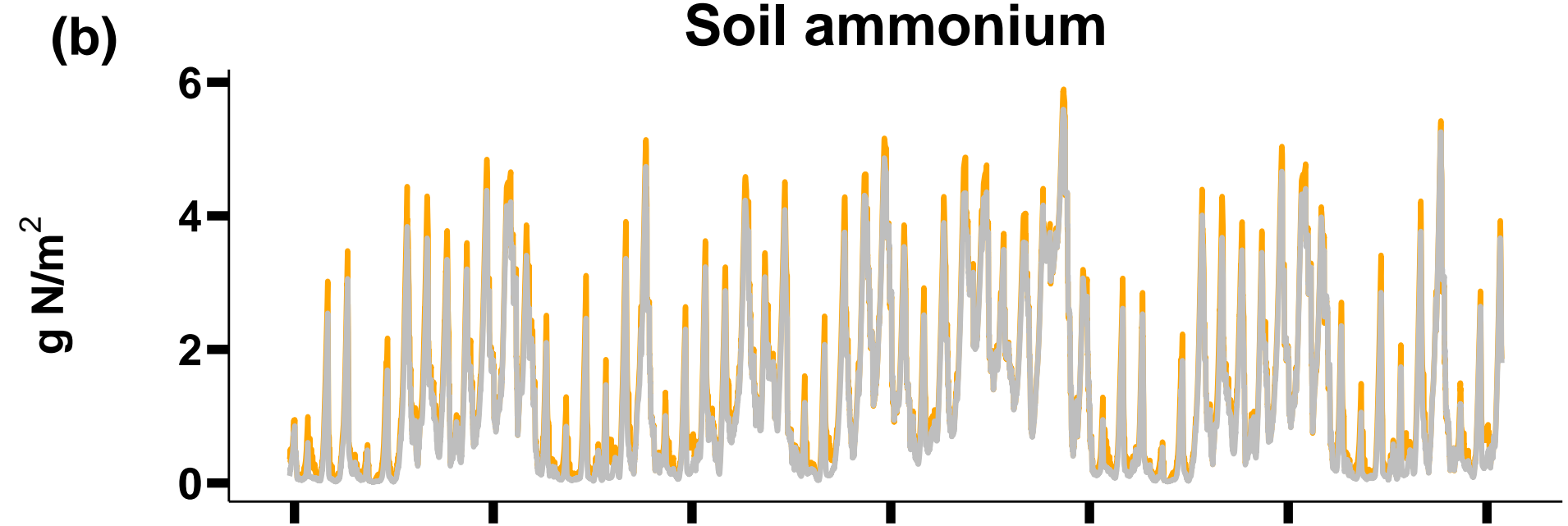
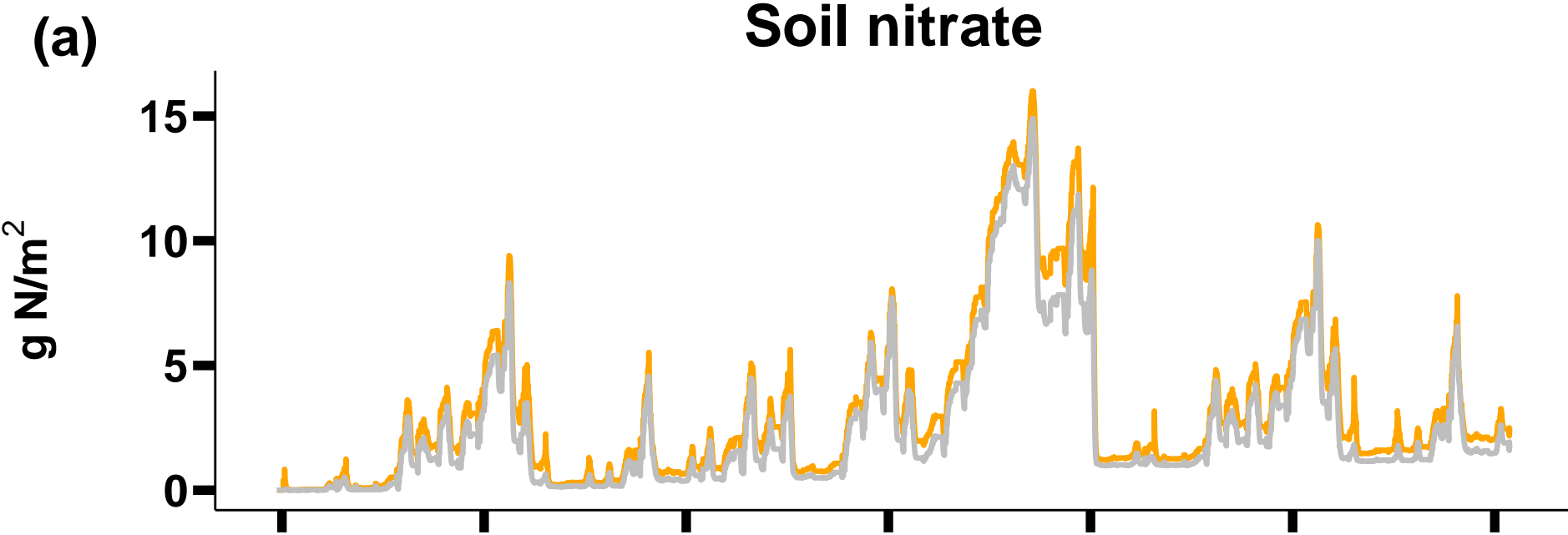
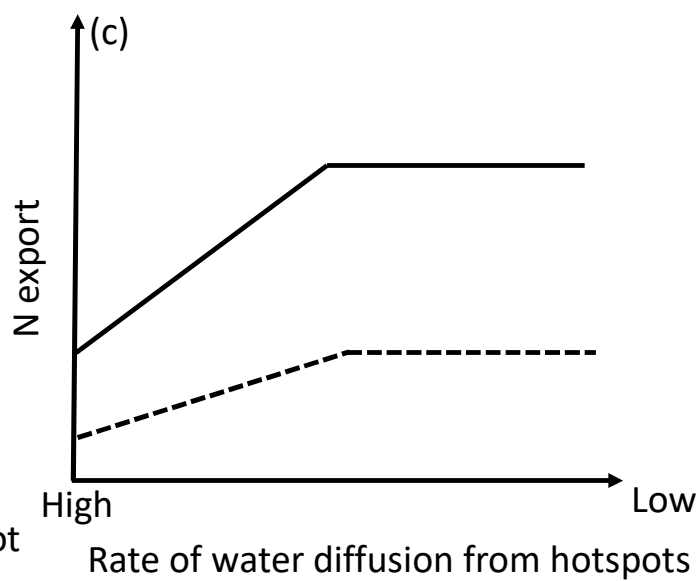
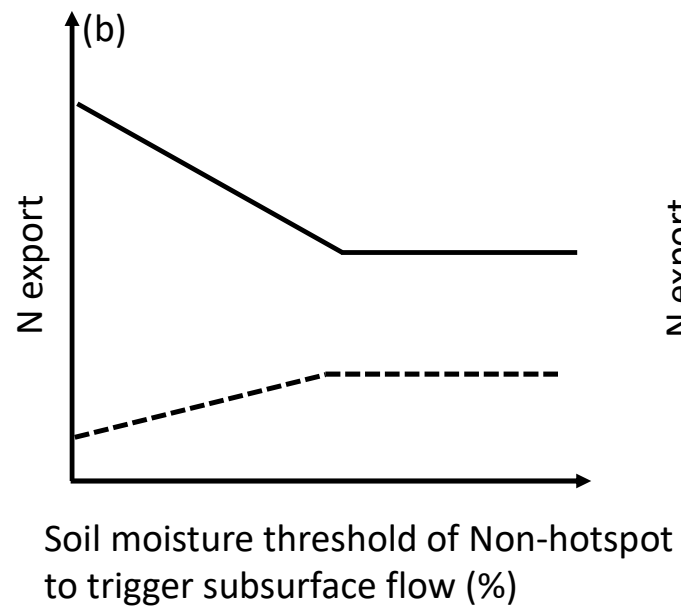
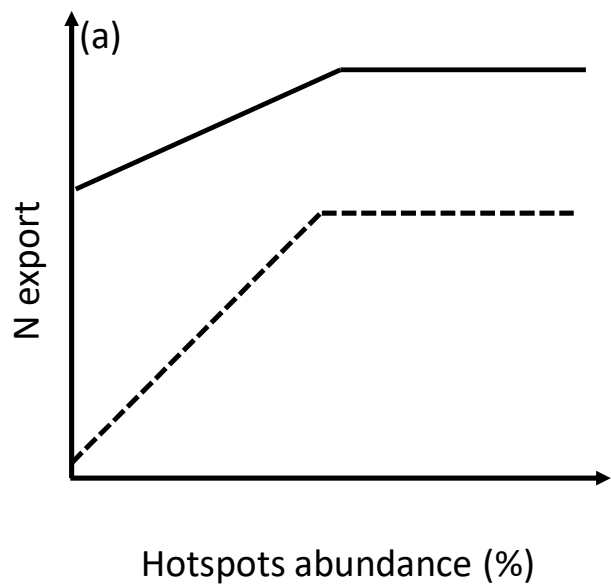


Figure 9.



— With hotspot — Without hotspot

Figure 10.



———— Streamflow nitrate

- - - - - Denitrification

1 **Simulating the role of biogeochemical hotspots in driving nitrogen export**  
2 **from dryland watersheds**

3 <sup>1</sup>Jianning Ren, <sup>1</sup>Erin J. Hanan, <sup>2</sup>Aral Greene, <sup>3</sup>Christina Tague, <sup>4</sup>Alexander H. Krichels, <sup>1</sup>William  
4 D. Burke, <sup>5</sup>Joshua P. Schimel, <sup>2</sup>Peter M. Homyak

5 <sup>1</sup>Department of Natural Resources and Environmental Science, University of Nevada, Reno,  
6 89501, Reno, USA

7 <sup>2</sup>Department of Environmental Sciences, University of California, Riverside, 92521, Riverside,  
8 USA

9 <sup>3</sup>Bren School of Environmental Science & Management, University of California, Santa Barbara,  
10 93106, Santa Barbara, USA

11 <sup>4</sup>USDA Forest Service Rocky Mountain Research Station, 87102, Albuquerque, USA

12 <sup>5</sup>Department of Ecology, Evolution and Marine Biology, University of California, Santa Barbara,  
13 93106, Santa Barbara, USA

14 Correspondence:

15 Jianning Ren ([nren@unr.edu](mailto:nren@unr.edu), [renjianning@gmail.com](mailto:renjianning@gmail.com))

16 Erin Hanan ([ehanan@unr.edu](mailto:ehanan@unr.edu))

17 Key Points:

- 18 • We developed a model framework to represent biogeochemical hotspots in dryland  
19 ecosystems.
- 20 • Nitrogen export is sensitive to parameters controlling hotspot abundance, subsurface  
21 hydrologic connectivity, and soil moisture dynamics.
- 22 • The abundance and physical characteristics of hotspots can affect the timing of hot  
23 moments.

24 **Abstract**

25           Climate change and nitrogen (N) pollution are altering biogeochemical and  
26 ecohydrological processes in dryland watersheds, increasing N export, and threatening water  
27 quality. While simulation models are useful for projecting how N export will change in the  
28 future, most models ignore biogeochemical “hotspots” that develop in drylands as moist  
29 microsites become hydrologically disconnected from plant roots when soils dry out. These  
30 hotspots enable N to accumulate over dry periods and rapidly flush to streams when soils wet up.  
31 To better project future N export, we developed a framework for representing hotspots using the  
32 ecohydrological model RHESSys. We then conducted a series of virtual experiments to  
33 understand how uncertainties in model structure and parameters influence N export. Modeled  
34 export was sensitive to the abundance of hotspots in a watershed, increasing linearly and then  
35 reaching an asymptote with increasing hotspot abundance. Peak streamflow N was also sensitive  
36 to a soil moisture threshold at which subsurface flow from hotspots reestablished, allowing N to  
37 be transferred to streams; it increased and then decreased with an increasing threshold value.  
38 Finally, N export was generally higher when water diffused out of hotspots slowly. In a case  
39 study, we found that when hotspots were modeled explicitly, peak streamflow nitrate export  
40 increased by 29%, enabling us to better capture the timing and magnitude of N losses observed  
41 in the field. N export further increased in response to interannual variability in precipitation,  
42 particularly when multiple dry years were followed by a wet year. This modeling framework can  
43 improve projections of N export in watersheds where hotspots play an increasingly important  
44 role in water quality.

## 45 **1 Introduction**

46 Climate change and atmospheric nitrogen (N) deposition are accelerating biogeochemical  
47 cycling in dryland ecosystems and increasing N loading in streams, which can pose a major  
48 threat to water quality (Borer & Stevens, 2022; Fenn et al., 2003). However, the extent to which  
49 deposited N is exported to streams remains difficult to predict, in part because models are limited  
50 in their ability to capture hotspots—defined as wetter microsites in the soil that have  
51 disproportionately high rates of biogeochemical cycling—which can strongly influence N fluxes  
52 in dryland soils (Vargas et al., 2013). For example, hotspots enable N to accumulate over dry  
53 periods and rapidly flush to streams when soils wet up (McClain et al., 2003; Parker & Schimel,  
54 2011). This can occur even when plants are N-limited because precipitation pulses can mobilize  
55 accumulated N more quickly than plants are able to take it up (Homyak et al., 2014). As the  
56 global distribution of drylands expands with climate warming (Seager et al., 2018), and as  
57 urbanization increases rates of N deposition (Borer & Stevens, 2022), it is critical to better  
58 account for the mechanisms driving N export in models (Gustine et al., 2022; Schimel, 2018).

59 Hotspots can range in size from microsites within soil aggregates (Ebrahimi & Or, 2018)  
60 to islands of fertility within landscape patches (Osborne et al., 2020). While landscape models  
61 may effectively represent the later by parameterizing plant physiological processes that promote  
62 resource heterogeneity—for example, transpiration-driven nutrient accumulation beneath woody  
63 plant canopies in savannas; (Ridolfi et al., 2008)—representing the role of microscale  
64 biogeochemical hotspots is much more challenging at watershed scales. For one, soil moisture  
65 and subsurface transport processes are often oversimplified and not fully integrated into  
66 landscape-scale N-cycling models (Ouyang et al., 2017; Poblador et al., 2017; Schmidt et al.,  
67 2007; Zhang et al., 2018). When models do incorporate coupled hydrological-biogeochemical

68 processes, they often reduce spatial heterogeneity by averaging soil hydraulic parameters across  
69 a basin (Crow et al., 2012; Lin et al., 2015; Tague, 2009; Zhu et al., 2012, 2015). As a result,  
70 these models do not capture the role of soil microsites that remain wetter than bulk soils for at  
71 least some time into the dry season. While more detailed representation of soil heterogeneity is  
72 needed, at least three key uncertainties remain in scaling microsite processes across an entire  
73 watershed: (1) how hotspots are distributed across watersheds (McClain et al., 2003) (2) the  
74 amount of precipitation required to reestablish for hydrological connection between hotspots and  
75 bulk soils and to generate subsurface flow (Zhu et al., 2018), and (3) how the physical  
76 parameters governing fine-scale water diffusion from hotspots are distributed across a watershed  
77 (Clark et al., 2017).

78 A common modeling approach to represent the effects of fine-scale spatial heterogeneity  
79 on large-scale hydrologic fluxes is to incorporate distributions of sub-grid state variables that  
80 influence large-scale fluxes (i.e., statistical-dynamical flux parameterizations occurring within a  
81 grid cell; the smallest spatially explicit model unit; Clark et al., 2017; Wood et al., 1992). For  
82 example, Burke et al. (2021) developed an approach using the ecohydrological model RHESSys,  
83 which uses a distribution of aspatial, sub-grid vegetation patches that interact to influence grid-  
84 scale ecohydrological processes. This approach can better capture spatial heterogeneity without  
85 requiring detailed spatial information at sub-grid scales or increasing computational costs. To  
86 better predict how climate change modifies N retention and export, we developed a framework  
87 for modeling belowground hotspots and their interactions with soil moisture and subsurface flow  
88 by expanding the Burke et al. (2021) aspatial approach.

89

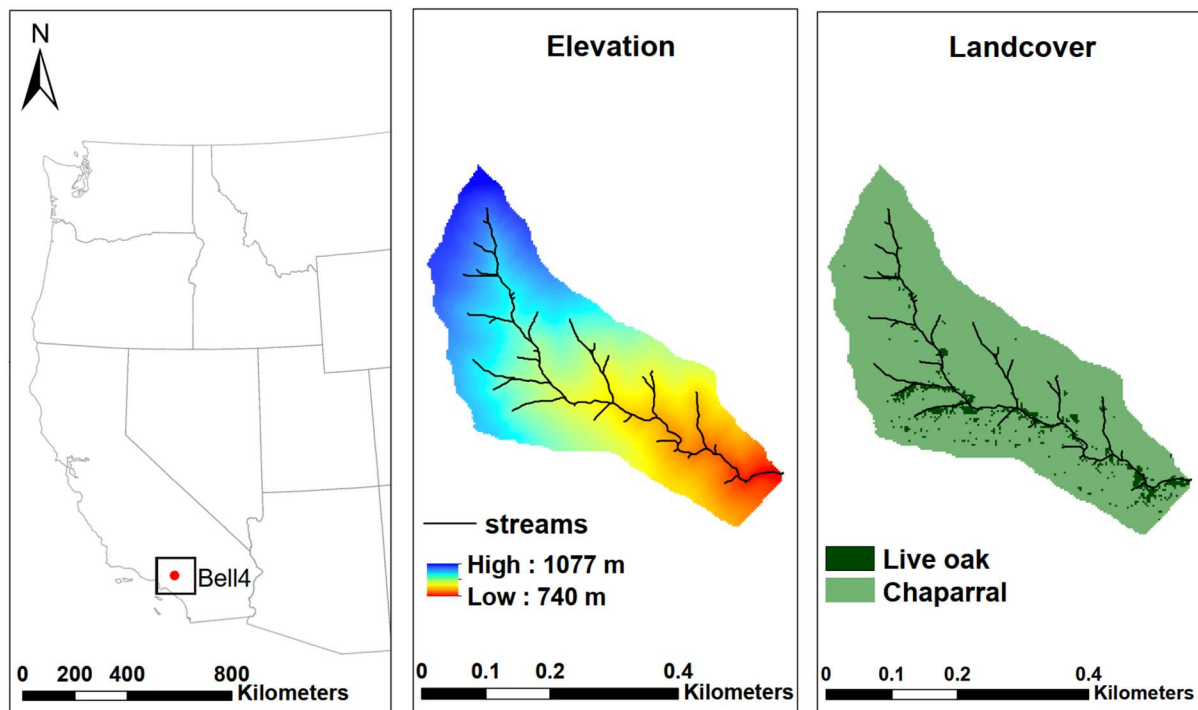
90 Our new modeling framework enables N to accumulate in microscale hotspots—  
91 represented aspatially within 10-m resolution grid cells—which contain sufficient moisture for  
92 decomposition to occur but are hydrologically disconnected from roots when the soils dry out.  
93 These micro-scale hotspot patches slowly lose water through diffusion and evaporation over the  
94 course of the dry season and can become hydrologically reconnected to the surrounding  
95 vegetated patches when soils wet up. Using this framework, we conducted a set of virtual  
96 experiments in a dryland, chaparral watershed in Southern California to characterize model  
97 sensitivity to three key sources of uncertainty: (1) the area percentage of hotspots within the  
98 watershed, (2) the length of time it takes for water to diffuse from hotspots during periods of  
99 drought, and (3) the moisture conditions under which hydrological connectivity between hotspot  
100 and non-hotspot locations reestablishes. Finally, we used field observations of N export to  
101 optimize the parameters controlling N dynamics and then with an optimized model, we  
102 investigated how precipitation patterns can influence hotspot effects on N export. This case study  
103 demonstrates how our modeling framework can be used to improve our theoretical understanding  
104 of the role biogeochemical hotspots play in N cycling and retention in drylands.

## 105 **2 Methods**

### 106 **2.1 Study area**

107 Model simulations were conducted in the Bell 4 basin (0.14 km<sup>2</sup>), which is part of the  
108 San Dimas experimental forest located northeast of Los Angeles, California (34°12'N, 117°47'E;  
109 Figure 1). Elevations in Bell 4 range from 700 to 1024 meters. The topography is characterized  
110 by steep slopes with steep channel gradients. Soils are shallow, coarse-textured sandy loams,  
111 which are weathered from granite (Chaney et al., 2016; Dunn et al., 1988) and classified as Typic  
112 Xerorthents (Soil Survey Staff, 2022) The region has hot, dry summers (June to September

113 around 17 mm precipitation) and cool, moist winters (698 mm precipitation); mean annual  
114 precipitation is around 715 mm and daily temperatures range from -8 °C to 40 °C. Vegetation  
115 cover is mainly mixed chaparral with chamise (*Adenostoma fasciculatum*), ceanothus  
116 (*Ceanothus spp.*), and black sage (*Salvia mellifera*) on south-facing slopes; ceanothus and  
117 California laurel (*Umbellularia californica*) on north-facing slopes; and some live oak (*Quercus*  
118 *agrifolia*) along riparian areas (Wohlgemuth, 2006).



120 *Figure 1. Bell 4 watershed in the San Dims experimental forest located in Southern California,*  
121 *U.S. (34°12'N, 117°47'E). The watershed is 0.14 km<sup>2</sup>.*

## 122 2.2 RHESSys model

123 The regional hydro-ecologic simulation system (RHESSys) is a spatially distributed,  
124 process-based model that simulates interacting ecohydrological and biogeochemical processes at  
125 multiple scales (Chen et al., 2020; Hanan et al., 2017; Tague, 2009; Tague & Band, 2004). The  
126 smallest spatial unit is the “patch,” which has a 10-meter resolution in the current study. At the

127 patch scale, vertical hydrologic fluxes include canopy interception, transpiration, evaporation,  
128 infiltration, capillary rise, and drainage from the rooting zone to the saturated zone. Carbon (C)  
129 cycling processes are tightly coupled with hydrology and soil moisture and include  
130 photosynthesis, allocation of net photosynthate, plant and soil respiration, and litter and soil  
131 decomposition. Nitrogen cycling includes atmospheric N deposition, mineralization, nitrification,  
132 immobilization, denitrification, plant uptake, and export to streams (Hanan et al., 2017; Lin et  
133 al., 2015). RHESSys has been parameterized and validated in several watersheds across the  
134 western USA, including in several chaparral watersheds (Burke et al., 2021; Chen et al., 2020;  
135 Hanan et al., 2017, 2021; Lin et al., 2015; Meentemeyer & Moody, 2002; Ren et al., 2021, 2022;  
136 Tague, 2009).

137         There are four layers for vertical soil moisture processes, including a surface detention  
138 store, a root zone store, an unsaturated store below the root zone, and a saturated store. The  
139 vertical hydrologic processes also include canopy layers, snowpack, and litter moisture stores.  
140 Rain throughfall from multiple canopy layers and a litter layer provide potential infiltration. If  
141 the precipitation falls as snow, snow throughfall updates a snowpack store. Then the surface  
142 detention storage receives water from canopy throughfall and snowmelt at a daily time step.  
143 Following precipitation and throughfall, water infiltrates into the soil following the Phillip  
144 (1957) infiltration equation. At a daily timestep, ponded water that has not infiltrated is added to  
145 detention storage and any water that is above detention storage capacity generates overland flow.

146         Infiltration updates one of three possible stores: a saturated store when the water table  
147 reaches the surface, a rooting zone store, or an unsaturated store for unvegetated patches. A  
148 portion of infiltrated water can bypass the rooting zone and unsaturated store through  
149 macropores. This bypass flow (carrying N) is added to a deeper groundwater store at the

150 subbasin scale. Water drains vertically from the unsaturated store or root zone store based on  
 151 hydraulic conductivity. Capillary rise moves water from the saturated zone to the root zone or  
 152 unsaturated store based on Eagleson (1978). Lateral fluxes can occur through both shallow  
 153 subsurface flow between patches and through bypass flow that contributes to a deeper hillslope-  
 154 scale groundwater flow model. Shallow subsurface saturated flow between patches follows  
 155 topography and changes with saturation deficit and transmissivity.

156 RHESSys simulates subsurface lateral redistribution of water and N between patches  
 157 based on topographic gradients and soil hydraulic parameters (Tague, 2009). Nitrification rates  
 158 in RHESSys are calculated based on the CENTURY<sub>NGAS</sub> model, where the nitrification rate is a  
 159 function of soil pH ( $f_{pH}$ ; Hanan et al 2017), moisture ( $f_{H_2O}$ ), soil temperature ( $f_T$ ), and available  
 160 soil ammonium ( $f_{NH_4}$ ; Parton, 1996):

$$161 \quad N_{nitri\text{f}} = \text{soil.NH4} \times f_{pH} \times f_{H_2O} \times f_T \times f_{NH_4} \quad \text{Eq (1)}$$

162 The pH scalar ( $f_{pH}$ ) is calculated as:

$$163 \quad f_{pH} = \frac{0.56 + \arctan(\pi \times 0.45 \times (-5 + pH))}{\pi} \quad \text{Eq (2)}$$

164 The soil moisture scalar ( $f_{H_2O}$ ) is calculated as:

$$165 \quad f_{H_2O} = \left(\frac{\theta - b}{a - b}\right)^d \left(\frac{b - a}{a - c}\right)^{\left(\frac{\theta - c}{a - c}\right)} d \quad \text{Eq (3)}$$

166 Where  $a$ ,  $b$ ,  $c$ , and  $d$  are parameters related to soil texture based on Parton et al. (1996) and  $\theta$  is  
 167 volumetric soil moisture.

168 The temperature scalar ( $f_T$ ) is calculated as:

$$169 \quad f_T = 0.06 + 0.13 \exp^{0.07T_{\text{soil}}} \quad \text{Eq (4)}$$

170 Where  $T_{soil}$  is the surface soil temperature in degrees C.

171 The ammonium concentration available for nitrification is calculated as:

$$172 \quad f_{NH_4} = 1.0 - \exp^{-0.0105 * NH_{4concl}} \quad \text{Eq (5)}$$

173 Where  $NH_{4con}$  is the soil ammonium concentration in the fast-cycling soil layer.

174 N export includes denitrification and subsurface lateral flow of ammonium, nitrate, and  
175 dissolved organic N (DON). Denitrification is calculated based on a maximum denitrification  
176 rate ( $R_{NO_3}$ ), and is modified by soil moisture ( $f_{H_2O}$ ), and soil respiration ( $f_{hrCO_2}$ ):

$$177 \quad N_{denitri} = R_{NO_3} \times f_{H_2O} \times f_{hrCO_2} \quad \text{Eq (6)}$$

178 The maximum denitrification rate is calculated as:

$$179 \quad R_{NO_3} = 0.0011 + \frac{a \tan(\pi \times 0.002 \times (\frac{NO_{3\_soil}}{N_{soil} + C_{soil}} - 180))}{\pi} \quad \text{Eq (7)}$$

180 Where  $NO_{3\_soil}$  is the available nitrate (kg N/m<sup>2</sup>) in soil and  $N_{soil}$  and  $C_{soil}$  are soil N (kg N/m<sup>2</sup>)  
181 and C (kg C/m<sup>2</sup>) amounts, respectively.

182 The soil moisture limitation is calculated as:

$$183 \quad f_{H_2O} = \frac{a}{b(\frac{c}{b^{d \times \theta}})} \quad \text{Eq (7)}$$

184  $\theta$ ,  $a$ ,  $b$ ,  $c$ , and  $d$  are defined in eq. 3 above.

185 The effect of soil respiration is calculated as:

$$186 \quad f_{hrCO_2} = \frac{0.0024}{1 + \frac{200}{e^{(3.5 \times hr)}}} - 0.00001 \quad \text{Eq (8)}$$

187 Where  $hr$  is total daily respiration (g C/m<sup>2</sup>/day).

188 Nitrate enters the soil from infiltration or from the surface detention store. Nitrate in the  
 189 soil is transported by subsurface flow in the saturated zone, while in the unsaturated soil, there is  
 190 no lateral nitrate transport (Chen et al., 2020; Tague & Band, 2004). Vertical distribution of  
 191 nitrate in the unsaturated zone soil profile is assumed to follow an exponential decay function,  
 192 where the surface layer has more nitrate and deeper soil has less. the available nitrate at soil  
 193 depth  $z$  is calculated as

$$194 \quad NO_{3\_soil}(z) = NO_{3\_surface} \times \exp^{-N_{decay} \times z} \quad \text{Eq (10)}$$

195 Where  $NO_{3\_surface}$  is nitrate at soil surface and  $N_{decay}$  is a soil specific parameter that defines the  
 196 rate of nitrate decay. When water is moving between the unsaturated zone and the saturated  
 197 zone, through downward leaching or upward capillary rise, nitrate moves with water based on its  
 198 concentration.

199 Nitrate export follows the flushing hypothesis (Chen et al., 2020). As the water table rises, more  
 200 N becomes available for flushing. The total soil nitrate export ( $NO_{3\_out}$ ) is calculated as the  
 201 integration of soil nitrate below the water table:

$$202 \quad NO_{3\_out} = \int_{z_{max}}^{z_s} \frac{q_z}{S_z} NO_{3\_soil} NO_{3\_mobile} \quad \text{Eq (11)}$$

203 Where  $z_{max}$  is the maximum water table depth,  $z_s$  is current water table depth,  $q_z$  is the net lateral  
 204 transport of water from the patch at depth  $Z$ ;  $S_z$  is the soil water content (in meters) and  $NO_{3\_mobile}$   
 205 is a parameter that defines the portion of nitrate that is mobile (related to soil type). Mobile  
 206 surface N can also be transported to deep ground water through preferential flow paths.

207 Recent improvements to RHESSys enable users to account for fine-scale (within patch)  
 208 heterogeneity (e.g., different types of vegetation cover and associated soil layers that may share

209 water within a single patch; Burke et al. 2021). These are referred to as "aspatial patches." When  
210 running RHESSys using the aspatial patch framework, "patch families" become the smallest  
211 spatially explicit model unit, and aspatial patches (nested within a patch family) are the smallest  
212 aspatial model unit. Note that an aspatial patch within a patch family is used to represent  
213 a distribution of a given vegetation type (e.g., trees or shrubs) based on observed (or  
214 hypothetical) distributions. It can but does not necessarily represent a single stand or clump  
215 of vegetation cover; vegetation from a single aspatial patch within a patch family does not have a  
216 defined distribution in RHESSys, so the assumption is that biophysical interactions, such as the  
217 extent to which a given cover type shares water, are more important than their physical location  
218 within the finest grid cell. Because there are no physical locations of aspatial patches within a  
219 patch family, within patch heterogeneity can be modeled without explicitly parameterizing and  
220 modeling fine scale spatial units that would be both computationally prohibitive and nearly  
221 impossible to parameterize with measured data.

222         Local water routing between aspatial patches inside a patch family is based on root access  
223 to water (Figure 2). Local routing moves water between aspatial patches based on user defined  
224 rules. Most commonly, water is distributed among aspatial patches as a function of relative  
225 differences between their rooting and unsaturated zone water contents and mediated by gaining  
226 and losing coefficients defined for each cover type. In this framework, an aspatial patch will gain  
227 water if its water content is below the patch family mean and vice versa, with the rate of water  
228 transfer controlled by sharing coefficients. Sharing coefficients to capture the integrated effects  
229 of uncertain, fine-scale variation in root distributions, and how root distributions and forest  
230 structure interact with fine-scale soil drainage characteristics. Nitrate and dissolved organic C are

231 exchanged along with water during local routing. A detailed description of aspatial patches can  
232 be found in Burke et al. (2021).

### 233 **2.3 Model development**

234 To enable RHESSys to account for biogeochemical hotspots, we expanded the aspatial  
235 patch framework to incorporate “hotspot” aspatial patches within each patch family. These  
236 aspatial patches represent a distribution of unvegetated microsites where biogeochemical cycling  
237 can be hydrologically disconnected, as soils dry out, from aspatial patches that contain plant  
238 roots (Figure 2). To model hotspot aspatial patches (hereafter called hotspots), we implemented  
239 three key model developments: (1) model algorithms that enable hotspots to access soil and litter  
240 C and N from neighboring non-hotspot patches for decomposition and biogeochemical cycling,  
241 and (2) algorithms and parameters that control the moisture conditions under which hotspots are  
242 hydrologically disconnected from other aspatial patches in the saturated zone, (3) parameters that  
243 control water diffusion in the unsaturated and/or root zone between hotspot and non-hotspot  
244 patches as soils dry out.

245 Research has shown that N-rich microsites can occur in unvegetated locations where  
246 there is less N uptake and less water demand from plants (Zhu et al., 2018). In the original  
247 RHESSys framework, unvegetated patches were used to represent large (e.g., 10 to 30-m) areas  
248 with no vegetation. Without vegetation inputs, these patches did not develop C and N stores to  
249 support microbial biogeochemical cycling. To generate hotspots, we implemented a litter sharing  
250 scheme that moves litter from vegetated aspatial patches to hotspots at an annual timestep to  
251 coincide with litter fall (Figure 2). Because we assume that hotspot aspatial patches occur at fine  
252 scales across a given 10-m patch family, it is reasonable to assume that they have access to plant  
253 litter for decomposition and N cycling from other aspatial patches within the patch family. The

254 amount of litter shared ( $CN_{share}$ ) is a function of the mean litter C and N content of the patch  
 255 family ( $CN_{mean}$ ), where the amount of C and N in a hotspot patch after litter sharing ( $CN_{hotspot}$ )  
 256 cannot be above the patch family mean (Eq 12). To enable N cycling in hotspots, hotspots also  
 257 have access to 1% of the protected soil organic C and N pools from the vegetated patch families.  
 258 The litter C and N routing is described as

$$259 \quad CN_{share} = \frac{(\sum_{i=1}^{n_{veg}} (CN_{veg\_i} - CN_{mean}) \times coef\_litter)}{n_{hotspot}} \quad \text{Eq (12)}$$

$$260 \quad CN_{hotsp\_after} = \min (CN_{hotspot\_before} + CN_{share}, CN_{mean}) \quad \text{Eq (13)}$$

$$261 \quad CN_{veg\_after\_i} = CN_{veg\_i} - (CN_{veg\_i} - CN_{mean}) \times coef\_litter \quad \text{Eq (14)}$$

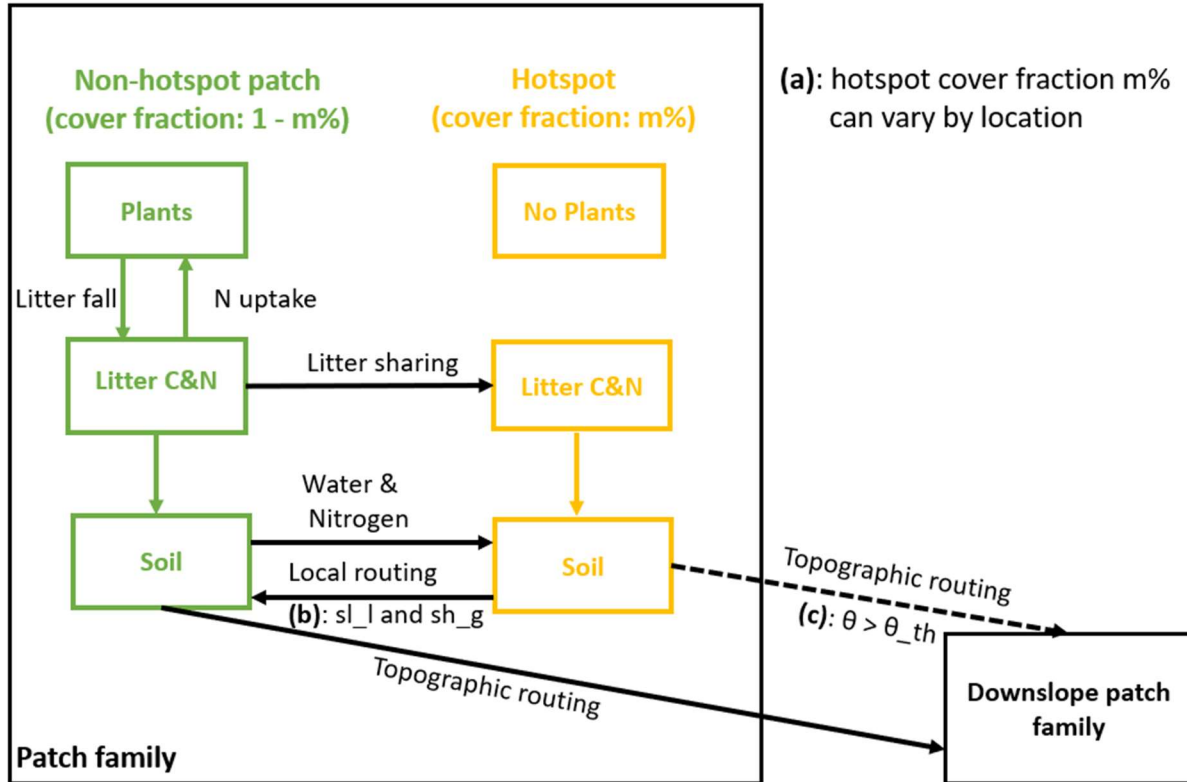
262 Where,  $n_{veg}$  is the number of non-hotspot patches in a patch family,  $CN_{veg}$  is the amount  
 263 of litter C and N in a non-hotspot patch,  $n_{hotspot}$  is the number of hotspot patches in a patch  
 264 family.  $Coef\_litter$  is the sharing coefficient parameter that controls the amount of litter sharing.  
 265 Hotspot patches can also be assigned a finer soil texture (e.g., loam), which can hold more water  
 266 than non-hotspot patches. In the current model, non-hotspot patches were comprised of sandy  
 267 loam (based on the POLARIS database; Chaney et al., 2016).

268 To control subsurface hydrologic flow from hotspots to vegetated patches, we set up a  
 269 soil moisture threshold for non-hotspot patches ( $\theta_{th}$ ), above which, water flows into them from  
 270 the saturated zone in hotspots. In other words, when non-hotspot patches dry down, they become  
 271 hydrologically disconnected from hotspots and they become reconnected when soils wet up  
 272 (Figure 2c & Eq 15).

$$273 \quad \begin{cases} \theta_{veg} > \theta_{th}: \text{subsurface flow move water and nitrate from hotspots to neighboring non - hotspot pathes} \\ \theta_{veg} \leq \theta_{th}: \text{no subsurface flow from hotspots to neighbor normal patches} \end{cases} \quad \text{Eq (15)}$$

274 This threshold is used to define a condition where “water films” can form as soils dry  
275 down, which enables microscale biogeochemical cycling while reducing nitrate leaching from  
276 hotspots over the course of the hot, dry summer (Parker & Schimel, 2011). When soils are  
277 rewetted at the onset of the rainy season, the water table rises, and hydrologic connectivity  
278 reestablishes between hotspot and non-hotspot patches. This can lead to rapid nitrification and  
279 nitrate export before plants become active and gain access to N that accumulated during dry  
280 periods of hydrologic disconnection (Parker & Schimel, 2011). While the thresholds at which  
281 hydrologic connectivity reestablishes are not currently well established, the threshold parameter  
282 can be calibrated to match field observations.

283 Although subsurface flow from hotspot patches remains somewhat disconnected during  
284 the dry season, water can still slowly diffuse from hotspots as soils dry out. To account for this,  
285 we developed water gain coefficients ( $sh\_g$ ) and water loss coefficients ( $sh\_l$ ) that constrain  
286 local routing to and from hotspots and the unsaturated and rooting zone in the surrounding non-  
287 hotspot patches (Figure 2a). During the dry season (June to November), the default  $sh\_g$  was set  
288 to 0.05 and  $sh\_l$  was set to 0.9 to simulate hotspots losing water. During the wet season  
289 (December to May), the default  $sh\_g$  was 0.9 and  $sh\_l$  was 0.05 to simulate hotspots gaining  
290 water. We rely on sharing coefficients here to capture “film” dynamics that depend on micro-  
291 scale characteristics that are not feasible to explicitly model but have been documented to  
292 influence hot-spot dynamics in field and lab-studies (Homyak et al., 2016; Parker & Schimel,  
293 2011). To summarize, while soil moisture gradients control whether routing occurs in the  
294 saturated zone between hotspot and non-hotspot patches, the sharing coefficients control the rate  
295 of local water transfer in the unsaturated zone.



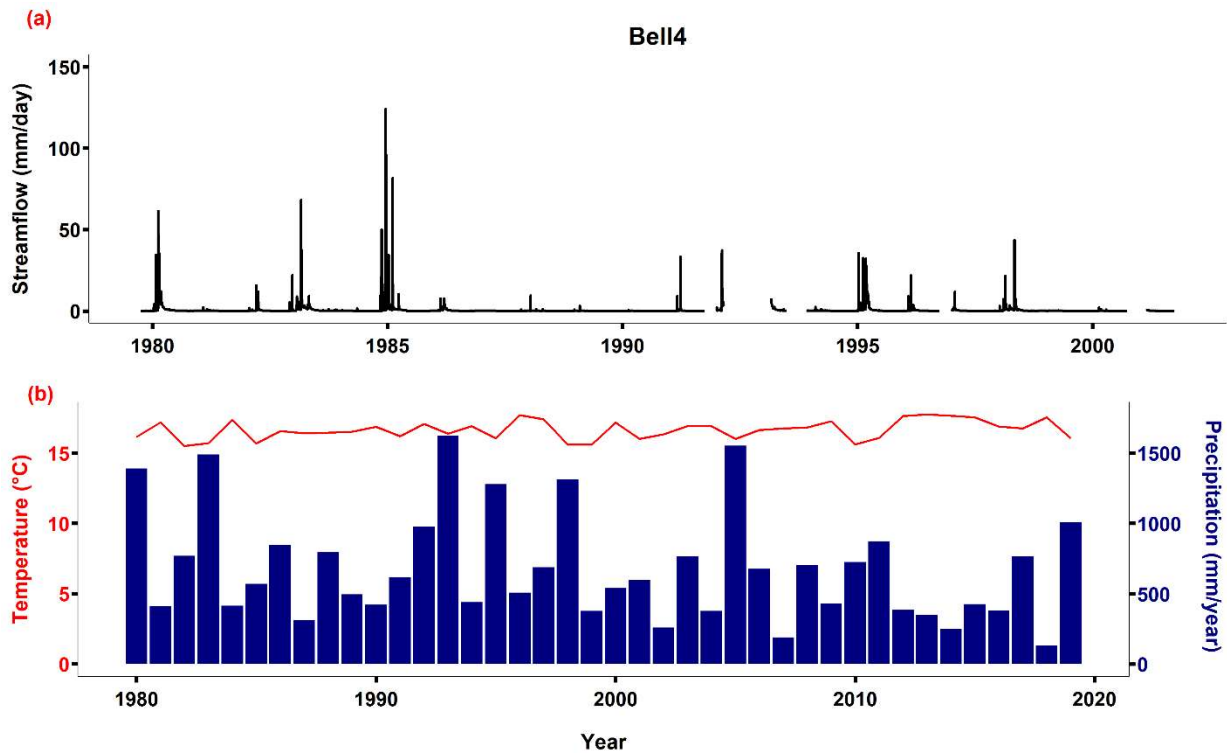
296

297 *Figure 2. Conceptual overview of hotspots patches nested within each patch family. Each year,*  
 298 *vegetated patches share litter C and N with hotspot patches from the portions of their stores that*  
 299 *are greater than the patch family means. Note that the conceptual figure does not indicate that*  
 300 *there is only one hotspot and one non-hotspot patch in a patch family, but rather represents their*  
 301 *cover fraction. Key model uncertainties include: (a) hotspot cover fraction  $m\%$ , which can vary*  
 302 *by location, (b) local routing of water and N in the unsaturated zone between aspatial patches*  
 303 *based on the mean water content of the patch family, which can be mediated by sharing*  
 304 *coefficients  $sh_l$  and  $sh_g$ ; and (c) topographic routing in the saturated zone from patches in one*  
 305 *patch family to patches in downslope patch families, which can be controlled by a soil moisture*  
 306 *threshold  $\theta_{th}$ . The dashed lines signify that hotspots are hydrologically disconnected from non-*  
 307 *hotspot patches during dry periods but reconnect during wet periods when soil moisture in non-*  
 308 *hotspot patch is larger than  $\theta_{th}$ . The extent of hydrological routing between hotspot and non-*  
 309 *hotspot patches is controlled by  $\theta_{th}$ , which can be calibrated to match field observations.*

## 310 2.4 Data

311 To generate metrological inputs for RHESSys scenarios in Bell 4 using the new hotspot  
 312 framework, we compared daily meteorological data from gridMET (Abatzoglou, 2013),  
 313 including maximum and minimum temperatures, precipitation, relative humidity, radiation, and  
 314 wind speed, from 1979 to 2020, to daily meteorological data at a station located near Bell 4 (San

315 Dimas Tanbark) from the U.S. Forest Service (USFS). Because gridMET matched closely with  
316 ground station data but does not require gap filling, gridMET was selected as a suitable  
317 meteorological forcing dataset for our analyses. To calibrate drainage parameters, we used  
318 streamflow data from the USFS for the years 1980 to 2002; data were missing for some months  
319 (Figure 3). We omitted 8 years of streamflow data (1984-1992) following a prescribed fire that  
320 occurred in 1984 (Meixner et al., 2006). We selected streamflow data from 1993 to 2002 for  
321 model calibration and 1980 to 1983 for validation (described in section 2.5 below).



322  
323 *Figure 3. Streamflow and climate data for Bell 4. The temperature is yearly average, and*  
324 *streamflow is calculated as the volume divided by the catchment area (0.14 km<sup>2</sup>).*

325 We aggregated a 1-m resolution Digital Elevation Model (DEM) from LiDAR to 10  
326 meters to represent topography across the watershed. To map landcover, we aggregated 1-m  
327 resolution land cover data from the National Agriculture Imagery Program (NAIP; collected on  
328 June 5, 2016) to 3-m and classified three land cover types: chaparral, live oak, and bare ground

329 (Maxwell et al., 2017). We then overlapped the 10-meter DEM with 3-meter vegetation cover  
330 data to classify aspatial patch distributions in each patch family using a k-means function  
331 (Hartigan & Wong, 1979) in R version 4.3.0 (R Core Team, 2022). This resulted in  
332 approximately 11 aspatial patches in each patch family and 375 different vegetation  
333 combinations across the watershed. We acquired soil texture data from POLARIS (Chaney et al.,  
334 2016).

335 To measure streamflow, two pressure transducers (Water level data loggers),  
336 compensated for barometric pressure (Barologgers; Solinst Canada Ltd, Georgetown, Ontario,  
337 Canada), were used to record stream stage at the Bell 4 weir. Water stage was measured at 5-  
338 minute intervals and converted to discharge using a rating curve developed for the v-notch weir.  
339 Stream samples were collected using an automatic sampler (Teledyne, ISCO model 6712C,  
340 Lincoln, Nebraska, US) set to collect 500-mL samples every 2 hours over a 48-hour period at the  
341 onset of flow. Samples were then filtered through pre-baked whatman GF/F filters and stored at -  
342 20 °C. Nitrate and ammonium concentrations were measured colorimetrically using an AQ2  
343 SEAL discrete analyzer (methods EPA-129-A and EPA-126-A).

## 344 **2.5 Model initialization, calibration, and evaluation**

345 We initialized the soil C and N pools by spinning them up to steady state (i.e., running  
346 the model until the pools stabilized). For the vegetation C and N pools, we used a target-driven  
347 method that allows vegetation to grow until it reaches target leaf area index (LAI) values from  
348 remote sensing data (Hanan et al., 2018). This method enables C and N pools to spin up  
349 mechanistically while still capturing landscape heterogeneity resulting from local resource  
350 limitations and disturbance histories. To construct a map of target LAI values, we chose the

351 clearest available NAIP image during the growing season (i.e., April 24, 2010). We then  
 352 calculated NDVI using equation 1.

$$353 \quad NDVI = \frac{\rho_{NIR} - \rho_R}{\rho_{NIR} + \rho_R} \quad (1)$$

354 In this equation,  $\rho_{NIR}$  is the reflectance in the near-infrared, and  $\rho_R$  is reflectance in the red  
 355 (Hanan et al., 2018). We then estimated LAI using a generalized NDVI-LAI model developed by  
 356 (Baret et al. 1989; equation 2).

$$357 \quad LAI = -\frac{1}{k} \times \ln \left( \frac{NDVI_{max} - NDVI}{NDVI_{max} - NDVI_{back}} \right) \quad (2)$$

358 Here,  $k$  is the extinction of solar radiation through a canopy.  $NDVI_{max}$  is the maximum NDVI  
 359 occurring in the region, and  $NDVI_{back}$  is the background NDVI (i.e., from pixels without  
 360 vegetation). We obtained  $k$  value from Smith et al. (1991) and White et al. (2000). The other  
 361 parameters were obtained for each vegetation type (Table 1).

362 *Table 1. Parameters used for calculating LAI from NDVI*

| Vegetation type | $k$   | $NDVI_{max}$ | $NDVI_{back}$ |
|-----------------|-------|--------------|---------------|
| Live oak        | 0.500 | 0.379        | -0.160        |
| Chaparral       | 0.371 | 0.372        | -0.160        |

363

364 We used observed streamflow for Bell 4 to calibrate six soil parameters: saturated  
 365 hydraulic conductivity ( $K_{sat}$ ), the decay of  $K_{sat}$  with depth (m), pore size index (b), air entry  
 366 pressure ( $\phi$ ), bypass flow to deeper groundwater storage ( $gw_1$ ), and deep groundwater drainage  
 367 rates to stream ( $gw_2$ ). We selected the best parameter set by comparing observed and modeled  
 368 streamflow using monthly Nash-Sutcliffe efficiency (NSE; Nash & Sutcliffe, 1970) and percent

369 error in annual flow estimates. NSE is used to evaluate peak flows and can range from  $-\infty$  to 1,  
 370 where 1 represents a perfect fit between modeled and observed data. Percent error is used to  
 371 compare differences between the total quantity of modeled and observed streamflow; values  
 372 closer to zero represent better fit.

373 **2.6 Sensitivity analyses and simulation scenarios:**

374 After model initialization and calibration, we used the new model framework to build in  
 375 microscale hotspots. We assumed the hotspots were evenly distributed across the landscape and  
 376 converted one bare ground patch inside of every patch family to an aspatial hotspot patch. Note  
 377 that this does not mean that there was only one hotspot in a patch family, but one aspatial patch  
 378 was used to represent the distribution (or percent cover) of microscale hotspots. If no bare  
 379 ground patches existed in the patch family, we instead converted a chaparral patch to an aspatial  
 380 hotspot patch. Because there were approximately 11 patches in each patch family, this setup  
 381 resulted in approximately 9% of each patch family (and of the overall basin) consisting of  
 382 microscale hotspots. We also assigned a loam soil texture to hotspot patches to represent the soil  
 383 physical properties that may also increase moisture retention. The default parameters used to  
 384 represent hotspot hydrological and biogeochemical dynamics are shown in Table 2.

385 *Table 2. Default parameters for hotspots.  $sh\_l$  and  $sh\_g$  control water diffusion in the*  
 386 *unsaturated zone between hotspot and non-hotspot patches, the default values promote strong*  
 387 *seasonality in hotspot soil moisture. The soil moisture threshold controls water flow in the*  
 388 *saturated zone between hotspot and non-hotspot patches; the default value promotes the*  
 389 *maximum peak streamflow  $N$ . We defined one aspatial patch as a hotspot inside of each family.*  
 390 *This leads to 9.1% cover of hotspot patches evenly distributed across the landscape.*

| Parameters  | Value                               |
|---|-------------------------------------|
| Sharing coefficient of losing water in unsaturated zone from hotspots ( $sh\_l$ ) | Dry season: 0.9<br>Wet season: 0.05 |
| Sharing coefficient of gaining water in unsaturated zone of hotspots ( $sh\_g$ )  | Dry season: 0.05<br>Wet season: 0.9 |

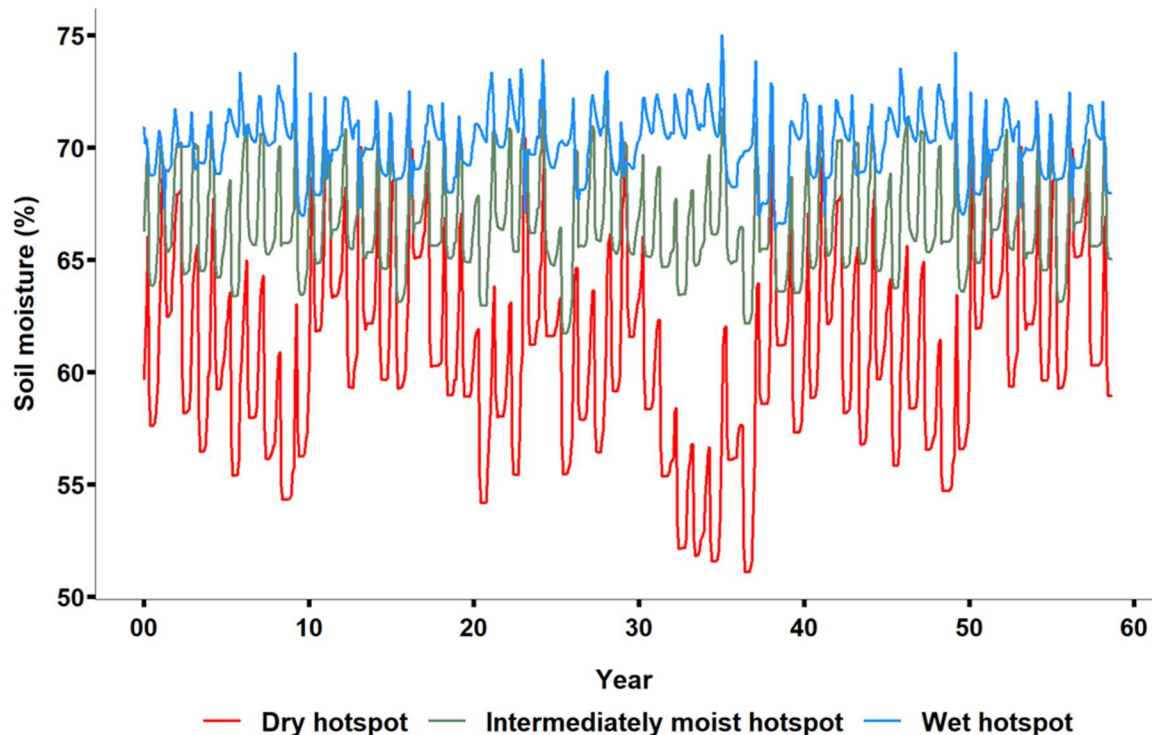
|   |      |
|---|------|
| Soil moisture threshold of non-hotspot above which water in saturated zone flows from hotspots to non-hotspot ( $\theta_{th}$ ) | 21%  |
| Percentage cover of hotspots  | 9.1% |
| Sharing coefficient of litter from non-hotspot patches to hotspot patches (coef_litter)   | 1    |

391

392 To evaluate the uncertainties related to model structure and parameters, we conducted a set of  
393 virtual experiments, or sensitivity analyses. For each sensitivity analysis, we ran RHESSys for 60  
394 years by looping the available climate data from 1979-2020. Results are presented as simulation  
395 years and capture the climate variability from the available record. First, we examined how the  
396 percentage cover of hotspots can influence N export. We built hotspot patches from zero percent  
397 to 13.7 percent at 2.3 percent increments (i.e., 0%, 2.2%, 4.5%, 6.8%, 9.1%, 11.4%, 13.7%).  
398 When the hotspot percentage was equal to 9.1%, there were exactly one aspatial hotspot patch in  
399 each patch family. When the hotspot percentage was larger than 9.1%, we needed to convert two  
400 aspatial patches in some patch families to hotspot patches. For example, the scenario with 11.4%  
401 hotspot cover at the watershed scale, required 2.3% of patch families to have two aspatial hotspot  
402 patches. Again, this does not mean that there were only one or two hotspots in a patch family,  
403 but one or two aspatial patches were used to represent their distribution.

404 Second, we investigated how the saturation status of hotspots influences nitrate export.  
405 We built three soil moisture conditions for hotspots by changing the sharing coefficients for local  
406 routing which influenced connectivity between hotspot and surrounding patches (Figure 2b): wet  
407 (sh\_l was 0.05 and sh\_g was 0.9 throughout the year; water diffused slowly from hotspots), dry  
408 (sh\_l and sh\_g were set to default values, hotspots diffused water quickly during the dry season),  
409 and intermediate (sh\_l was 0.1 and sh\_g was 0.8 during the dry season but used default values in  
410 the wet season; water diffused from hotspots at an intermediate rate). The hotspots in the wet

411 scenario were saturated almost all the time and had small interannual variation in soil moisture.  
412 The hotspots in the dry scenario lost water during dry periods and had large interannual soil  
413 moisture variation. The hotspots in the intermediate scenario had soil moisture dynamics in  
414 between the levels observed in the dry and wet scenarios (Figure 4).



415  
416 *Figure 4. Hotspot volumetric soil moisture conditions used to examine the sensitivity of N*  
417 *cycling and export to hotspot soil moisture saturation status and timing.*  
418         Lastly, we examined how uncertainty in the subsurface connectivity threshold parameter,  
419 which determines when non-hotspot patches become reconnected and can receive substantial N  
420 and water from the hotspot ( $\theta_{th}$ ; Figure 2c). By establishing conditions for this larger scale  
421 connectivity, this parameter can influence streamflow nitrate export. We then compared modeled  
422 streamflow nitrate export (under a range of parameter values based on the range of basin scale  
423 soil moisture: 0.15, 0.21, 0.25, 0.31, 0.35) to observed data (from 1988 to 2001).

424           Following the sensitivity analyses, we used available data and literature to estimate the  
425 most likely value for these parameters. We selected hotspot abundance of 9.1% assuming every  
426 patch family had the same hotspot coverage (using the default value in Table 2). We then  
427 selected the “dry” hotspot scenario in order to most closely match the seasonality of N dynamics  
428 observed in dryland ecosystems (Parker & Schimel 2011). Finally, as a simple optimization  
429 strategy, we selected a value for the soil moisture threshold parameter that enabled us to best  
430 capture observed peak N export. Then using these values, we conducted modeling scenarios to  
431 investigate how biogeochemical hotspots influence N export.

432           Modeling scenarios were based on the presence or absence of biogeochemical hotspots.  
433 For the hotspot scenario, we used the optimized soil moisture threshold determined using the  
434 approach described above, along with default parameters shown in Table 2, which created “dry”  
435 hotspots (i.e., with rapid water diffusion) that had distinct seasonality in denitrification as  
436 observed in field data (Li et al., 2006; Parker & Schimel, 2011). In this scenario, the hotspot  
437 patches received litter and protected C and N from vegetated patches and both biogeochemical  
438 and hydrologic processes still occurred within the hotspot patches. For the non-hotspot scenario,  
439 we used unvegetated patches in place of the hotspot patches, which were initialized to zero.  
440 However, in these unvegetated patches, we did not route litter and recalcitrant soil C and N from  
441 the vegetated patches. As a result, only hydrologic processes occurred there. We ran these two  
442 scenarios for 120 years, 60 years to stabilize the hotspot patches, and another 60 years to  
443 compare differences between scenarios.

## 444 **3 Results**

### 445 **3.1 Initialization and calibration results**

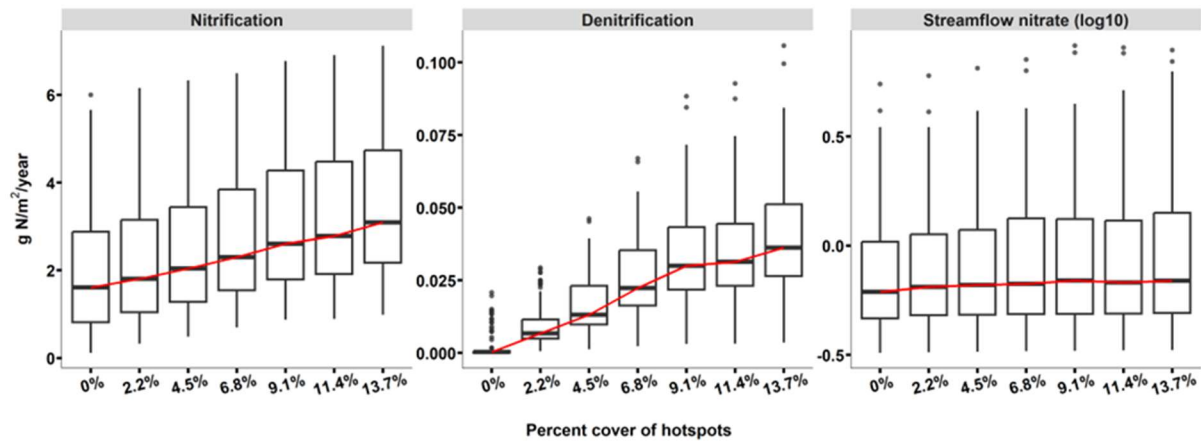
446 Using the target-driven initialization method of Hanan et al. (2018), we were able to  
447 capture the spatial distribution of leaf area index (LAI) and associated C stores across the Bell 4  
448 watershed, with some minor underestimates in riparian areas (covered by live oak) and  
449 overestimates in a small percentage of patches, which occurred because RHESSys allocates C to  
450 LAI at the end of growing season. Overall, the initialized and remotely sensed LAI were a strong  
451 match (Figure S1).

452 During the calibration period, the monthly NSE (a metric to evaluate the extent to which  
453 models capture peak streamflow; values close to 1 represent the best correspondence between  
454 modeled and observed values) was 0.88. Percent error (a metric to evaluate total flow; values  
455 close to 0 represent low error in the total amount of streamflow for modeled vs. observed data)  
456 was 5.45%. For the evaluation period, the monthly NSE was 0.8 with a percent error of -3.92%.  
457 In general, the model captured the seasonality, recession, and low flow patterns observed in the  
458 streamflow record.

### 459 **3.2 Sensitivity of N fluxes to the abundance of hotspots**

460 Total N export increased with increasing hotspot cover and then reached an asymptote  
461 when hotspot cover was greater than 9.1% (Figure 5). Denitrification rates were very low in the  
462 zero percent hotspot cover scenario and increased with an increasing percentage of hotspot  
463 patches. However, the rate of increase declined when hotspot cover was greater than 9.1%.  
464 Median streamflow nitrate export began increasing when hotspot cover was above 4.5% but  
465 reached an asymptote at 9.1%. Maximum streamflow nitrate export also increased with  
466 increasing hotspot cover, but the rate of increase declined when cover was above 9.1%. This

467 occurred because increasing hotspot cover led to concomitant decreases in vegetation cover and  
 468 therefore less carbon and nitrogen inputs from vegetation to soil. As a result, N cycling processes  
 469 became limited by productivity of the patch family. Although this result was partly an artifact of  
 470 the model's structure—which resulted in more than one aspatial hotspot patch occurring in some  
 471 patch families when the hotspot percentage cover exceeded 9.1%—it still demonstrates the  
 472 mechanism by which increases in hotspot cover above a given threshold can decrease  
 473 productivity. However, the actual threshold value should be interpreted with caution.



474

475 *Figure 5. Sensitivity of N processes to the percent cover of hotspots. Box plots show 25<sup>th</sup>,*  
 476 *median, and 75<sup>th</sup> percentile values, and the red line connects the median of each scenario to show*  
 477 *trends. Streamflow nitrate is calculated as total mass of nitrate in discharge divided by the basin*  
 478 *area.*

479 **3.3 The sensitivity of N fluxes to the parameters controlling water diffusion during periods**  
 480 **of hydrologic disconnection.**

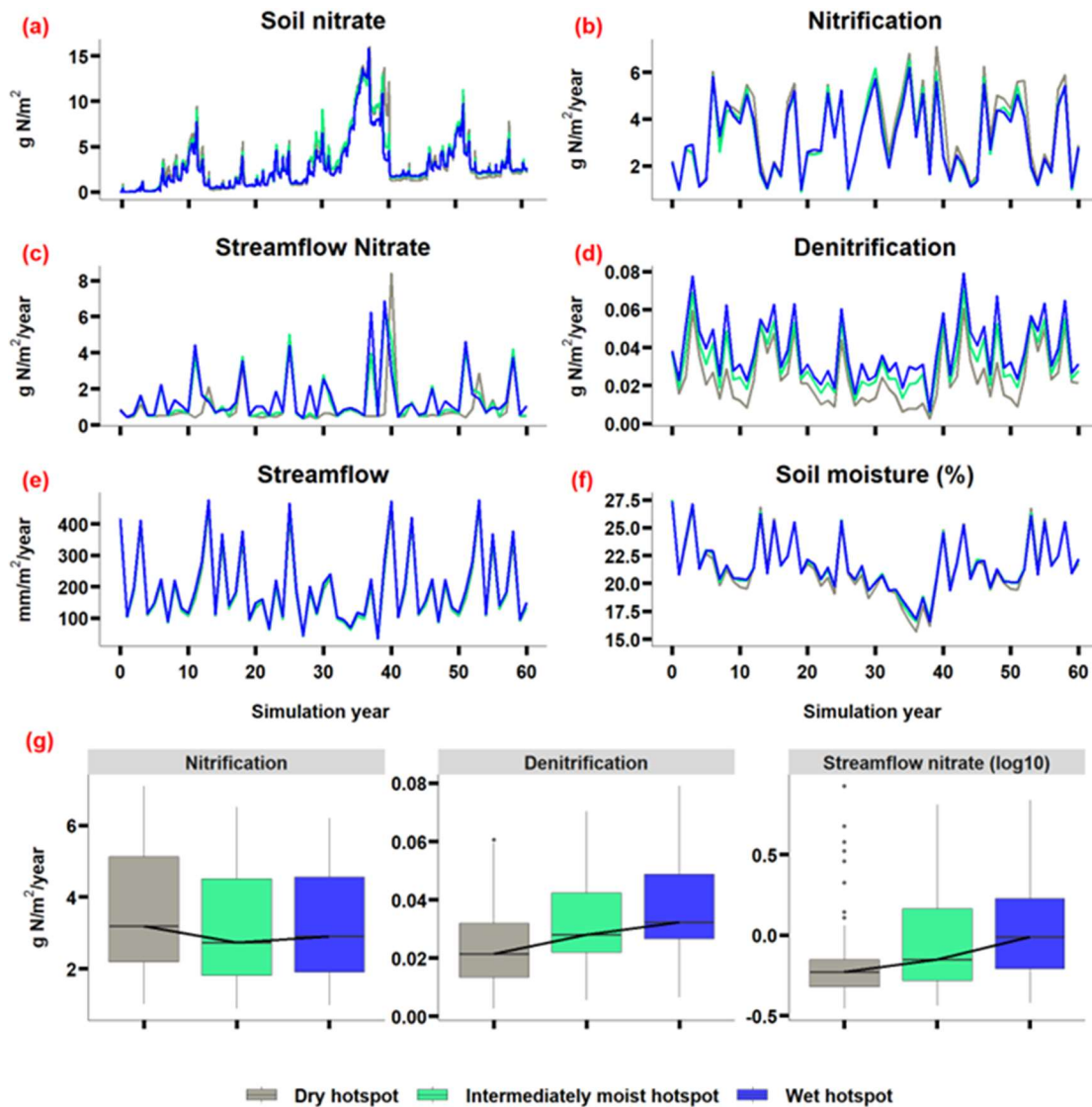
481 To examine how the rate at which hotspots dry out during periods of hydrologic  
 482 disconnection influences N fluxes, we ran three scenarios: a scenario where soil moisture in the  
 483 hotspots diffused slowly to non-hotspot patches and hotspots retained their soil moisture  
 484 throughout the year (i.e., a wet hotspot scenario), and a scenario where the diffusion speed was  
 485 intermediate (i.e., an intermediately moist hotspot scenario), and a scenario where soil moisture

486 diffused relative quickly from hotspot to non-hotspot patches (i.e., a dry hotspot scenario). We  
487 found that basin-scale nitrification rates can increase or decrease with the moisture content of  
488 hotspots (Figure 6 b&g). Higher moisture content in hotspots led to relatively lower moisture  
489 content in non-hotspot patches (based on water balance). In the wet-hotspot scenario, basin-scale  
490 nitrification was lower than in the dry-hotspot scenario where water slowly diffused to non-  
491 hotspot patches. This occurred because in the wet-hotspot scenario, soil moisture in non-hotspot  
492 patches was lower, which reduced total nitrification, even though nitrification rates increased in  
493 the hotspots.

494 Basin-scale denitrification increased with higher moisture content in hotspots since  
495 denitrification mainly occurs in those locations (Figure 6 d&g). For both nitrification and  
496 denitrification, the differences between the three scenarios were most pronounced during dry  
497 years when soil moisture differences between hotspots and non-hotspot patches were higher  
498 (Figure 6 b&d). During dry and average years, streamflow nitrate export was higher in the  
499 scenarios where hotspots remained saturated or close to saturated (i.e., the wet- and  
500 intermediately-moist- hotspot scenarios) than in the scenario where water diffused rapidly during  
501 dry periods (i.e., the dry-hotspot scenario). However, there was higher total annual and peak  
502 streamflow nitrate export during the wet years in the dry-hotspot scenario especially after  
503 multiple dry years (Figure 6c&e). Altogether, the closer hotspots are to being water-saturated,  
504 the more quickly N is exported to streamflow.

505 During multiple dry years, for the rapid diffusion (dry hotspot) scenario, nitrate  
506 accumulated in the saturated zone. Once a wet year occurred, that nitrate was flushed out to  
507 streams (Figure 6a). In the more continuously saturated (wet hotspot) hotspot scenario, higher  
508 denitrification, and faster leaching of nitrate from hotspots led to less nitrate accumulation in the

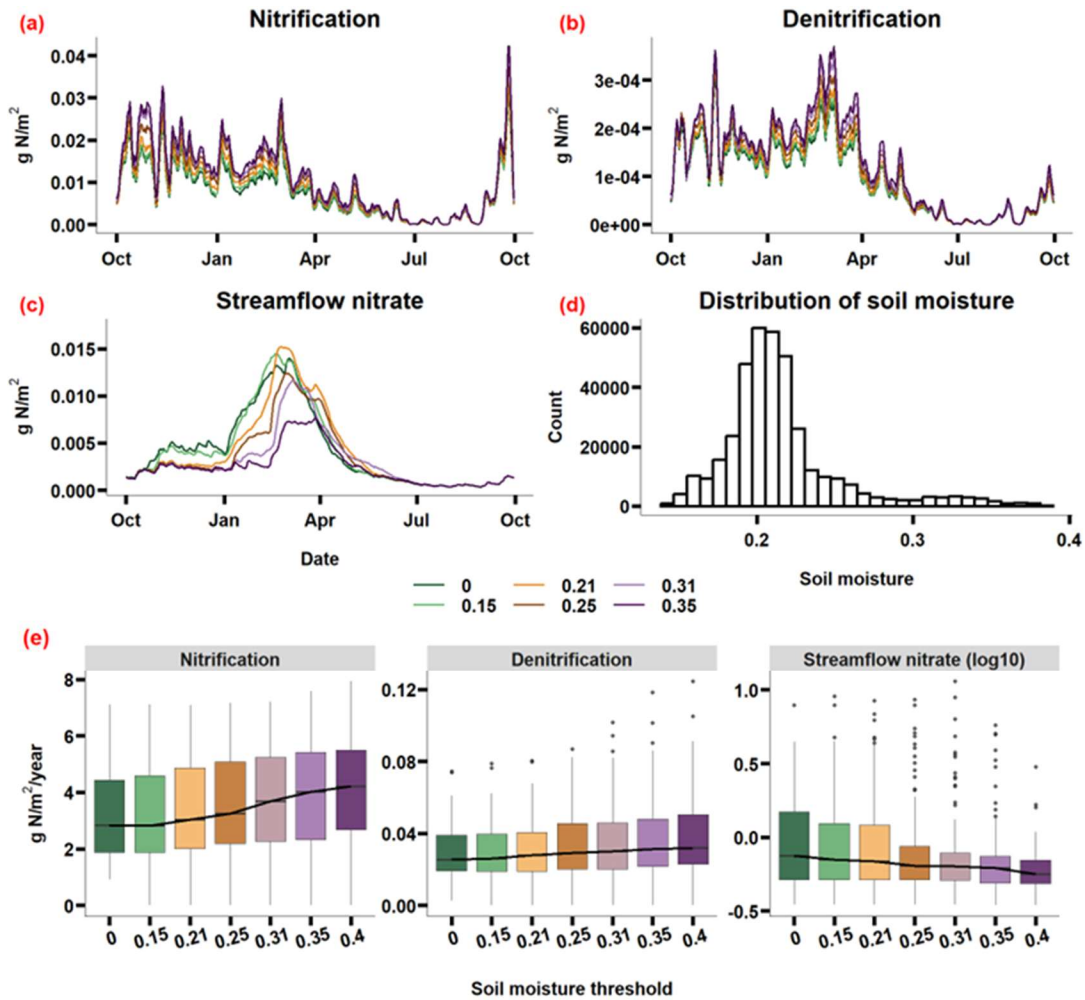
509 saturated zone. This suggests that soil moisture in hotspots and the subsurface flow interact to  
 510 drive N movement from soil to streams.



511  
 512 *Figure 6. N processes for three different scenarios, one where hotspots were saturated most of*  
 513 *the time (i.e., the slow diffusion, wet hotspot scenario), one where water diffused more rapidly*  
 514 *from hotspots during the dry season (i.e., the rapid diffusion, dry hotspot scenario), and one*  
 515 *where diffusion was intermediate (i.e., the intermediately moist hotspot scenario). Streamflow is*  
 516 *calculated as the average water depth over the basin area of Bell 4 (0.14 km<sup>2</sup>). Panel (g) is the*  
 517 *distribution of annual N fluxes, box plots show 25<sup>th</sup>, median, 75<sup>th</sup> percentile, and the black line*  
 518 *connects the median of each scenario.*

### 519 3.4 Sensitivity of N export to the subsurface connectivity parameter

520 The soil moisture threshold, which controls the connectivity of hotspots to non-hotspot  
521 patches, had a stronger influence on streamflow nitrate export than on nitrification and  
522 denitrification fluxes (Figure 7). This occurred because streamflow N export is influenced by  
523 both soil moisture content and subsurface lateral transport. Thus, when the threshold was high  
524 (i.e., when more moisture was required to establish hydrologic connectivity), streamflow N  
525 export was close to zero. With a higher soil moisture threshold, hotspots also tended to have  
526 higher moisture content, which increased nitrification and denitrification (Figure 7e), although  
527 the increases were small. The soil moisture threshold affected both the magnitude and timing of  
528 streamflow nitrate export. At a very low threshold of 0.15, there was higher magnitude and  
529 similar timing of peak nitrate export to streams compared to the no-threshold scenario (fully  
530 connected). This occurred because soil moisture in non-hotspot patches was higher than 0.15  
531 most of the time (Figure 7d). A threshold of 0.21, which was around the median basin-scale soil  
532 moisture, caused the largest peak in streamflow nitrate export. This occurred because  
533 connectivity was delayed until the threshold was reached, allowing nitrate to accumulate. When  
534 the threshold was larger than 0.21, peak streamflow nitrate was smaller and came later because  
535 hotspots were disconnected from non-hotspot patches most of the time.



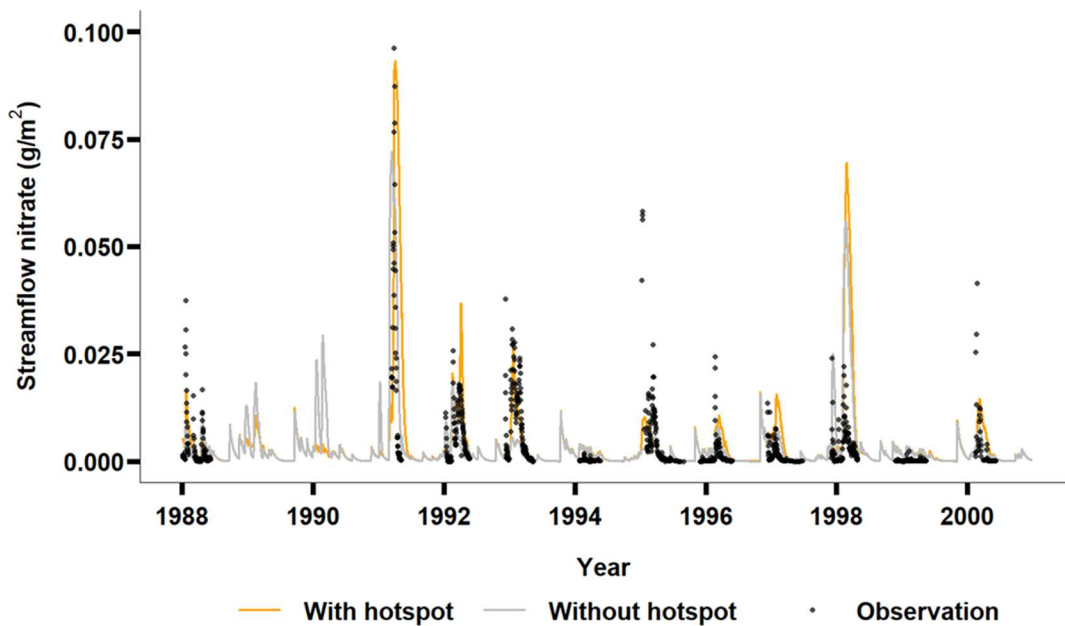
536

537 Figure 7. Sensitivity of N fluxes to the soil moisture threshold. Panels (a), (b) and (c) are mean  
 538 daily N fluxes over 60 years. Panel (d) is the distribution of daily soil moisture at the basin scale  
 539 over 60 years. Panel (e) is the distribution of annual fluxes, box plots show 25<sup>th</sup>, median, 75<sup>th</sup>  
 540 percentile, and the black line connects the median of each scenario. Different colors represent  
 541 different soil moisture thresholds.

### 542 3.5 Prediction of streamflow N export compared with observations.

543 We selected the optimal soil moisture threshold from section 3.2 for capturing the  
 544 magnitude of observed nitrate export (i.e., 0.21; this parameter value maximized peak  
 545 streamflow nitrate export) and we used the default values shown in Table 2 for the other  
 546 parameters. Using these values, we found that hydrologic disconnection of soil hotspots during  
 547 the dry periods and reconnection during wet periods enabled us to capture the observed

548 magnitude of nitrate export in streamflow, which we could not otherwise capture in the non-  
549 hotspot scenario (Figure 8). For example, the non-hotspot scenario underestimated nitrate export  
550 with a NSE of 0.22, while the hotspot scenario increased the estimation peak streamflow nitrate  
551 by 29% and captured its timing better with a NSE of 0.4 (in 1988, 1991, 1992, 1993, 2000).  
552 However, after optimizing the moisture threshold parameter, the timing of stream nitrate export  
553 was still slightly off; for example, in 1998, the modeled stream nitrate export peak was higher  
554 and occurred slightly later than observed.



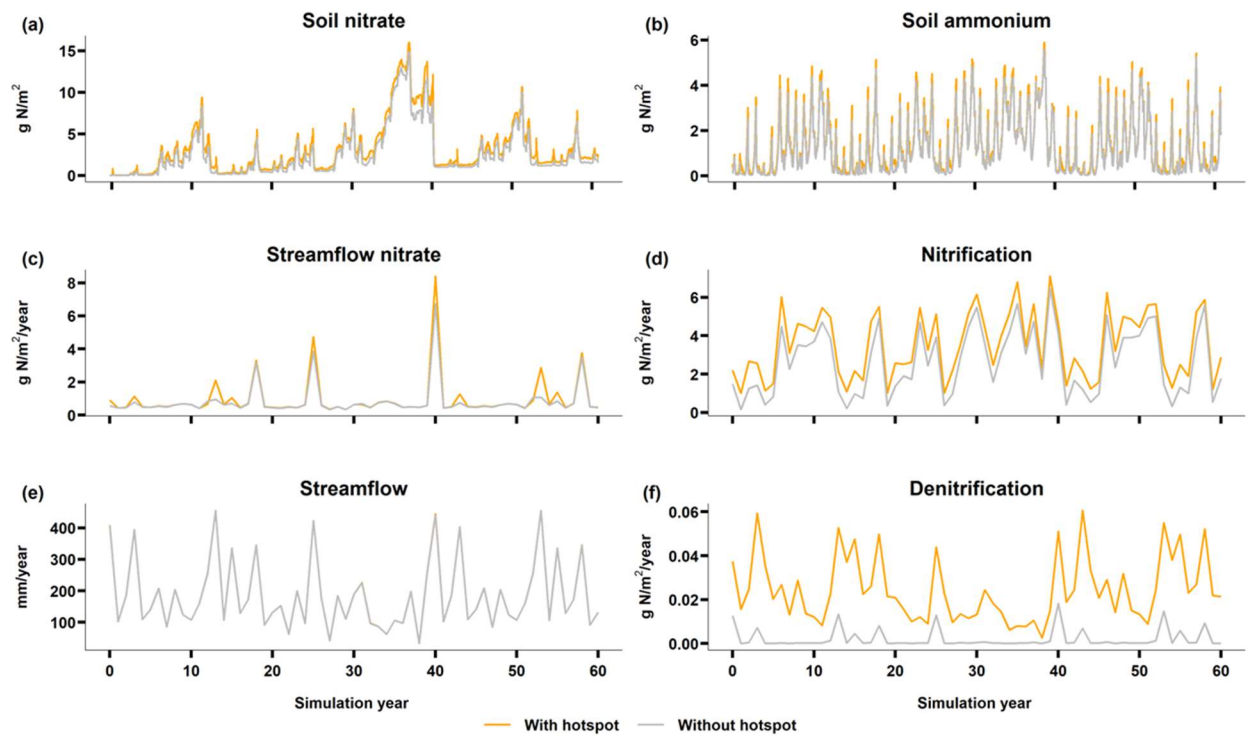
555

556 *Figure 8. Simulated and observed nitrate export in streamflow. The dots show observed*  
557 *streamflow nitrate.*

### 558 **3.6 Comparison of hotspot and non-hotspot scenarios**

559 At the basin-scale, there was higher N export in the hotspot scenario than in the non-  
560 hotspot scenario (Figure 9). Increases in streamflow nitrate with the hotspot scenario closely  
561 corresponded with increases in soil nitrate. Nitrate accumulated during dry years and there was  
562 substantial nitrate export to streams in wet years, especially when a wet year followed multiple

563 dry years (e.g., in year 40). We also found that streamflow nitrate export was further influenced  
 564 by interannual precipitation patterns. The differences between the hotspot and non-hotspot  
 565 scenarios were most evident during wet years when the basin was more connected. During wet  
 566 years, more nitrate was flushed out from hotspots, which illustrates how subsurface connectivity  
 567 can be an important factor driving streamflow N export. Consequently, the differences in  
 568 streamflow nitrate between the hotspot and non-hotspot scenarios were less consistent than the  
 569 differences in nitrification and denitrification, which had similar temporal patterns but differing  
 570 magnitude (e.g., Figure 9 c&d).

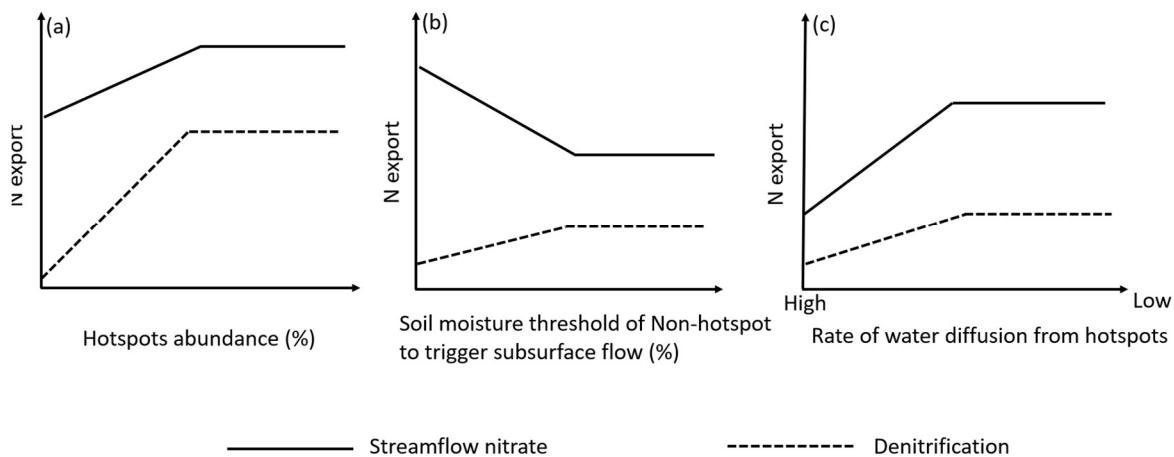


571  
 572 *Figure 9. Nitrogen and hydrologic cycling processes (annual sum) and nitrate pools (annual*  
 573 *mean) at the full basin scale for Bell 4.*

574 **4 Discussion**

575 Modeling hotspots at watershed scales has been challenging because most models,  
 576 including RHESSys, lack corresponding fine-scale (e.g., below 1-meter resolution) parameters

577 and variables (Tague, 2009). To address this limitation, we developed a framework for  
 578 representing hotspots aspatially within 10-m resolution patches. Using this framework, we  
 579 conducted a series of virtual experiments to investigate how uncertainties in model structure and  
 580 parameters influence N cycling and export. Then using the new modeling framework, we  
 581 examined how precipitation can affect N export in a dryland watershed in California. Our model  
 582 framework and virtual experiments improve our ability to connect plot-scale measurements to  
 583 catchment scale projections by developing integrative model algorithms and parameters that  
 584 control the biophysical behavior of hotspots across a landscape. These parameters can be  
 585 optimized using field observations of N cycling and export. We illustrate how uncertainty in  
 586 model parameters can influence projections of N export. Future research should aim to reduce  
 587 these uncertainties, and ultimately represent hotspot behavior more mechanistically across  
 588 watersheds.



589  
 590 *Figure 10. Conceptual framework summarizing how total annual streamflow nitrate and*  
 591 *denitrification respond to (a) hotspots abundance, (b) the soil moisture threshold required to*  
 592 *trigger subsurface flow, and (c) the rate of water diffusion from hotspots.*

#### 593 4.1. Uncertainties related to hotspot abundance and distribution

594 Estimating nitrogen (N) export at watershed and regional scales is limited by uncertainty  
595 in how hotspots are distributed across landscapes. Our research is among the few studies that  
596 have evaluated how hotspot abundance influences watershed-scale N export and illustrates the  
597 need to quantify hotspot cover to effectively scale N dynamics from ecosystems to watersheds  
598 (Anderson et al., 2015; Groffman, 2012). We parameterized the hotspots with varying cover  
599 percentages across a small watershed (0.14 km<sup>2</sup>) and found that N export increased with hotspot  
600 abundance (Figure 5& Figure 10), but with an asymptotic relationship due to limitations in N  
601 inputs and plant productivity (i.e., energy input for denitrification). However, in less N-limited  
602 and more mesic sites (e.g., under elevated N deposition and increasing precipitation), N export  
603 may be more sensitive to increasing hotspot abundance.

604 One limitation of our study is that we did not examine how the spatial distribution of  
605 hotspots influences N export. Previous research has shown that hotspots can be more  
606 concentrated in riparian corridors and wetlands where moisture content is higher (Pinay et al.,  
607 2015). We did however find that wet hotspots, which may serve as a surrogate for riparian and  
608 wetland locations, can in some cases increase both denitrification and N export in streams  
609 (Figure 6). However, because the location and arrangement of hotspots across a landscape can  
610 significantly influence streamflow N export (Laudon et al., 2011; Pinay et al., 2015), more  
611 research is needed to understand these spatial relationships (Haas et al., 2013). For example,  
612 combining high-resolution remote sensing data with field observations may help us better constrain  
613 hotspot distribution and abundance in ecohydrological models (Goodridge et al., 2018;  
614 Groffman, 2012; Tague, 2009; Walter et al., 2000).

## 615 4.2 Uncertainties in how rapidly hotspots dry out

616 Soil moisture is a major factor regulating denitrification and streamflow nitrate export  
617 (Pinay et al., 2015; Zhu et al., 2012). Our modeling experiments illustrate how the relationships  
618 between soil moisture and N dynamics can be complex and non-linear. Elevated soil moisture  
619 may reduce nitrification, increase denitrification, and ultimately decrease the amount of nitrate  
620 available for hydrologic flushing. Drier soils on the other hand can decrease denitrification and  
621 increase the amount of nitrate available for flushing (Homyak et al., 2016). We found that during  
622 dry and average years, higher moisture in hotspots increased nitrate infiltration from the  
623 unsaturated zone to the saturated zone, resulting in elevated and more rapid nitrate export to  
624 streams (Figure 6c). However, during wet years, higher soil moisture led to less nitrate export to  
625 streams due to increases in denitrification combined with less nitrate in the subsurface from the  
626 legacy effects of leaching in prior average and dry years. The dry hotspot scenario captured the  
627 observed nitrate-flushing better than the wet scenario, suggesting that hotspots are not likely to  
628 be continuously saturated (Figure 6). Because recent studies have shown that very small changes  
629 in soil moisture can change N fluxes abruptly (Castellano et al., 2013; Evans et al., 2016), it is  
630 important to improve our representation of soil moisture conditions in hotspots to accurately  
631 predict nitrate export.

632 Soil water residence time is an important factor affecting N export (Pinay et al., 2015;  
633 Zarnetske et al., 2011). The slower water diffuses from hotspots, the longer nitrate is exposed to  
634 denitrifying conditions (McClain et al., 2003). Our study shows that longer water residence time  
635 in hotspots (i.e., in the wet hotspot scenario) increases both denitrification and total N export to  
636 streams (Figure 6 & Figure 10). We used water diffusion coefficients to model water residence  
637 time in hotspots and we selected coefficients that enabled us to best capture the plausible timing

638 of denitrification and streamflow N fluxes. While this is a simplified, proxy approach, adding  
639 further complexity by explicitly modeling diffusion maybe infeasible since it would require  
640 local, spatially explicit soil parameters (Wood et al., 2011). However, further investigation into  
641 how proxy parameters may be calibrated is recommended for future research.

642 Stream nitrate export was also affected by precipitation patterns. When there were  
643 multiple dry years in a row, nitrate accumulated to a greater extent than in average years (Figure  
644 6a). When a wet year followed a multi-year drought, there was higher streamflow nitrate export  
645 in the dry hotspot scenario (Figure 6c). This is corroborated by field observations, which suggest  
646 that severe drought promoted nitrate accumulation in soil due to less denitrification and plant  
647 uptake, resulting in more nitrate available for flushing with the return of precipitation (Winter et  
648 al. 2023). We found that the length of drought and precipitation variability were more important  
649 in driving streamflow N export than the amount of precipitation (Figure 6c&e). For example,  
650 even with similar amount of precipitation in simulation years 26 and 40, N export was much  
651 higher in year 40 due to the legacy of a multi-year drought (Figure 6c&e). Recent research has  
652 similarly shown that precipitation variability can have positive or negative legacy effects on  
653 dryland productivity, which can in turn influence N cycling and export (Gherardi & Sala, 2015;  
654 Krichels et al., 2022). However, the direction of N responses vary along long-term precipitation  
655 gradients (Gherardi & Sala, 2015, 2019).

#### 656 **4.3 Uncertainties in hydrologic connectivity**

657 The subsurface flow threshold also plays a role in how much nitrate is transported to  
658 streams. In this study, we found that the optimal volumetric soil moisture to trigger subsurface  
659 flow from hotspot to non-hotspot patches was around 21% (Figure 7). Other studies have  
660 similarly shown that to trigger a subsurface flow, the soil moisture needs to reach a threshold of

661 18% (Liao et al., 2016). However, this threshold may vary with soil texture and water potential  
662 dynamics. While our new model framework can improve the prediction of streamflow nitrate  
663 with a static soil moisture threshold, topography and vegetation cover can also influence the  
664 connectivity and amount of subsurface flow, suggesting that soil moisture thresholds should be  
665 dynamic (Crow et al., 2012, Zhu et al., 2018).

666 Coupling soil biogeochemical models with hydrological models has become increasingly  
667 popular for investigating N cycling and export (Schimel, 2018). To save time, researchers  
668 typically prefer to couple existing models rather than build new ones (Malek et al., 2017; Zhu et  
669 al., 2018). Since most hydrologic models do not account for fine-scale heterogeneity in available  
670 moisture, they may not be able to capture biogeochemical hotspots even when coupled with  
671 biogeochemical models (Chen et al., 2020). Our new model framework provides a relatively  
672 simple way to capture hotspots without having to explicitly represent sub-meter scale spatial  
673 heterogeneity. While this intermediate complexity approach enables us to represent hotspots  
674 across a watershed, it does not fully capture some of the potential controls on hotspot function.  
675 For example, although our model captured the variability and magnitude of streamflow nitrate,  
676 there was some error associated with its timing (Figure 8). Future work can build upon our  
677 simple hotspot model to develop more process-based and dynamic representation of subsurface  
678 flow thresholds. This can be achieved by improving our understanding of hydrology and N  
679 processes in soil through hydrogeochemical observations.

#### 680 **4.4 The role of hotspots and hot moments in watershed models**

681 We found that the catchment-scale denitrification rate in the hotspot scenarios was  
682 significantly higher than that observed in the non-hotspot scenario (Figure 5& Figure 9), aligning  
683 with the concept that small areas often account for a high percentage of denitrification activity

684 (McClain et al., 2003). Additionally, denitrification was more sensitive to hotspot abundance,  
685 while N export to streams was more sensitive to the soil moisture threshold that triggers  
686 subsurface flow (Figure 10). Both are affected by the speed at which water diffuses from  
687 hotspots, which influences soil moisture levels, water residence time in soil, and vertical and  
688 horizontal transport of water. Our virtual experiments provide information on model uncertainty  
689 and sensitivity that can inform future studies focused on scaling N processes from plots to  
690 catchments. For example, in areas with high N deposition, managers who are interested in  
691 predicting how much N ends up in streams should focus on reducing model uncertainties in  
692 subsurface flow thresholds and soil moisture retention in hotspots.

693         In the context of predicting N export, hot moments—defined as wet periods after a  
694 prolonged dry spell (Groffman et al., 2009)—are currently better represented in the RHESSys  
695 model than hotspots. Even in our no hotspot scenario, there was a pulse of streamflow N export  
696 when wet years followed multiple dry years (Figure 6 & Figure 9). However, models of how hot  
697 moments influence streamflow N export are still limited by uncertainties in soil moisture  
698 dynamics. For instance, we found that in the wet hotspot scenario, there was an earlier  
699 streamflow N pulse than in the dry hotspot scenario (Figure 6c). Thus, hotspot conditions can  
700 affect the timing of hot moments, which has not been previously explored in modeling studies. In  
701 future studies, it is important to consider interactions between hotspots and hot moments rather  
702 than discussing them in isolation.

## 703 **5 Conclusion**

704         Coupling hydrologic processes with biogeochemical processes in watershed-scale models  
705 is challenging due to subsurface heterogeneity and the existence of hotspots and hot moments  
706 that are not well represented in models. We developed a framework for representing hotspots

707 explicitly in dryland watersheds and using this framework, we demonstrated how hydrologic  
708 connectivity and precipitation can affect N export in a dryland watershed in California. With  
709 increasing hotspot coverage (up to a threshold), both denitrification and N export to streams  
710 increased. The partitioning between denitrification and N-export, and the timing and magnitude  
711 of N-export were largely controlled by hotspot soil moisture dynamics. Specifically, we found  
712 that when the soil moisture threshold required for reestablishing subsurface flow was  
713 intermediate, nitrate was able to accumulate during drier periods and then be flushed to the  
714 stream upon wet up. This led to the highest peak nitrate export to streams, which tended to  
715 better-capture observed nitrate patterns. To our knowledge, this is the first time biogeochemical  
716 hotspots have been modeled explicitly using a coupled biogeochemical-ecohydrological model in  
717 a dryland watershed. This modeling framework can help better project N export in dryland  
718 watersheds where hotspots may play an increasingly important role in governing water quality as  
719 drought and N deposition continue to increase.

## 720 **6 Acknowledgments**

721 This project was supported by National Science Foundation of the United States under award  
722 number DEB-1916658. We thank Tom Dilts for helping with preparing input maps and data of  
723 RHESSys. We thank Pete Wohlgemuth for helping with streamflow data processing and model  
724 calibration. This study was supported in part by the USDA Forest Service Rocky Mountain  
725 Research Station. The findings and conclusions in this publication are those of the author and  
726 should not be construed to represent any official USDA or U.S. Government determination or  
727 policy.

## 728 **Conflict of Interest**

729 The authors declare no conflicts of interest relevant to this study.

### 730 **Data Availability Statement**

731 The data sets used to run simulations for this study can be found in the Open Science Forum:

732 <https://osf.io/ukpjpg/>, and the model code can be found on GitHub:

733 <https://doi.org/10.5281/zenodo.7754375>.

### 734 **References**

735 Abatzoglou, J. T. (2013). Development of gridded surface meteorological data for ecological

736 applications and modelling. *International Journal of Climatology*, 33(1), 121–131.

737 <https://doi.org/10.1002/joc.3413>

738 Anderson, T. R., Groffman, P. M., & Walter, M. T. (2015). Using a soil topographic index to

739 distribute denitrification fluxes across a northeastern headwater catchment. *Journal of*

740 *Hydrology*, 522, 123–134. <https://doi.org/10.1016/j.jhydrol.2014.12.043>

741 Baret, F., Olioso, A., Luciani, J. L., Hanocq, J. F., & Monterrot, J. C. (1989). Estimation à partir

742 de mesures de réflectance spectrale du rayonnement photosynthétiquement actif absorbé

743 par une culture de blé. *Agronomie*, 9(9), 885–895. <https://doi.org/10.1051/agro:19890906>

744 Borer, E. T., & Stevens, C. J. (2022). Nitrogen deposition and climate: an integrated synthesis.

745 *Trends in Ecology & Evolution*. <https://doi.org/10.1016/j.tree.2022.02.013>

746 Burke, W. D., Tague, C., Kennedy, M. C., & Moritz, M. A. (2021). Understanding How Fuel

747 Treatments Interact With Climate and Biophysical Setting to Affect Fire, Water, and

748 Forest Health: A Process-Based Modeling Approach. *Frontiers in Forests and Global*

749 *Change*, 3. <https://doi.org/10.3389/ffgc.2020.591162>

750 Castellano, M. J., Lewis, D. B., & Kaye, J. P. (2013). Response of soil nitrogen retention to the  
751 interactive effects of soil texture, hydrology, and organic matter. *Journal of Geophysical*  
752 *Research: Biogeosciences*, 118(1), 280–290. <https://doi.org/10.1002/jgrg.20015>

753 Chaney, N. W., Wood, E. F., McBratney, A. B., Hempel, J. W., Nauman, T. W., Brungard, C.  
754 W., & Odgers, N. P. (2016). POLARIS: A 30-meter probabilistic soil series map of the  
755 contiguous United States. *Geoderma*, 274, 54–67.  
756 <https://doi.org/10.1016/j.geoderma.2016.03.025>

757 Chen, X., Tague, C. L., Melack, J. M., & Keller, A. A. (2020). Sensitivity of nitrate  
758 concentration-discharge patterns to soil nitrate distribution and drainage properties in the  
759 vertical dimension. *Hydrological Processes*, 34(11), 2477–2493.  
760 <https://doi.org/10.1002/hyp.13742>

761 Clark, M. P., Bierkens, M. F. P., Samaniego, L., Woods, R. A., Uijlenhoet, R., Bennett, K. E., et  
762 al. (2017). The evolution of process-based hydrologic models: historical challenges and  
763 the collective quest for physical realism. *Hydrology and Earth System Sciences*, 21(7),  
764 3427–3440. <https://doi.org/10.5194/hess-21-3427-2017>

765 Crow, W. T., Berg, A. A., Cosh, M. H., Loew, A., Mohanty, B. P., Panciera, R., et al. (2012).  
766 Upscaling sparse ground-based soil moisture observations for the validation of coarse-  
767 resolution satellite soil moisture products. *Reviews of Geophysics*, 50(2).  
768 <https://doi.org/10.1029/2011RG000372>

769 Dunn, P. H., Barro, S. C., Wells, W. G., Poth, M. A., Wohlgenuth, P. M., & Colver, C. G.  
770 (1988). *The San Dimas experimental forest: 50 years of research* (No. PSW-GTR-104)  
771 (p. PSW-GTR-104). Berkeley, CA: U.S. Department of Agriculture, Forest Service,

772 Pacific Southwest Forest and Range Experiment Station. <https://doi.org/10.2737/PSW->  
773 GTR-104

774 Eagleson, P. S. (1978). Climate, soil, and vegetation: 3. A simplified model of soil moisture  
775 movement in the liquid phase. *Water Resources Research*, 14(5), 722–730.  
776 <https://doi.org/10.1029/WR014i005p00722>

777 Ebrahimi, A., & Or, D. (2018). On Upscaling of Soil Microbial Processes and Biogeochemical  
778 Fluxes From Aggregates to Landscapes. *Journal of Geophysical Research:*  
779 *Biogeosciences*, 123(5), 1526–1547. <https://doi.org/10.1029/2017JG004347>

780 Evans, S., Dieckmann, U., Franklin, O., & Kaiser, C. (2016). Synergistic effects of diffusion and  
781 microbial physiology reproduce the Birch effect in a micro-scale model. *Soil Biology and*  
782 *Biochemistry*, 93, 28–37. <https://doi.org/10.1016/j.soilbio.2015.10.020>

783 Fenn, M. E., Baron, J. S., Allen, E. B., Rueth, H. M., Nydick, K. R., Geiser, L., et al. (2003).  
784 Ecological Effects of Nitrogen Deposition in the Western United States. *BioScience*,  
785 53(4), 404–420. [https://doi.org/10.1641/0006-3568\(2003\)053\[0404:EEONDI\]2.0.CO;2](https://doi.org/10.1641/0006-3568(2003)053[0404:EEONDI]2.0.CO;2)

786 Gherardi, L. A., & Sala, O. E. (2015). Enhanced precipitation variability decreases grass- and  
787 increases shrub-productivity. *Proceedings of the National Academy of Sciences*, 112(41),  
788 12735–12740. <https://doi.org/10.1073/pnas.1506433112>

789 Gherardi, L. A., & Sala, O. E. (2019). Effect of interannual precipitation variability on dryland  
790 productivity: A global synthesis. *Global Change Biology*, 25(1), 269–276.  
791 <https://doi.org/10.1111/gcb.14480>

792 Goodridge, B. M., Hanan, E. J., Aguilera, R., Wetherley, E. B., Chen, Y.-J., D'Antonio, C. M.,  
793 & Melack, J. M. (2018). Retention of Nitrogen Following Wildfire in a Chaparral  
794 Ecosystem. *Ecosystems*, 21(8), 1608–1622. <https://doi.org/10.1007/s10021-018-0243-3>

795 Groffman, P. M. (2012). Terrestrial denitrification: challenges and opportunities. *Ecological*  
796 *Processes*, 1(1), 1–11. <https://doi.org/10.1186/2192-1709-1-11>

797 Groffman, P. M., Butterbach-Bahl, K., Fulweiler, R. W., Gold, A. J., Morse, J. L., Stander, E. K.,  
798 et al. (2009). Challenges to incorporating spatially and temporally explicit phenomena  
799 (hotspots and hot moments) in denitrification models. *Biogeochemistry*, 93(1–2), 49–77.  
800 <https://doi.org/10.1007/s10533-008-9277-5>

801 Gustine, R. N., Hanan, E. J., Robichaud, P. R., & Elliot, W. J. (2022). From burned slopes to  
802 streams: how wildfire affects nitrogen cycling and retention in forests and fire-prone  
803 watersheds. *Biogeochemistry*, 157(1), 51–68. [https://doi.org/10.1007/s10533-021-00861-](https://doi.org/10.1007/s10533-021-00861-0)  
804 [0](https://doi.org/10.1007/s10533-021-00861-0)

805 Haas, E., Klatt, S., Fröhlich, A., Kraft, P., Werner, C., Kiese, R., et al. (2013). LandscapeDNDC:  
806 a process model for simulation of biosphere–atmosphere–hydrosphere exchange  
807 processes at site and regional scale. *Landscape Ecology*, 28(4), 615–636.  
808 <https://doi.org/10.1007/s10980-012-9772-x>

809 Hanan, E. J., Tague, C. (Naomi), & Schimel, J. P. (2017). Nitrogen cycling and export in  
810 California chaparral: the role of climate in shaping ecosystem responses to fire.  
811 *Ecological Monographs*, 87(1), 76–90. <https://doi.org/10.1002/ecm.1234>

812 Hanan, E. J., Tague, C., Choate, J., Liu, M., Kolden, C., & Adam, J. (2018). Accounting for  
813 disturbance history in models: using remote sensing to constrain carbon and nitrogen pool  
814 spin-up. *Ecological Applications: A Publication of the Ecological Society of America*,  
815 28(5), 1197–1214. <https://doi.org/10.1002/eap.1718>

816 Hanan, E. J., Ren, J., Tague, C. L., Kolden, C. A., Abatzoglou, J. T., Bart, R. R., et al. (2021).  
817 How climate change and fire exclusion drive wildfire regimes at actionable scales.

818 *Environmental Research Letters*, 16(2), 024051. <https://doi.org/10.1088/1748->  
819 9326/abd78e

820 Hartigan, J. A., & Wong, M. A. (1979). Algorithm AS 136: A K-Means Clustering Algorithm.  
821 *Journal of the Royal Statistical Society. Series C (Applied Statistics)*, 28(1), 100–108.  
822 <https://doi.org/10.2307/2346830>

823 Homyak, P. M., Sickman, J. O., Miller, A. E., Melack, J. M., Meixner, T., & Schimel, J. P.  
824 (2014). Assessing Nitrogen-Saturation in a Seasonally Dry Chaparral Watershed:  
825 Limitations of Traditional Indicators of N-Saturation. *Ecosystems*, 17(7), 1286–1305.  
826 <https://doi.org/10.1007/s10021-014-9792-2>

827 Homyak, P. M., Blankinship, J. C., Marchus, K., Lucero, D. M., Sickman, J. O., & Schimel, J. P.  
828 (2016). Aridity and plant uptake interact to make dryland soils hotspots for nitric oxide  
829 (NO) emissions. *Proceedings of the National Academy of Sciences*, 113(19), E2608–  
830 E2616. <https://doi.org/10.1073/pnas.1520496113>

831 Krichels, A. H., Greene, A. C., Jenerette, G. D., Spasojevic, M. J., Glassman, S. I., & Homyak,  
832 P. M. (2022). Precipitation legacies amplify ecosystem nitrogen losses from nitric oxide  
833 emissions in a Pinyon–Juniper dryland. *Ecology*, n/a(n/a), e3930.  
834 <https://doi.org/10.1002/ecy.3930>

835 Laudon, H., Berggren, M., Ågren, A., Buffam, I., Bishop, K., Grabs, T., et al. (2011). Patterns  
836 and Dynamics of Dissolved Organic Carbon (DOC) in Boreal Streams: The Role of  
837 Processes, Connectivity, and Scaling. *Ecosystems*, 14(6), 880–893.  
838 <https://doi.org/10.1007/s10021-011-9452-8>

839 Li, X., Meixner, T., Sickman, J. O., Miller, A. E., Schimel, J. P., & Melack, J. M. (2006).  
840 Decadal-scale Dynamics of Water, Carbon and Nitrogen in a California Chaparral

841 Ecosystem: DAYCENT Modeling Results. *Biogeochemistry*, 77(2), 217–245.  
842 <https://doi.org/10.1007/s10533-005-1391-z>

843 Liao, K.-H., Lv, L.-G., Yang, G.-S., & Zhu, Q. (2016). Sensitivity of simulated hillslope  
844 subsurface flow to rainfall patterns, soil texture and land use. *Soil Use and Management*,  
845 32(3), 422–432. <https://doi.org/10.1111/sum.12282>

846 Lin, L., Webster, J. R., Hwang, T., & Band, L. E. (2015). Effects of lateral nitrate flux and  
847 instream processes on dissolved inorganic nitrogen export in a forested catchment: A  
848 model sensitivity analysis. *Water Resources Research*, 51(4), 2680–2695.  
849 <https://doi.org/10.1002/2014WR015962>

850 Malek, K., Stöckle, C., Chinnayakanahalli, K., Nelson, R., Liu, M., Rajagopalan, K., et al.  
851 (2017). VIC–CropSyst-v2: A regional-scale modeling platform to simulate the nexus of  
852 climate, hydrology, cropping systems, and human decisions. *Geoscientific Model*  
853 *Development*, 10(8), 3059–3084. <https://doi.org/10.5194/gmd-10-3059-2017>

854 Maxwell, A. E., Warner, T. A., Vanderbilt, B. C., & Ramezan, C. A. (2017). Land Cover  
855 Classification and Feature Extraction from National Agriculture Imagery Program  
856 (NAIP) Orthoimagery: A Review. *Photogrammetric Engineering & Remote Sensing*,  
857 83(11), 737–747. <https://doi.org/10.14358/PERS.83.10.737>

858 McClain, M. E., Boyer, E. W., Dent, C. L., Gergel, S. E., Grimm, N. B., Groffman, P. M., et al.  
859 (2003). Biogeochemical Hot Spots and Hot Moments at the Interface of Terrestrial and  
860 Aquatic Ecosystems. *Ecosystems*, 6(4), 301–312. [https://doi.org/10.1007/s10021-003-](https://doi.org/10.1007/s10021-003-0161-9)  
861 0161-9

862 Meentemeyer, R. K., & Moody, A. (2002). Distribution of plant life history types in California  
863 chaparral: the role of topographically-determined drought severity. *Journal of Vegetation*  
864 *Science*, 13(1), 67–78. <https://doi.org/10.1111/j.1654-1103.2002.tb02024.x>

865 Meixner, T., Fenn, M. E., Wohlgemuth, P., Oxford, M., & Riggan, P. (2006). N Saturation  
866 Symptoms in Chaparral Catchments Are Not Reversed by Prescribed Fire. *Environmental*  
867 *Science & Technology*, 40(9), 2887–2894. <https://doi.org/10.1021/es051268z>

868 Nash, J. E., & Sutcliffe, J. V. (1970). River flow forecasting through conceptual models part I —  
869 A discussion of principles. *Journal of Hydrology*, 10(3), 282–290.  
870 [https://doi.org/10.1016/0022-1694\(70\)90255-6](https://doi.org/10.1016/0022-1694(70)90255-6)

871 Osborne, B. B., Nasto, M. K., Soper, F. M., Asner, G. P., Balzotti, C. S., Cleveland, C. C., et al.  
872 (2020). Leaf litter inputs reinforce islands of nitrogen fertility in a lowland tropical forest.  
873 *Biogeochemistry*, 147(3), 293–306. <https://doi.org/10.1007/s10533-020-00643-0>

874 Ouyang, W., Xu, X., Hao, Z., & Gao, X. (2017). Effects of soil moisture content on upland  
875 nitrogen loss. *Journal of Hydrology*, 546, 71–80.  
876 <https://doi.org/10.1016/j.jhydrol.2016.12.053>

877 Parker, S. S., & Schimel, J. P. (2011). Soil nitrogen availability and transformations differ  
878 between the summer and the growing season in a California grassland. *Applied Soil*  
879 *Ecology*, 48(2), 185–192. <https://doi.org/10.1016/j.apsoil.2011.03.007>

880 Parton, W. J. (1996). The CENTURY model. In D. S. Powlson, P. Smith, & J. U. Smith (Eds.),  
881 *Evaluation of Soil Organic Matter Models* (Vol. 38, pp. 283–291). Springer, Berlin,  
882 Heidelberg: Evaluation of Soil Organic Matter Models.

883 Phillip, J. (1957). The theory of infiltration: 4. Sorptivity and algebraic infiltration equation. *Soil*  
884 *Sci*, 84, 257–264.

885 Pinay, G., Peiffer, S., De Dreuzy, J.-R., Krause, S., Hannah, D. M., Fleckenstein, J. H., et al.  
886 (2015). Upscaling Nitrogen Removal Capacity from Local Hotspots to Low Stream  
887 Orders' Drainage Basins. *Ecosystems*, *18*(6), 1101–1120. [https://doi.org/10.1007/s10021-](https://doi.org/10.1007/s10021-015-9878-5)  
888 [015-9878-5](https://doi.org/10.1007/s10021-015-9878-5)

889 Poblador, S., Lupon, A., Sabaté, S., & Sabater, F. (2017). Soil water content drives  
890 spatiotemporal patterns of CO<sub>2</sub> and N<sub>2</sub>O emissions from a Mediterranean riparian forest  
891 soil. *Biogeosciences*, *14*(18), 4195–4208. <https://doi.org/10.5194/bg-14-4195-2017>

892 R Core Team. (2022). R: A Language and Environment for Statistical Computing. Retrieved  
893 from <https://www.R-project.org/>

894 Ren, J., Adam, J. C., Hicke, J. A., Hanan, E. J., Tague, C. L., Liu, M., et al. (2021). How does  
895 water yield respond to mountain pine beetle infestation in a semiarid forest? *Hydrology*  
896 *and Earth System Sciences*, *25*(9), 4681–4699. [https://doi.org/10.5194/hess-25-4681-](https://doi.org/10.5194/hess-25-4681-2021)  
897 [2021](https://doi.org/10.5194/hess-25-4681-2021)

898 Ren, J., Hanan, E., Hicke, J., Kolden, C., Abatzoglou, J. T., Tague, C., et al. (2022, March 23).  
899 Bark beetle effects on fire regimes depend on underlying fuel modifications in semiarid  
900 systems [preprint]. <https://doi.org/10.1002/essoar.10510802.1>

901 Ridolfi, L., Laio, F., & D'Odorico, P. (2008). Fertility Island Formation and Evolution in  
902 Dryland Ecosystems. *Ecology and Society*, *13*(1). [https://doi.org/10.5751/ES-02302-](https://doi.org/10.5751/ES-02302-130105)  
903 [130105](https://doi.org/10.5751/ES-02302-130105)

904 Schimel, J. P. (2018). Life in Dry Soils: Effects of Drought on Soil Microbial Communities and  
905 Processes. *Annual Review of Ecology, Evolution, and Systematics*, *49*(1), 409–432.  
906 <https://doi.org/10.1146/annurev-ecolsys-110617-062614>

907 Schmidt, J. P., Hong, N., Dellinger, A., Beegle, D. B., & Lin, H. (2007). Hillslope Variability in  
908 Corn Response to Nitrogen Linked to In-Season Soil Moisture Redistribution. *Agronomy*  
909 *Journal*, 99(1), 229–237. <https://doi.org/10.2134/agronj2006.0187>

910 Seager, R., Lis, N., Feldman, J., Ting, M., Williams, A. P., Nakamura, J., et al. (2018). Whither  
911 the 100th Meridian? The Once and Future Physical and Human Geography of America’s  
912 Arid–Humid Divide. Part I: The Story So Far. *Earth Interactions*, 22(5), 1–22.  
913 <https://doi.org/10.1175/EI-D-17-0011.1>

914 Smith, F. W., Sampson, D. A., & Long, J. N. (1991). Comparison of Leaf Area Index Estimates  
915 from Tree Allometrics and Measured Light Interception. *Forest Science*, 37(6), 1682–  
916 1688. <https://doi.org/10.1093/forestscience/37.6.1682>

917 Soil Survey Staff. (2022). *Keys to Soil Taxonomy*, 13th ed. USDA-Natural Resources.

918 Tague, C. (2009). Modeling hydrologic controls on denitrification: sensitivity to parameter  
919 uncertainty and landscape representation. *Biogeochemistry*, 93(1/2,), 79–90.

920 Tague, C. L., & Band, L. E. (2004). RHESSys: Regional Hydro-Ecologic Simulation System—  
921 An Object-Oriented Approach to Spatially Distributed Modeling of Carbon, Water, and  
922 Nutrient Cycling. *Earth Interactions*, 8(19), 1–42. [https://doi.org/10.1175/1087-  
923 3562\(2004\)8<1:RRHSSO>2.0.CO;2](https://doi.org/10.1175/1087-3562(2004)8<1:RRHSSO>2.0.CO;2)

924 Vargas, R., Sonnentag, O., Abramowitz, G., Carrara, A., Chen, J. M., Ciais, P., et al. (2013).  
925 Drought Influences the Accuracy of Simulated Ecosystem Fluxes: A Model-Data Meta-  
926 analysis for Mediterranean Oak Woodlands. *Ecosystems*, 16(5), 749–764.  
927 <https://doi.org/10.1007/s10021-013-9648-1>

928 Walter, M. T., Walter, M. F., Brooks, E. S., Steenhuis, T. S., Boll, J., & Weiler, K. (2000).  
929 Hydrologically sensitive areas: Variable source area hydrology implications for water  
930 quality risk assessment. *Journal of Soil and Water Conservation*, 55(3), 277–284.

931 White, M. A., Thornton, P. E., Running, S. W., & Nemani, R. R. (2000). Parameterization and  
932 Sensitivity Analysis of the BIOME–BGC Terrestrial Ecosystem Model: Net Primary  
933 Production Controls. *Earth Interactions*, 4(3), 1–85. [https://doi.org/10.1175/1087-  
934 3562\(2000\)004<0003:PASAOT>2.0.CO;2](https://doi.org/10.1175/1087-3562(2000)004<0003:PASAOT>2.0.CO;2)

935 Wohlgemuth, P. (2006). *Hillslope erosion and small watershed sediment yield following a  
936 wildfire on the San Dimas Experimental Forest, southern California*. Reno, Nevada.:  
937 Proceedings of the 8th Federal Interagency Sedimentation Conference. Retrieved from  
938 [https://www.semanticscholar.org/paper/HILLSLOPE-EROSION-AND-SMALL-  
939 WATERSHED-SEDIMENT-A-ON-  
940 Wohlgemuth/e666a9991c2c1813f3e63289a20636d4028fb7ec](https://www.semanticscholar.org/paper/HILLSLOPE-EROSION-AND-SMALL-WATERSHED-SEDIMENT-A-ON-Wohlgemuth/e666a9991c2c1813f3e63289a20636d4028fb7ec)

941 Wood, E. F., Lettenmaier, D. P., & Zartarian, V. G. (1992). A land-surface hydrology  
942 parameterization with subgrid variability for general circulation models. *Journal of  
943 Geophysical Research: Atmospheres*, 97(D3), 2717–2728.  
944 <https://doi.org/10.1029/91JD01786>

945 Wood, E. F., Roundy, J. K., Troy, T. J., van Beek, L. P. H., Bierkens, M. F. P., Blyth, E., et al.  
946 (2011). Hyperresolution global land surface modeling: Meeting a grand challenge for  
947 monitoring Earth’s terrestrial water. *Water Resources Research*, 47(5).  
948 <https://doi.org/10.1029/2010WR010090>

949 Zarnetske, J. P., Haggerty, R., Wondzell, S. M., & Baker, M. A. (2011). Dynamics of nitrate  
950 production and removal as a function of residence time in the hyporheic zone. *Journal of*  
951 *Geophysical Research: Biogeosciences*, 116(G1). <https://doi.org/10.1029/2010JG001356>

952 Zhang, J., Cai, Z., & Müller, C. (2018). Terrestrial N cycling associated with climate and plant-  
953 specific N preferences: a review. *European Journal of Soil Science*, 69(3), 488–501.  
954 <https://doi.org/10.1111/ejss.12533>

955 Zhu, Q., Schmidt, J. P., & Bryant, R. B. (2012). Hot moments and hot spots of nutrient losses  
956 from a mixed land use watershed. *Journal of Hydrology*, 414–415, 393–404.  
957 <https://doi.org/10.1016/j.jhydrol.2011.11.011>

958 Zhu, Q., Schmidt, J. P., & Bryant, R. B. (2015). Maize (*Zea mays* L.) yield response to nitrogen  
959 as influenced by spatio-temporal variations of soil–water–topography dynamics. *Soil and*  
960 *Tillage Research*, 146, 174–183. <https://doi.org/10.1016/j.still.2014.10.006>

961 Zhu, Q., Castellano, M. J., & Yang, G. (2018). Coupling soil water processes and the nitrogen  
962 cycle across spatial scales: Potentials, bottlenecks and solutions. *Earth-Science Reviews*,  
963 187, 248–258. <https://doi.org/10.1016/j.earscirev.2018.10.005>

964

965



*[Water Resources Research]*

Supporting Information for

**Simulating the role of biogeochemical hotspots in driving nitrogen export from drylands watersheds**

<sup>1</sup>Jianning Ren, <sup>1</sup>Erin J. Hanan, <sup>2</sup>Aral Greene, <sup>3</sup>Christina Tague, <sup>4</sup>Alexander H. Krichels,  
<sup>1</sup>William D. Burke, <sup>5</sup>Joshua P. Schimel, <sup>2</sup>Peter M. Homyak

<sup>1</sup>Department of Natural Resources and Environmental Science, University of Nevada, Reno, 89501, Reno, USA

<sup>2</sup>Department of Environmental Sciences, University of California, Riverside, 92521, Riverside, USA

<sup>3</sup>Bren School of Environmental Science & Management, University of California, Santa Barbara, 93106, Santa Barbara, USA

<sup>4</sup>USDA Forest Service Rocky Mountain Research Station, 87102, Albuquerque, USA

<sup>5</sup>Department of Ecology, Evolution and Marine Biology, University of California, Santa Barbara, 93106, Santa Barbara, USA

**Contents of this file**

Figures S1

**Introduction**

Figures S1 are supplementary figures to support results of vegetation initialization.

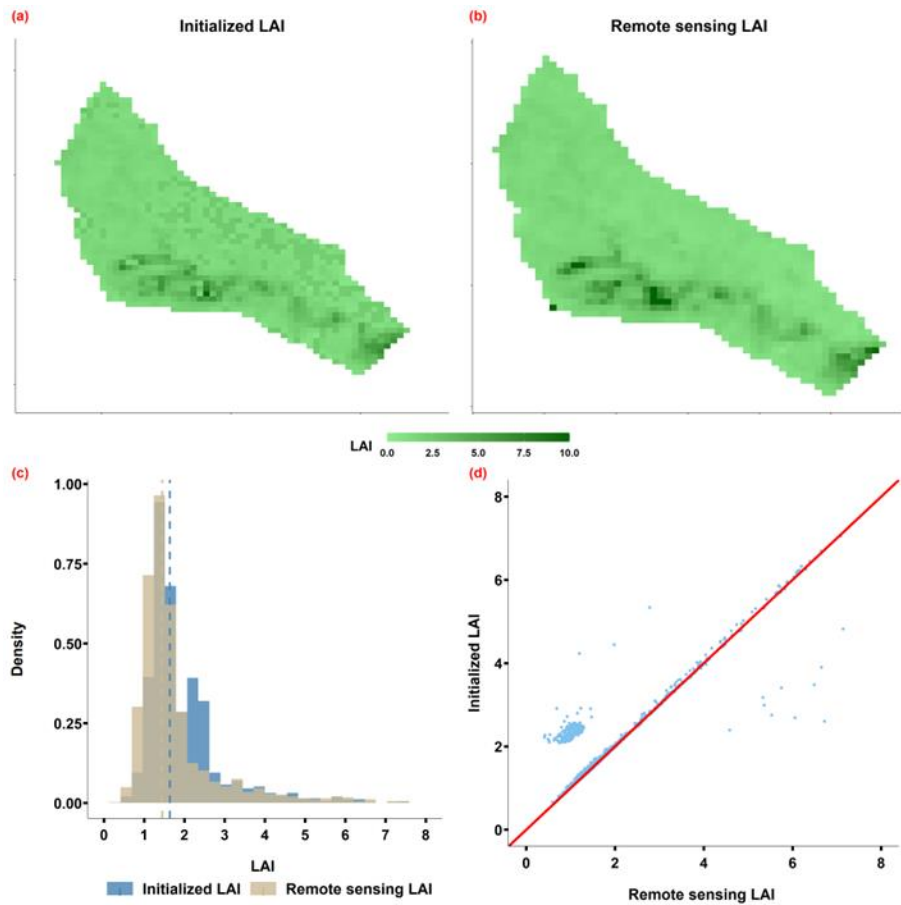


Figure S1. Vegetation initialization results for Bell 4: (a) initialized LAI from RHESSys, (b) target LAI calculated from a NAIP image from April 26, 2010, (c) comparison of density distributions between target and simulated LAIs; the dashed line is the mean of the two LAI distributions, and (d) scatter plot showing target LAI vs. initialized LAI for each patch.